Real-time monitoring of DNA hybridization and replication using optical and acoustic biosensors

Dissertation zur Erlangung des Grades

„Doktor der Naturwissenschaften“

am Fachbereich
Chemie und Pharmazie der
Johannes Gutenberg-Universität Mainz

vorgelegt von
Gudrun Stengel
aus Hanau

Januar 2004

Dekan:

1. Berichterstatter:
2. Berichterstatter:

Die vorliegende Arbeit wurde im Zeitraum zwischen März 2001 bis Januar 2004 am Max-Planck-Institut für Polymerforschung, Mainz angefertigt. Tag der mündlichen Prüfung: 17.02.2004

Contents

Abbreviations

ρ	density
η	shear viscosity
μ	shear modulus
2D	two-dimensional
bp	base pairs
c	concentration
cps	counts per second
Cy5	cyanine dye
D	dissipation factor
d	thickness
DNA	deoxyribonucleic acid
dATP	deoxyadenosine triphosphate
dCTP	deoxycytidine triphosphate
dGTP	deoxyguanosine triphosphate
dTTP	deoxythymine triphosphate
dNTP	deoxyribonucleoside triphosphate
ds	double-stranded
E	electric field
f	frequency
G	complex shear modulus
H	magnetic field
HEPES	n-[2-Hydroxyethyl]piperazine-n‘-[2-ethanesulforic acid]
I	intensity
k	wave vector
KF	Klenow fragment
LCR	ligase chain reaction
m	mass
n	refractive index, overtone number
nt	nucleotides
P	primer or probe
PBS	phosphate buffered saline
PCR	polymerase chain reaction
PMT	photomultiplier tube
QCM-D	quartz crystal microbalance with dissipation monitoring
RCA	rolling cycle amplification
SAM	self-assembled monolayer
SDA	strand displacement amplification
SNP	single nucleotide polymorphism
SP	surface plasmon
SPFS	surface plasmon fluorescence spectroscopy
SPR	surface plasmon resonance
ss	single-stranded
T	target or template
TIR	total internal reflection
TSM	transversal shear mode
x_{Label}	mole fraction of Cy5-labeled dCTP

1 Introduction

1.1 Biosensors

Nanotechnology involves the creation and utilization of materials and devices on the nanometer scale. In our days, biosensors are among the most promising nanotechnological achievements [Sahoo, 2003]. They have emerged to a well-known analytical technique in bio-medicine, biology and environmental control. Biosensors serve the sensitive and fast detection of biological compounds like DNA, antibodies or ligands of receptors by direct coupling of signal transduction to a molecular recognition event. The main reason for the popularity of biosensors is that they combine the excellent specificity of biomolecular recognition systems with the advantages of instrumental analysis.

A conventional biosensor consists of a solid surface functionalized with a biological recognition element, a liquid handling system and a physical transducer element [Lowe, 1985]. The latter creates a measurable signal as soon as an appropriate analyte is exposed to the surface and binds there. Typical binding partners are antibodies/antigenes, complementary DNA, enzymes/substrates or receptors/ligands. In the ideal case, the analyte detection is surface-sensitive, which means that the created signal is not influenced by the presence of analyte molecules in the bulk solution. The most common transducer elements make use of electrochemical [Bakker, 2002, Willner, 2002], piezoelectric [Marx, 2003, Janshoff, 2000] or optical principles [Brecht, 1997, Homola, 2003]. Electrochemical biosensors respond to changes in ionic concentration, redox potential, electron transfer rate or electron density; piezoelectric sensors monitor changes in the mass-load of the surface and optical sensors are either sensitive to changes of the interfacial refractive index or they utilize fluorescence mechanisms or a combination of both. In general, one distinguishes between label-free methods [Cooper, 2003] and those which require labeling of the biological units. On the one hand, labeling rises the costs of a method and limits its applicability, on the other hand it is a simple means to enhance the detection limit. Especially for optical methods, attachment of fluorescent-tags or the use of a second signal amplification mechanism like secondary antibodies or enzyme-catalyzed color reactions are wide-spread [Epstein, 2002, Yu, 2003, Liebermann, 2000]. The analyte solution can be either exposed under static conditions or using a constant flow rate. A circulation system significantly shortens the reaction times and enhances the detection limits since it facilitates the transport of the analyte molecules to the surface.

There are several advantages that make biosensors superior to conventional analytical methods: outstanding sensitivity and specificity, good reproducibility, rapid

response and the option for real-time monitoring, reusability of the device, ease of fabrication and application, possibility of miniaturization and low cost fabrication. Some of the advantages are direct consequences of the immobilization of the biological recognition unit; this way, the separation between bound and unbound species is possible by simple washing steps and the exchange of reaction compounds is facilitated. Thus, the immobilization process is central to biosensor fabrication. The difficulties are to exclude impairment of the functional units of biomolecules and to ensure stability and control of the surface coverage [Kasemo, 2001]. Common methods for surface immobilization utilize the covalent attachment or affinity binding, physisorption or electrostatic interactions in order to create highly ordered supramolecular architectures [Whitesides, 2003]. Surface-attachment of biomolecules also offers the basis for structuring surfaces such that a parallel read out of several probes is possible. Therefore biosensors often act as template for the development of microscopical methods allowing for high-throughput screening.

Due to the diversity of biological systems, there is no detection concept that is generally favorable. Rather, each system has its own requirements and possibilities one can take advantage of and needs to be investigated thoroughly in order to develop an optimized detection scheme.

1.2 Aim of the study

The accurate replication of genetic information is an indispensable process for every living organism. In cells, DNA polymerases are the enzymes in charge of template-directed DNA synthesis [Kornberg, 1992]. Thereby, the extension of primer DNA is achieved by the stepwise addition of the appropriate deoxynucleoside triphosphates (dNTPs) to its 3'-terminus. As a result, the DNA chain grows in 5' to 3'-direction. Goal of the present work was to reproduce this process in a biosensor format using the Klenow fragment (KF) of *E. coli* DNA polymerase I. The biosensor formats used in this study were Surface Plasmon Fluorescence Spectroscopy (SPFS) and the Quartz Crystal Microbalance with Dissipation monitoring (QCM-D). Special emphasis was placed on the ability of these techniques to follow the catalytic reaction in real-time.

To date, only a few studies are available, in which mass-sensitive surface analytical methods were utilized to investigate DNA-processing enzyme. Most of them aimed at the affinity of DNA/ RNA polymerases for different types of oligonucleotides. For instance, SPR was applied to examine the affinity of human DNA polymerase β for single-stranded, blunt-end, gapped, mismatched or double-stranded oligonucleotides [Tsoi, 2002]. In analogue, the interaction of HIV-I reverse transcriptase with recessed and blunt-ended DNA-RNA duplexes was compared [Gorshkova, 2001]. However, the

catalytic activity of the enzymes was only rarely addressed. SPR measurements were done on the cleavage of RNA substrates by a Ca^{2+}-dependent deoxyribozyme [Okumoto, 2003], for the in-vitro analysis of DNA transcription [Pemberton, 1999] and the elongation of DNA by a reverse transcriptase [Buckle, 1996]. Of special interest with regard to this thesis are two articles that describe DNA strand synthesis catalyzed by the Klenow fragment measured by QCM [Matsuno, 2001] and super critical angle fluorescence (SAF) detection [Krieg, 2003].

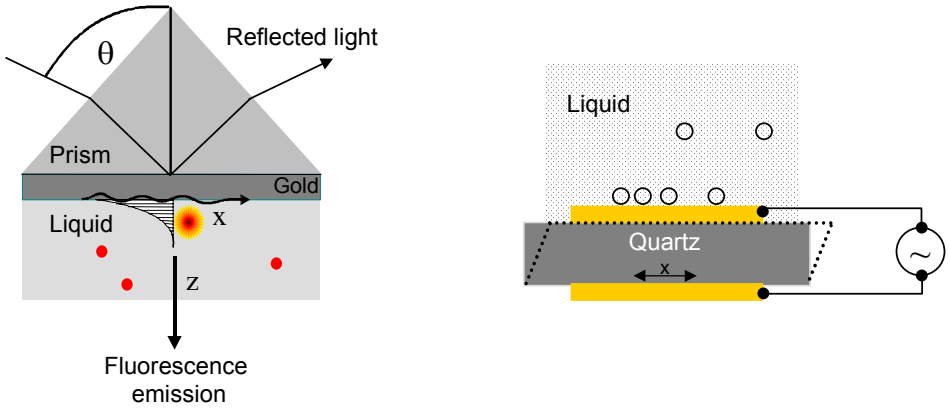

Figure 1.1: Schematic representation of the biosensor formats used for SPFS (left) and QCM-D (right) experiments.

For many catalytic reactions, the mass of the reaction product differs only insignificantly from that of the educt, making the use of mass-sensitive methods like SPR difficult. Aiming at the activity of enzymes, additional complications arise from the artificial environment a surface provides to an enzyme. Steric hindrance might impair enzyme activity. In this context, Thompson and coworkers studied even systematically the denaturation process of Chymotrypsinogen A close to a gold surface applying QCM [Yang, 1993]. Particularly, metal surfaces may influence surface charge and hydration state of an enzyme due to the existence of electric double layers in proximity to the surface [Vainrub, 2000]. Consequently, the requirements of a surface reaction may significantly differ from that being appropriate for the respective reaction in solution. Accordingly, major objective in the design of biosensors is to reveal surface-induced effects and to minimize them by creating well-suited surface architectures.

Both of the methods used in the present work are mass-sensitive, but they rely on different physical principles, which makes a comparison interesting. While SPFS is an optical, QCM is an acoustic method. In SPFS, the evanescent field of an electromagnetic surface wave propagating along a metal/liquid interface is used to excite chromophors in a surface-sensitive way [Liebermann, 2000]. The experimental design of the sensor is depicted in fig. 1.1. The surface wave (or surface plasmon) is

excited by resonant coupling of the collective oscillation of the metal electrons with incoming light whose momentum is accelerated by use of a high-refractive index prism. The experimentally observed parameter is the angle of incidence upon which resonance occurs. Since this angle depends strongly on the refractive index at the interface (which is proportional to the film mass), it is possible to follow adsorption and desorption processes. In QCM experiments, a piezoelectric quartz crystal is excited to perform shear oscillations by applying an alternating electric field across two gold electrodes (fig. 1.1) [see for a recent review Marx, 2003]. Here, frequency and damping of the shear oscillation depend on the mass and viscoelastic properties of the adsorbed film, which are measured experimentally.

The mass increase caused by the incorporation of a single nucleotide during DNA synthesis is quite small being only ~300 g/mol. Both techniques used here, provide mechanisms to enhance the signal caused by nucleotide addition: In SPFS, the incorporation of dye-labeled nucleotides was used to visualize the replication process; in parallel, changes in the surface coverage with enzyme could be monitored by means of the reflectivity signal making SPFS superior to conventional SPR or SAF, where either enzyme binding or nucleotide incorporation were observed. In QCM-D measurements, the mass signal is enhanced by water that is hydrodynamically trapped in DNA films and therefore couples to the shear motion of the quartz. Compared to QCM instruments not being designed for measuring the damping of the quartz, the QCM-D techniques adds valuable information by recording the dissipation factor. Measuring dissipation factor and frequency shift simultaneously allows for data analysis using viscoelastic models, which gives insights into material properties of thin films [Johannsmann, 1999, Höök, 2001].

The attractiveness of biosensors in studies of enzyme activity is based on the completeness of the picture that arises from those measurements compared to conventional solution methods. While solution methods provide only snapshots of one of the reaction steps or reaction intermediates involved in a complex reaction cycle, biosensors allow for time-resolved monitoring of a sequence of reaction steps. In the particular case of DNA replication, in principle all reaction steps being attributed to mass changes can be addressed by utilizing biosensors: DNA hybridization, polymerase binding, DNA elongation and enzyme release. Monitoring the binding of DNA polymerase molecules to surface-tethered DNA and DNA synthesis in real-time, gives access to affinity and kinetic constants and is anticipated to elucidate mechanistic details that remain hidden otherwise using solution techniques.

The present study had the following aims:

- Fabrication of a supramolecular surface architecture that is compatible with polymerase reactions.
- Real-time monitoring and identification of the reaction steps involved in DNA replication. Validation and comparison of affinity and catalytic constants derived by using SPFS and QCM-D.
- Characterization of the viscoelastic properties of different oligonucleotides and the active or inactive polymerase/DNA complex using QCM-D.
- Comparison of the benefits and shortcomings of the two techniques and extraction of information only accessible using both techniques in combination.

2 Theory

2.1 Surface plasmons

The phenomenon of surface plasmon resonance (SPR) was discovered in the 1960; it relies on the excitation of surface-charge oscillations at the interface between an absorbing and a non-absorbing dielectric like a metal/water interface [Burstein, 1974]. Surface plasmons (SPs) are bound non-radiative electromagnetic waves propagating along the interface being damped in the direction of propagation and along the surface normal. The conditions for the resonant excitation of SPs strongly depend on the refractive indices of the chemical environment at the interface, which is why SPR is ideally suited for monitoring surface reactions. The underlying principles are well understood and methods for the theoretical treatment of the system response have been established. For the interested reader, several excellent books describing surface plasmon theory [Agranovich, 1982, Raether, 1988, Yeh, 1988] and review articles are available [Knoll, 1997, Knoll, 1998].

In the following chapter, an introduction into optical reflection methods will be given. After explaining the general formalisms used to describe electromagnetic fields in dielectrics, the resonant excitation of surface plasmons will be discussed and the characteristics of SPR spectra outlined. In the end, SPFS, a combination of SPR and fluorescence spectroscopy, will be introduced.

2.1.1 Electromagnetic fields in matter

The fundamental description of electromagnetic waves propagating in an isotropic, homogenous medium is given by the well-known Maxwell's equations. The interested reader is referred to one of the standard textbooks dealing with electromagnetism [Karthe, 1991, Jackson, 1988]:

$$\nabla \times \mathbf{H} = \frac{4\pi}{c}\mathbf{J} + \frac{1}{c}\frac{\partial \mathbf{D}}{\partial t} \qquad \nabla \times \mathbf{B} = 0$$

$$\nabla \times \mathbf{E} = -\frac{1}{c}\frac{\partial \mathbf{B}}{\partial t} \qquad \nabla \times \mathbf{E} = 0$$

Eq. 2.1

where **D** is the effective electric field inside the dielectric, ρ is the (free) charge density, **E** is the imposed electric field, **B** is the magnetic induction, **H** is the effective magnetic field inside the dielectric, c is the speed of light, and **J** is the charge density.

$\nabla \times$ denotes the curl of a vector field. Solving the Maxwell's equations for certain boundary conditions leads to the material equations, which connect the four field quantities **E**, **B**, **H** and **D**. The connection between **D** and **E** is given by the wavelength-dependent dielectric function $\varepsilon(\omega) = \varepsilon' + i\varepsilon''$ of the material:

$$\mathbf{D} = \varepsilon(\omega) \cdot \varepsilon_0 \cdot \mathbf{E}$$

Eq. 2.2

where ε_0 is the permittivity in vacuum and ω the angular frequency. Analogously, **B** and **H** are connected by the magnetic permeability μ and the permeability of free space μ_0:

$$\mathbf{B} = \mu(\omega) \cdot \mu_0 \cdot \mathbf{H}$$

Eq. 2.3

The general wave equation describing the electric field of a planar wave as a function of time at a point x in an isotropic homogenous medium is given by:

$$\mathbf{E}(\mathbf{x}, t) = \mathbf{E}_0 \cdot \exp(i(\mathbf{k} \cdot \mathbf{x} - \omega \cdot t))$$

Eq. 2.4

where $\mathbf{E}_0$ is the electric field amplitude perpendicular to the wave vector **k** that points into the direction of propagation. Alternatively, the magnetic field **H** may be used to describe the planar wave:

$$\mathbf{H}(\mathbf{x}, t) = \mathbf{H}_0 \cdot \exp(i(\mathbf{k} \cdot \mathbf{x} - \omega \cdot t))$$

Eq. 2.5

It is obvious from the Maxwell's equations that both approaches are equivalent and knowing **H** or **E** is sufficient to calculate **E** or **H** using:

$$\mathbf{H}_0 = \frac{1}{\mu \mu_0 \omega} \cdot \mathbf{k} \times \mathbf{E}_0$$

$$\mathbf{E}_0 = \frac{1}{\varepsilon \varepsilon_0 \omega} \cdot \mathbf{k} \times \mathbf{H}_0$$

Eq. 2.6

Since momentum matching between the wave vectors of free photons and bound planar waves propagating along an interface is crucial for resonant SP excitation, we will focus on the wave vector at this point. Using the wave vector **k** instead of the wavelength λ allows for a precise description of planar waves in the three directions in space. The absolute value of **k** is connected with the wavelength as follows:

$$|\mathbf{k}| = \sqrt{k_x^2 + k_y^2 + k_z^2} = \frac{2\pi}{\lambda}$$

Eq. 2.7

with k_x, k_y, k_z being the wave vectors in x, y, z direction.

The dispersion relation for electromagnetic waves passing through a certain dielectric is given by:

$$\frac{\omega^2}{|\mathbf{k}|^2} = \frac{1}{\mu\mu_0\varepsilon\varepsilon_0} = \frac{c^2}{n^2}$$

Eq. 2.8

where c is the speed of light in vacuum, n the refractive index of a material. By assuming μ equals 1, the equation simplifies to an expression solely dependent on the dielectric constant:

$$|\mathbf{k}| = \omega \cdot \sqrt{\varepsilon\varepsilon_0\mu_0} = \mathbf{k}_0 \cdot \sqrt{\varepsilon} = \mathbf{k}_0 \cdot n$$

Eq. 2.9

where k_0 designates the wave vector of light in vacuum at the corresponding frequency.

2.1.2 Reflection and transmission of light

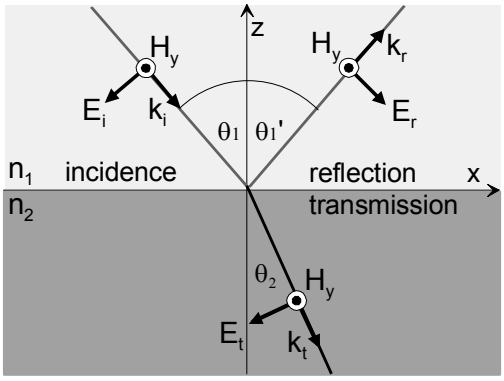

Figure 2.1: Reflection and transmission of p-polarized light at the interface between two different optical media.

Consider an interface in the xy-plane between two media with optical properties described by their refractive indices n_1 and n_2. Coming from layer 1, monochromatic polarized light passes through the media as depicted in fig. 2.1. Depending on the angle of incidence θ_1 and the optical constants of the materials, a certain fraction of the light will be reflected or transmitted into the adjacent optical medium. The sum of the energies of these two light waves equals to that of the original wave.

Since propagating light consists of a transverse electric and magnetic field, the magnetic, $H_{x,y,z}$, and electric field components, $E_{x,y,z}$, can have different orientations

parallel or perpendicular to the surface. Two modes of polarization can be distinguished for a wave propagating in the xy-plane:

Transversal magnetic polarization (TM or p-polarized light)
with

$$H_x = H_z = E_y = 0$$

and the non-vanishing components E_x, E_z and H_y. The electric field has a component E_z that oscillates in a plane perpendicular to the xy-plane.

Transversal electric polarization (TE or s-polarized light)
with

$$E_x = E_z = H_y = 0$$

and the non-vanishing components E_y, H_x, H_z. Here, the electric field only a field component that oscillates in parallel to the xy-plane.

Below the critical angle for total internal reflection, the reflection differs slightly for s- and p-polarized light. In the following considerations, we will focus on the TM mode since only this mode is able to induce a surface charge density along the z-direction, which is the pre-requisite for SP excitation. According to the reflection law, the angle of incidence θ_1 equals the angle upon which reflection occurs θ_1'. The transmitted ray is diffracted towards the surface normal according to Snell's law:

$$n_1 \cdot \sin\theta_1 = n_2 \cdot \sin\theta_1' \qquad \text{Eq. 2.10}$$

with $n_1 > n_2$. Monitoring the reflection R as a function of the angle of incidence yields the reflection spectrum (with $R=I_r/I_0$, where I_r is the intensity of the reflected and I_0 the intensity of the excitation light, respectively). Note that the intensity always corresponds to the square of the electric field, $|E|^2$. The spectrum can be theoretically predicted using a Transfer matrix algorithm [Raether, 1988].

Total internal reflection

Consider again fig. 2.1, where a ray of light travels through an optically dense medium (n_1) and approaches a medium with lower optical density (n_2). Depending on the angle of incidence, the ray is partly transmitted and partly reflected at the boundary of the two media. If one gradually increases the angle of incidence θ_1, it causes an increase of the transmission angle θ_2 until the maximum value of 90° is reached. At the

same time, the intensity of reflected light increases to the maximum, while the intensity of transmitted light is reduced until it vanishes at 90°. This particular angle of incidence is referred to as the critical angle. Upon further increase of θ_1, the reflection coefficient remains 1, indicating total internal reflection (TIR). The TIR regime is characterized by the existence of a plane wave travelling along the interface. This wave exhibits an electrical field component that decays exponentially in z-direction. The penetration depth, d, of the evanescent field is in the range of the wavelength λ that is used.

2.1.3 Dispersion relation of surface plasmons

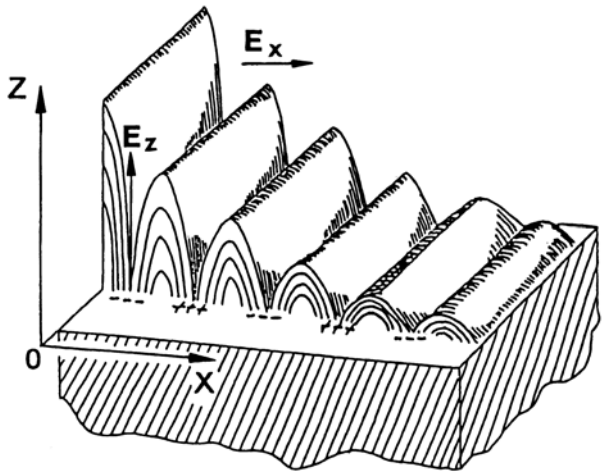

Figure 2.2: Schematic representation of a surface plasmon as surface-electromagnetic mode with field components E_x and E_z propagating along the x-direction coupled to a charge-density wave [Knoll, 1997].

Surface plasmons (SPs) are collective oscillations of the quasi-free electrons of a metal at the interface between a metal and a dielectric with the complex dielectric constants ε_1 and ε_2. The electromagnetic wave propagates along the interface, thereby exhibiting electric field components, which are damped in x- and z- direction (fig. 2.2).

In order to excite SPs at such an interface, the dielectric displacement $\mathbf{D}$ of the electromagnetic mode must have a component normal to the surface which induces a surface charge density σ:

$$(\mathbf{D_2} - \mathbf{D_1}) \cdot \mathbf{z} = 4\pi\sigma$$

Eq. 2.11

Only p-polarized light (see 2.1.2) exhibits an electric field component normal to the surface, E_z, by which a dielectric displacement in z-direction can be achieved. The corresponding electric and magnetic fields will have the following forms:

$$\mathbf{A}_1 = \mathbf{A}_{10} \exp i(k_{x1}\mathbf{x} + k_{z1}\mathbf{z} + \omega t) \qquad \text{in medium 1}$$
$$\mathbf{A}_2 = \mathbf{A}_{20} \exp i(k_{x2}\mathbf{x} + k_{z2}\mathbf{z} + \omega t) \qquad \text{in medium 2}$$

Eq. 2.12

where **A** stands for **E** and **H**, respectively**.** k_{x1} and k_{x2} are the wave vectors pointing into x-direction; k_{z1} and k_{z2} are the wave vectors in z-direction, perpendicular to the k_x vectors. ω is the angular frequency.

By applying the Maxwell's equation $\nabla \cdot \mathbf{E} = 0$ with $E_{x1} = E_{x2}$ and $H_{y1} = H_{y2}$ and $z = 0$ one will find a simple relationship between the dielectric constants and the normal components of the wave vectors

$$\frac{k_{z1}}{k_{z2}} = -\frac{\varepsilon_1}{\varepsilon_2}$$

Eq. 2.13

Eq. 2.13 indicates that SP excitation is only possible at interfaces between materials with dielectric constants of opposite signs. For an arbitrary material with $\varepsilon_d = \varepsilon'_d + i \cdot \varepsilon''_d$, one can distinguish two types:

1. isolating ($\varepsilon'_d > 1$), absorbing or non-absorbing ($\varepsilon''_d \geq 0$)
2. metallic ($\varepsilon'_d < 1$), absorbing ($\varepsilon''_d > 0$)

Thus, the interfaces between a metal and any non-conducting dielectric is well-suited for this purpose. Due to the chemical resistance in aqueous solution, gold is the metal of choice for most applications.

The dispersion relation (i.e. the energy-momentum relation) for SPs at a metal (ε_m)/ dielectric (ε_d) interface is given by:

$$k_x = k'_x + ik''_x = \frac{\omega}{c}\sqrt{\frac{\varepsilon_d \varepsilon_m}{\varepsilon_d + \varepsilon_m}}$$

Eq. 2.14

Eq. 2.14 has important consequences for the properties of SPs: Since ε_m is complex, the wave vector k_x has to be complex, too, where k''_x represents the damping part of the SP. Consequently, SPs exhibit a finite propagation length L, given by $L_x = 1/k''_x$. The propagation length limits the lateral resolution of SP-based microscopical methods. If gold/dielectric interfaces are used for sample preparation which are excited by light of 630 nm, the lateral resolution will be about 5 µm.

For the z-components of the surface plasmon mode holds:

$$k_{zd} = \sqrt{\varepsilon_d \left(\frac{\omega}{c}\right)^2 - k_x{}^2}$$

$$k_{zm} = \sqrt{\varepsilon_m \left(\frac{\omega}{c}\right)^2 - k_x{}^2}$$

Eq. 2.15

Thus, the wave vector k_z is purely imaginary corresponding to the existence of an evanescent field decaying exponentially along the surface normal. The penetration depth of the evanescent field is typically in the order of the wavelength of the light used for SP excitation. For the frequency range of interest always holds:

$$\sqrt{\varepsilon_d} < \sqrt{\frac{\varepsilon_m \varepsilon_d}{\varepsilon_m + \varepsilon_d}}$$

Eq. 2.16

As a consequence, the momentum of a free photon, $k_{ph} = \frac{\omega}{c}\sqrt{\varepsilon_d}$, propagating in a dielectric medium is always lower than the momentum of a SP propagating in the same medium. Therefore, special techniques are required for the resonant excitation of SP modes, which will be described in the following chapter.

2.1.4 Excitation of surface plasmons

The excitation of SPs is either possible by electrons or by photons. In this chapter only the use of photons for this purpose will be outlined. Pre-requisite for the resonant coupling of photons and SPs is that both electromagnetic waves are equal regarding their energy and momentum. The previously discussed dispersion relation (eq. 2.14) has shown that resonant excitation cannot be realized using free photons. The dispersion of free photons is described by the light line:

$$\omega = c_d \cdot k_{ph} \quad \text{with } c_d = \frac{c}{\sqrt{\varepsilon_d}}$$

Eq. 2.17

Relevant for the excitation of SPs is only the projection of the wave vector **k** in x-direction. For the simple reflection of a photon with the energy $\hbar\omega_L$ (fig. 2.4) the magnitude of the x-component, $k_{ph,x} = k_{ph}\sin\theta$, can be varied by changing the angle of

incidence, θ. $k_{ph,x}$ vanishes for perpendicular incidence of light, while it is maximized for large angles of incidence.

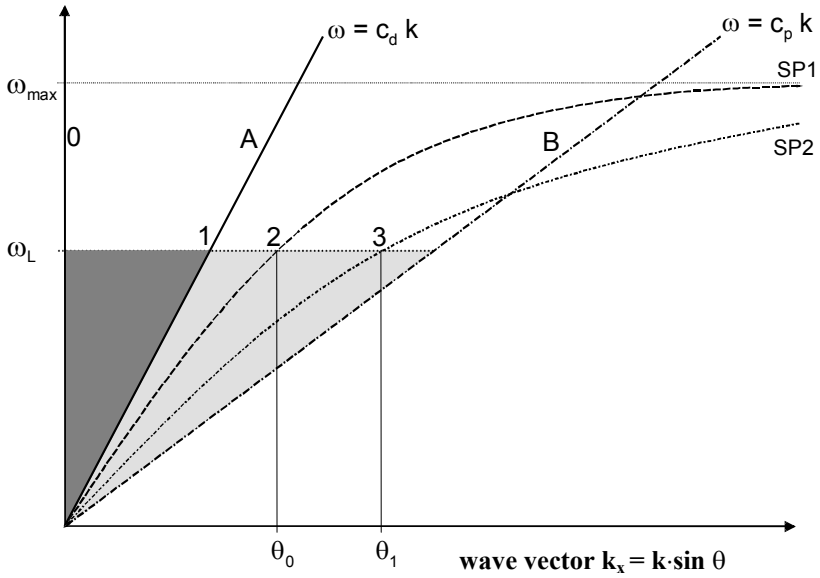

Figure 2.3: Dispersion relation for A) free photons in a dielectric, B) free photons propagating in a coupling prism, SP1) surface plasmons at a metal/dielectric interface and SP2) surface plasmons after adsorption of an additional dielectric layer [Liebermann, 1999].

A graphical representation of the dispersion of free photons and SP modes is given in fig. 2.3. The dispersion of photons in bulk is given as a straight line (A). The SP dispersion curve (SP1) approaches a maximum angular frequency that is attributed to the plasma frequency of the employed metal. Increasing the angle θ from 0° to the grazing angle, tilts curve a from point 0 to point 1 (dark gray area). Strikingly, there is no intersect between both lines, SP1 and A, which means that coupling of the modes is not possible by changing the angle of incidence alone. Therefore, a way must be found to increase the momentum of light.

Prism Coupling

A common way to accelerate the momentum of light are methods based on prism coupling. Using this method, the photons are not coupled directly to the metal/dielectric interface but via the evanescent tail of light upon total internal reflection at the base of a high refractive index prism ($\varepsilon_p > \varepsilon_d$). Line B in fig. 2.3 describes the increased momentum of photons travelling through a high index prism. Now, by choosing the appropriate angle of incidence (point 2), resonant coupling between the evanescent photons (B) and the surface plasmons (SP1) can be achieved. After adsorption of a dielectric film (SP2) the resonance occurs at an angle corresponding to point 3.

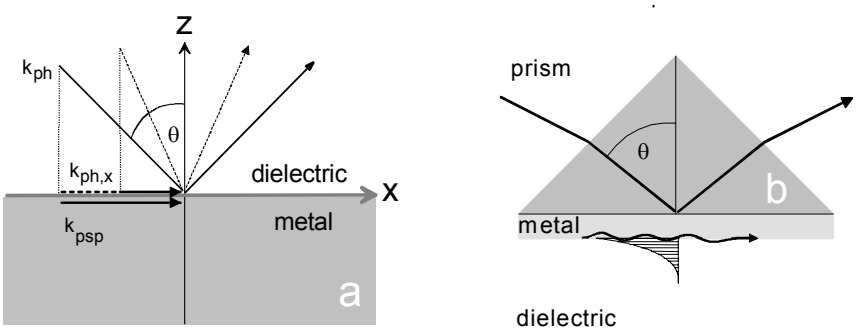

Figure 2.4: a) Reflection geometry for photons with a momentum k_{ph} at a metal/dielectric interface. The angle of incidence θ determines the absolute value of the momentum in z-direction, $k_{ph, x}$, that is relevant for surface plasmon excitation. b) Kretschmann configuration for momentum matching via prism coupling.

A detailed description of prism coupling can be found in [Knoll, 1998; Burstein, 1974; Raether, 1988]. The geometry experimentally used in the present work, is the Kretschmann configuration. As depicted in fig. 2.4 b, a high index prism is evaporated with a thin gold layer (~50 nm) adjacent to a lower index dielectric. Monochromatic p-polarized laser light is reflected at the base of the prism under an angle of incidence larger than the critical angle. The evanescent field resulting from total internal reflection overlaps with the surface plasmon mode and resonance is achieved by tuning the angle of incidence. If one monitors the intensity of reflected light while sweeping through a range of angles, plasmon resonance shows up as sharp dip in the reflectivity spectrum at the resonance angle.

SPR spectrum

Imagine a prism, the base being evaporated with a thin gold layer, which in turn is immersed in water. Monochromatic light is coupled to the oscillations of the quasi-free metal electrons via the prism resulting in SP excitation. The intensity of light reflected at the base of the prism is monitored as a function of the angle of incidence. As a results one obtains a typical SP scan spectrum as shown in fig. 2.5. If the geometry and the dielectric constants of the multiplayer system are known, the spectrum can be theoretically predicted using a transfer matrix algorithm [Karthe, 1991]. Employing this algorithm, the intensities of light being reflected and/or transmitted at each interface can be calculated. Below the critical angle for total internal reflection, a substantial amount of light is transmitted and therefore not detected in reflection geometry. Compared to the identical system lacking the gold layer, the intensities are higher below the critical angle because the metal layer acts as a mirror reducing transmission. The critical angle is determined by the dielectric constants of the prism and water only and hence, in practice allows for an angular calibration of the experimental set-up. Once the critical

angle is reached, the reflection remains constant until approaching the resonance angle that is significant for a particular system. SP excitation shows up in the reflectivity curve as a narrow dip with a minimum intensity that ideally reaches zero for full coupling efficiency. The dip exhibits a certain half width being attributed to the damping of the excited modes. The imaginary part of the complex dielectric constant accounts for dissipative losses typical of a metal. These losses also explain why the initial reflection coefficient of 1 is not reached again at angles exceeding the resonance angle. In the fictive case of a loss free metal the resonance dip should be infinitively sharp. Its finite width is reasoned by the resonance character of SP excitation. In reflection geometry one measures the coherent superposition of a partial wave directly reflected at the prism/metal interface with (a fraction of) the surface mode re-radiated via the prism. Destructive interference, quantitatively extinguishing the detected light, occurs only when the surface mode is phase shifted by 180° relative to the driving photon field. Accordingly, any damping (loss) in the system that broadens and smears the phase shift also broadens the plasmons curve.

2.1.5 Modification of the dispersion relation due to adsorption

Imagine a format in which SP excitation is realized using the Kretschmann configuration, the gold layer being adjacent to the bulk medium. Since the evanescent field of the SP mode is sensitive to its optical environment, any adsorption of material to the gold layer will change the resonance conditions. If the adlayer has a higher refractive index than the bulk medium, the mean refractive index sensed by the evanescent field is increased. As a result, the dispersion relation for SP is shifted towards larger wave vectors k_x, going from curve SP1 to SP2 in fig. 2.3. In order to account for this increase, resonance occurs at a higher angle of incidence. This corresponds to sweeping from point 2 to point 3 in fig. 2.3 (light gray area). Fig. 2.5 shows a typical SPR scan curve before and after adsorption of a thin film.
For non-absorbing layers, the shift in resonance angle is proportional to the product of the thickness gain, Δd, and change in refractive index, Δn:

$$\Delta\theta \propto \Delta n \cdot \Delta d$$

Eq. 2.18

For films thicker than ~200 nm one observes the excitation of waveguide modes in addition to SPs. The relation is also a good approximation for absorbing films if $d < 10$ nm.

From the thickness upon adsorption one can calculate the mass of the adsorbed film, Δm_{SPR}, as follows:

$$\Delta m_{SPR} = d \cdot \frac{n_{film} - n_{buffer}}{dn/dc}$$

Eq. 2.19

where dn/dc is the refractive index increment of a material given in ml/g.

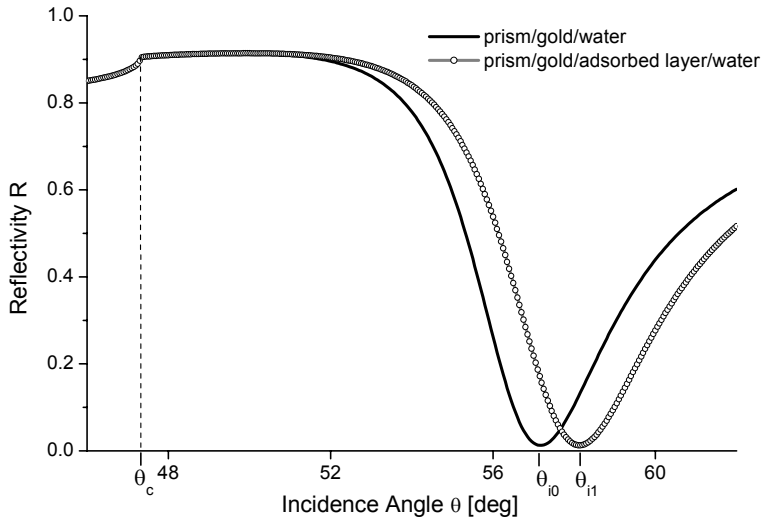

Figure 2.5: Resonance curve for a system consisting of a prism (ε'=3.4069), a gold layer (ε'= −12.1; ε''=1.3, d=50 nm) and water (ε'=1.778). Adsorption of a dielectric film (ε'=2.25; d=5 nm) shifts the resonance angle for surface plasmon excitation. θ_c denotes the critical angle for TIR, θ_{io} and θ_{i1} the resonance angle before and after adsorption of the dielectric layer.

2.2 Surface plasmon fluorescence spectroscopy

Due to its outstanding sensitivity, fluorescence spectroscopy is a powerful tool for the investigation and detection of biomolecules. Fluorescent probes offer a number of photophysical properties that can be exploited for the investigation of binding events. Ultrasensitive protein-DNA binding assays utilize fluorescence polarization [Bailey, 2001], fluorescence quenching [Dubertret, 2001], fluorescence enhancement [Faulds, 2004] and resonant energy transfer [Heyduk, 2002, Brown, 1997]. In the present work, the evanescent field of surface plasmons has been used to excite chromophors in a surface-sensitive way [Liebermann, 2000, Ruckstuhl, 2003]. The following chapters will explain the use of evanescent fields for fluorescence excitation, the basic principles of fluorescence and some issues relevant for the fluorescence emission near metallic surfaces.

2.2.1 Fluorescence mechanisms

Fluorescence is based on the absorption of photons, which causes the transition of a molecule from the ground to an electronically excited state. The absorption is maximal for a parallel orientation of the transition dipole moment relative to the electric field vector of the incoming light. For excited molecules, the emission of fluorescence light is only one possible decay mechanism. The Jablonsky energy diagram [Lakowicz, 1999, Noll, 1998] (fig. 2.6) summarizes alternative relaxation: The scheme shows different electronic states, the eletronic ground state designated as singlet (S_0) and the first existed singlet state, S_1. In each of these electronic states, the molecule can exist in a number of vibrational levels, which are populated according to the Boltzmann distribution law. The molecule exists in the lowest vibrational state of the electronic ground state prior to photon absorption. Upon photon absorption, the chromophor is excited to higher vibrational levels of S_1 or S_2, thereby obeying the Franck Condon principle. The transition occurs within 10^{-15} s. Than, the molecule relaxes to the vibrational ground state of the excited electronic state by collision with solvent molecules. This internal conversion (IC) happens within 10^{-2} s. From S_1 (v'=0), the molecule can relax to different vibrational states of S_0 upon emission of fluorescence light, which causes the fine structure of the emission spectrum. Fluorescence life times are typically in the order of 10^{-8} s. Since energy has been dissipated prior to fluorescence emission, the fluorescence light is red-shifted (Stokes-shifted) relative to the excitation light. In addition to fluorescence emission, three other radiation-less decay channels exist, which compete with the fluorescence process. Firstly, energy can be transferred to another molecule (quencher) that in turn emits the energy whether as

heat or as fluorescence light. The latter case is observable for chromophors forming a transiently stable complex (excimer complex) with a quencher that has different energy levels. The rate constant of this process is referred to as k_Q in the diagram. Alternatively, the molecule might be deactivated by singlet-singlet energy transfer (Förster transfer, k_{ET}). If the energy gap between the first excited triplet state T_1 (not shown here) and S_1 is small enough, the molecule might also switch between these states. This Inter System Crossing (ISC) is quantum mechanically not permitted; transition rates of $k_{ISC}=10^8\ s^{-1}$ have been measured for some systems, though. The slow ($k_P=10^{-2}$-$10^2\ s^{-1}$) transition from T_1 (v'0) to the singlet ground state S_0 is accompanied by the emission of phosphorescence light.

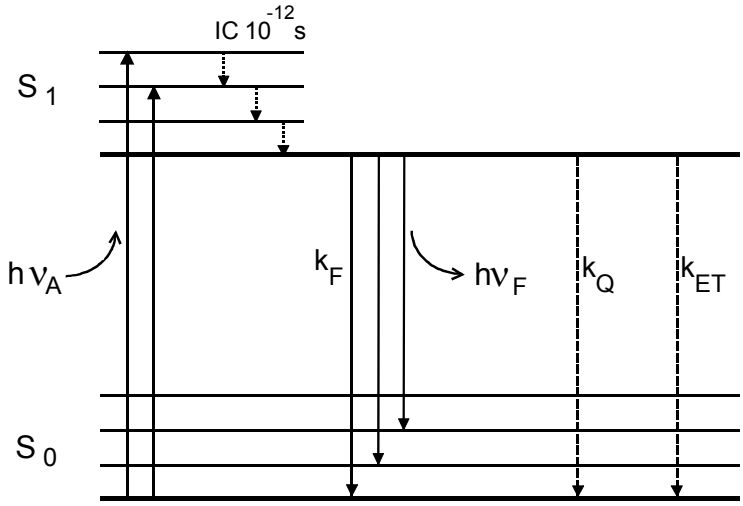

Figure 2.6: Jablonski energy diagram. The diagram illustrates the electronic and vibrational states of a molecule and gives an overview over possible decay mechanisms.

In a static fluorescence experiment, the number of molecules in the excited state remains constant because light absorption and relaxation of the excited state are in equilibrium. Relevant for the fluorescent yield observed in an experiment, is the quantum yield. The quantum yield Q is defined as the ratio of fluorescence intensity (I_F) and the number of absorbed photons per time unit (I_E):

$$Q = \frac{k_f}{k_f + k_o} = \frac{I_f}{I_a}$$

Eq. 2.20

where k_f is the rate constant for fluorescence emission and k_0 summarizes the rate constants for all existing radiation-less decay channels.

Fluorescence quenching

Fluorescence quenching designates all processes that decrease the fluorescence intensity of a fluorescent probe in an experiment. Hereby, the fluorescence lifetime is shortened by the presence of radiation-less decay channels for the excited state. Possible decay channels include excited state reactions, energy transfer, collision relaxation, and complex formation of the probe with other molecules. In the present work, the fluorescence yields are particularly influenced by the proximity of the fluorescent probe to the metal surface. In this geometry, energy can be transferred from the chromophor to the metal. Taking into account the nature of surface plasmons as periodic charge density fluctuations, the interaction originates from dipole-dipole interactions between the oscillating electrons and the chromophor. Due to the importance of the process, it will be discussed in detail in the next chapter.

2.2.2 Field distribution at a metal/dielectric interface

With respect to the combination of SPR and fluorescence spectroscopy, intensity and distribution of electromagnetic fields at a metal/dielectric interface are of particular relevance. While the penetration depth of the evanescent field determines the surface sensitivity of fluorescence excitation, the used metal is crucial for the enhancement of the electric field at the interface.

Since the electric field of p-polarized light consists of a x- and z-component, whereas the corresponding magnetic field exhibits only one component in y-direction, it is easier to present the magnetic instead of the electric field. Figure 2.7 shows the magnetic field intensity H_y calculated for the layer system: prism (ε=3.4069)/ gold (d=50 nm, ε= -12.1+ i·1.3)/adlayer (d=5 nm, ε=2.25)/water (ε=1.778) as function of the distance to the surface. The calculation is based on a transfer matrix algorithm. In fig. 2.7, three scenarios can be distinguished: The dotted curve at the bottom describes the field distribution obtained at the critical angle, the black line corresponds to the resonance angle and the dashed line results for an arbitrary angle below resonance (θ=50°). For angles exceeding the critical angle, the optical field exhibits a maximum intensity at the interface and decays exponentially to both sides, penetrating the metal and the water layer. Significantly, the field is enhanced by a factor of 16 relative to the TIR case and has a penetration depth of about 200 nm.

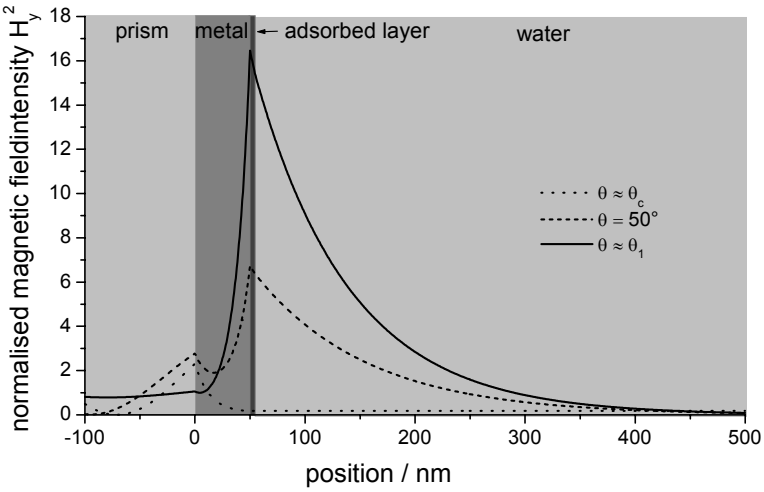

Figure 2.7: Normalized magnetic field intensity along a layer system prism/metal/adlayer/water. The field enhancement at the metal/dielectric interface at incidence angles close to the resonance angle is evident [Liebermann, 1999].

2.2.3 Fluorescence excitation by evanescent fields

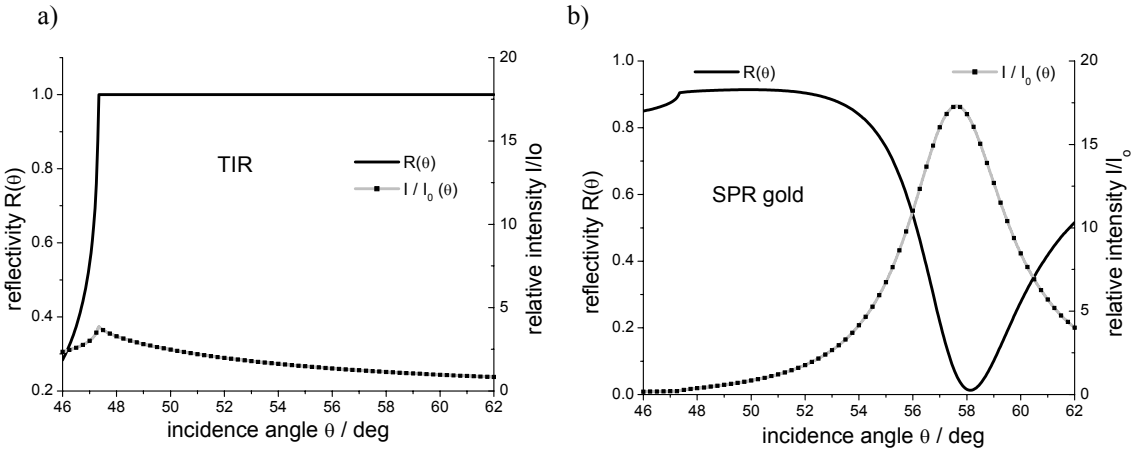

Figure 2.8: Field enhancement at interfaces. Theoretically predicted reflectivity and field intensity for a glass/water interface (a) and a glass/gold/water layer system (b).

The optical field schematically depicted in fig. 2.7 is an efficient means to excite chromophors coming close to the surface in the course of interfacial reactions. Surface Plasmon Fluorescence Spectroscopy (SPFS) makes use of this possibility. Here, the reflected light and fluorescence emission are recorded simultaneously by positioning a second detector at the backside of the prism (see fig. 1.1). The angle-dependence of the electric field has direct consequences for the SPFS spectra obtained this way. In fig. 2.8, theoretical calculations for the reflectivity and field intensity are plotted versus the

angle of incidence for two different systems: a) shows the field enhancement expected at a prism/water interface in TIR geometry, b) displays the field enhancement predicted for the excitation of surface plasmons in a system consisting of prism/gold/water.
For the pure dielectric case, a maximum field enhancement by a factor of 4 is observed at the critical angle. Here, the enhancement originates from the constructive interference of the incoming and reflected electromagnetic fields at the critical angle. The reflectivity remains constant above the critical angle as typical for the TIR geometry. In contrast, the maximum field enhancement for system b) is achieved at the resonance angle and amounts to a factor of 16 for gold. This is a logical consequence from the fact that a maximal amount of energy is transferred to the interface at resonance conditions. The enhancement factor as well as the half width of the fluorescence peak is determined by the absorption properties of the used metal. The stronger the absorption by the metal (indicated by large values of ε''), the smaller the field enhancement and the broader the fluorescence peak. For instance, a silver film, being less absorbing than gold, causes a field enhancement by a factor of 80, which is also attributed to a sharper fluorescence peak.

At a closer look, the maximum of the fluorescence peak is located at slightly lower incidence angles than the reflectivity minimum. This phenomenon is explained by the resonance character of surface plasmon excitation as described in the previous chapter. The angle designated by the fluorescence peak corresponds to the true resonance angle, whereas the minimum in reflectivity is observed at a position where destructive interference between the photons reflected at the prism/metal interface and the SP modes, out-coupled via the prism in the same direction, extinguishes the ray. Destructive interference occurs only if the surface mode is phase shifted by 180° relative to the driving photon field. Since any damping occurring in the system, broadens and smears the phase shift, light is extinguished at angles larger than the resonance angle.

2.2.4 Fluorescence emission near metallic interfaces

The vicinity of a chromophor to a metal surface offers additional loss channels, which do not play a role for experiments in solution [see review from Barnes, 1998]. Since the metal surface acts as a mirror, the emitter interferes with the reflected electromagnetic waves. If the reflected field is in phase with the emitter, the dipole will be driven harder, which enhances the emission. The opposite way, the emission will be reduced if the reflected wave is out of phase. Thus, the spontaneous emission rate is expected to oscillate with increasing distance, since the phase of the reflected field changes with distance. At the same time, the oscillation strength will decrease with

distance due to the emitters nature as point source. The radiation field of a dipole weakens with increasing distance and so does the field reflected at the metallic interface. Drexhage and coworkers measured the lifetime of Eu^{3+} ions in front of a silver mirror and confirmed this classical picture [Amos, 1997, Drexhage, 1974]. However, simple interference does not explain the strong quenching of fluorescence for small emitter-surface distances (< 40 nm). In this region the excited molecule may decay radiation-less via coupling to guided waves such as surface plasmons and/or lossy waves. Considering the geometry of the biosensor used in the present work, three main decay channels can be imagined:

a) Non radiative transition and exciton coupling

At dipole-metal distances smaller than 10 nm, fluorescence quenching originates from the transfer of energy from the excited dipole to the metal surface. If electron-hole pairs of the metal (excitons) act as energy acceptors, the transfer will be dipole-dipole in nature. The transferred energy is dissipated in the metal. The standard Förster model for energy transfer between two point dipoles shows a d^{-6} dependence of the transfer rate. This is because it depends on the near field of both, the donor and the acceptor, the strength of which falls with d^{-3}. For exciton excitation the acceptor is considered to be a planar array of dipoles rather than a point dipole. Integration over all possible transfer sites yields a d^{-4} dependence for the transfer rate. Fig. 2.9 illustrates the distance-dependence of the fluorescence intensity near a metallic surface, which is given by:

$$\frac{I_d}{I_\infty} = \left[1 + \left(\frac{d_0}{d}\right)^4\right]^{-1}$$

Eq. 2.21

where I_∞ denotes the fluorescence intensity at infinite separation distance in the absence of a metal surface, I_d is the observed fluorescence intensity at a distance d from the surface. d_0 is the so called Förster radius that corresponds to the distance at which the fluorescence is decreased to the 50 % level. This radius ranges typically between 5 and 10 nm for biological probes. In order to calculate a theoretical quenching profile for the present SPFS system, one has to consider the probability for fluorescence emission in a) all directions b) towards the photodiode on the backside of the prism and c) towards the gold surface, where coupling of the fluorescence light to surface plasmons is possible. The result is also shown in fig. 2.9 [Neumann, 2001].

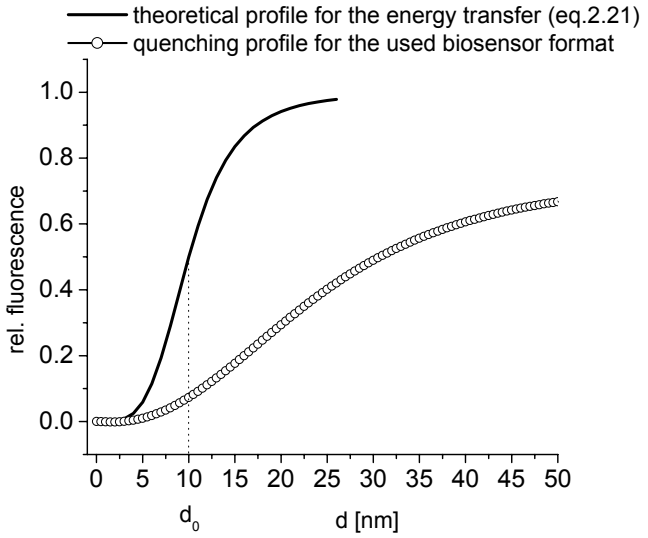

Figure 2.9: Transfer of energy according to eq. 2.21 (black line). The curve was calculated assuming a Förster radius of 10 nm. In addition, a theoretical quenching profile giving the fluorescence that can be detected in SPFS experiments.

b) Coupling between the emitter and surface plasmon modes

Excitation of surface plasmon modes at the wavelength of fluorescence emission dominates at distances around 20 nm. As a first approximation, the decay of energy from the excited dipole to a non-radiative surface plasmon mode cannot be observed. Momentum-matching techniques such as prism or grating coupling can be used to couple the surface plasmon modes to photons, thereby proofing their existence. The plasmon-coupled fluorescence emission exhibits a characteristic angular distribution and polarization which are determined by the emission spectrum of the fluorophor and the dispersion relation of the SPs.

c) Emission of photons

At metal-dipole distances larger than 20 nm, free emission of photons is the prevailing process. Since fluorescence is excited by the exponentially decaying evanescent tail of a SP mode in the present sensor format, no fluorescence is observed for distances exceeding the penetration depth of the SP mode. The penetration depth of a SP is in the range of 200 nm for an excitation wavelength of 630 nm. Using the classical picture of a dipole, it becomes possible to predict the emission rate. Doing so, the orientation of the dipole relative to the surface has to be taken into account because a reflecting surface produces an image dipole. For small separation distances, a dipole that is parallel to the surface tends to be cancelled out by its image. In contrast a dipole being perpendicular to the surface will be enhanced by its image dipole. Both effects are less pronounced with increasing separation distances.

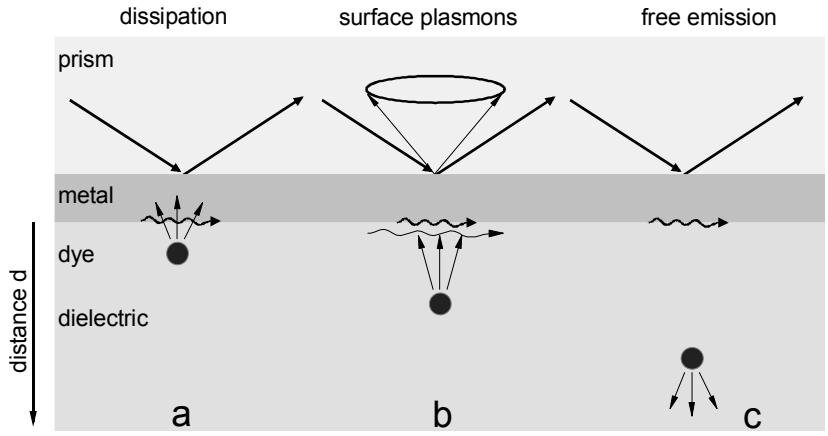

Figure 2.10: Decay channels for fluorescence emitted near a metallic surface. a) non-radiative energy transfer, b) coupling of irradiated fluorescence light to SP modes, c) free emission of fluorescence.

2.3 Quartz crystal microbalance with dissipation monitoring

The Quartz Crystal Microbalance (QCM) has been routinely used to measure the thickness of metal films obtained from thermal evaporation in vacuum for several decades [Warner, 1963]. The measuring principle is based on the shift of the resonance frequency of a quartz crystal excited to acoustic shear oscillations as a function of its mass load. According to the well-known Sauerbrey equation exists a linear relation between these quantities for films in gaseous environment [Sauerbrey, 1959]. The interpretation of QCM data obtained from measurements in liquid is largely complicated by a) water that couples to the shear motion of the quartz either by viscous drag or by entrapment and b) damping of the oscillation due to viscoelastic behavior of adsorbed films [Johannsmann, 1999, Höök, 2001]. Since the investigation of biomolecular recognition events requires to operate the QCM in liquid, advancements have been made to facilitate the data recording and analysis. Among these achievements is the new QCM-D instrument used in the present study [Rodahl, 1996]. Whereas most conventional QCM set-ups are designed to monitor the shift of the resonance frequency only, QCM-D measures the dissipation factor, ΔD, and frequency change, Δf, simultaneously at several harmonics with excellent time-resolution. The dissipation factor is a measure for the damping of the quartz and will be discussed later (see 2.3.3). Acquiring ΔD and Δf at several harmonics offers the possibility to analyze the raw data using a viscoelastic representation based on the Voigt model [Voinova, 1999]. So far, the method has been successfully applied in different fields such as adsorption of vesicles and proteins [Yang, 1993, Höök, 1998, Reimhult, 2002], DNA hybridization [Höök, 2001, Larsson, 2003] and cell adhesion [Andersson, 2003].

2.3.1 Excitation of acoustic shear waves

Commonly, QCMs consist of a thin quartz wafer sandwiched between two gold electrodes [Brise, 1997]. Quartz is the piezoelectric crystalline form of SiO_2. According to the indirect piezoelectric effect, applying an alternating electric field across the electrodes will induce a periodic deformation of the quartz plate. Since the deformation is attributed to periodic density fluctuations in the material, a standing acoustic wave is generated. Depending on the cut of the quartz crystal, different modes of oscillation can be excited. The quartz crystal commonly used for QCM application is cut at an angle of $\theta = 35°$ from the crystallographic zx-plane, which is referred to as AT-cut. AT-cut quartzes oscillate in the transversal shear mode (TSM); the shear motion originates from the coplanar displacement of the quartz relative to the surface. A beneficial feature of AT-cut quartzes is their excellent temperature stability (with temperature drifts of about 2 ppm/ °K). The thickness of the quartz plate d_q determines the fundamental frequency

f_0 of the shear motion by defining the wavelength of the fundamental oscillation. Thereby, the surface of the quartz crystal will be the anti-nodes of the oscillation of a standing wave within the quartz plate. For the resonance frequency holds:

$$f_n = n \cdot f_0 \quad \text{with} \quad f_0 = \frac{c_t}{\lambda} = \frac{c_t}{2d_q}$$

Eq. 2.22

where c_t is the transversal velocity of sound, d_q the thickness of the quartz plate, λ the wavelength and n is an odd integer (1, 3, 5, ...). Even overtones (harmonics) cannot be excited by electrical means because the integral polarization between the electrodes vanishes for symmetric strain patterns (c.f. fig. 2.11). If the thickness of the medium the acoustic wave propagates through is increased by adsorption of a film, the resonance frequency of the quartz crystal will decrease. Sauerbrey was the first one who derived an equation describing the frequency shift, Δf, caused by the deposition of a mass Δm_S on the electrodes of the quartz [Sauerbrey, 1959]:

$$\Delta m_S = -\frac{\rho_q d_q \Delta f}{n f_0} = -\frac{C \Delta f}{n} \Rightarrow C = \frac{\rho_q d_q}{f_0}$$

Eq. 2.23

with ρ_q being the specific density of the quartz crystal and n the overtone number. Using $\rho_q = 2648$ kg/m^3, $f_0 = 5$ MHz and $d_q = 0.33$ mm, C amounts to 17.7 ng/cm^2. Sauerbrey's assumption holds only true if the added mass is significantly smaller than the mass of the quartz crystal. Experimental data confirmed the Sauerbrey equation for mass loads up to 2 % (m_{film}/m_{quartz}). Furthermore, the film has to be homogenous and rigidly attached to the quartz surface so that no slip or inelastic deformation occurs during the oscillatory motion.

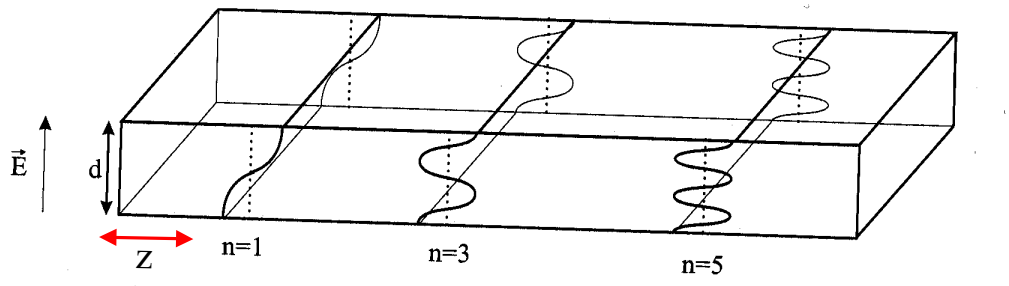

Figure 2.11: Transversal acoustic shear modes at n=1, 3 and 5. Only odd-numbered overtones are excitable. E denotes the electric field vector, z the lateral displacement of the quartz plate.

2.3.2 QCM operated in liquid environment

In liquids, the elasticity of an adsorbed film might change dramatically due to solvation and swelling effects. Especially for biological materials like proteins and DNA, the up-take of water is a pre-requisite for adopting their natural secondary structures resulting in lose and flexible surface architectures. Under these condition, deviations from the linear relation between Δm and Δf originate from the viscoelastic behavior of a material. The standing acoustic waves are not fully reflected anymore at the interface between film and bulk medium but propagate into the liquid. In this case, the effectively coupled mass depends on the damping of the oscillatory motion by the viscoelastic film and on the properties of the bulk liquid. In 1985, Kanazawa and Gordon published a theory on the behavior of QCM in liquid phase that described the oscillation frequency of the quartz in terms of the material properties of the quartz and the bulk liquid [Kanazawa, 1985]. The theory was based on a physical model, which coupled the shear wave in the quartz crystal to a damped shear wave in the liquid. The resulting shear wave decays into the liquid. The decay length δ is the distance after which the amplitude of the shear wave is reduced to a 1/e fraction and is given by:

$$\delta = \sqrt{\frac{4\pi\eta_l}{f_n\rho_l}}$$

Eq. 2.24

with η_l being the viscosity of the bulk liquid, ρ_l the liquid density and f_n the resonance frequency of the dry quartz. For a 5 MHz quartz oscillating in water the decay length calculates to 250 nm at 20°C. Not only the decay length of the shear wave is affected by the liquid environment but also its amplitude, i.e. the lateral displacement of the quartz. From the classical oscillator theory it is clear that the amplitude is a function of the driving voltage applied and the quality factor Q (the inverse of the dissipation factor D) of the system. Kanazawa derived following equation [Kanazawa, 1997]:

$$A_{av} = C_{av} \cdot Q \cdot V_d$$

Eq. 2.25

A_{av} is the average amplitude of vibration (the average corresponds to the half maximum), C_{av} an empirical constant, Q the quality factor and V_d the drive amplitude. Values for C_{av} published so far by different authors range from 0.7 to 3.1 pm/V. Summarizing different theoretical and experimental results, the amplitude of a 5 MHz quartz operated in air with a quality factor of 100.000 and a driving amplitude of 1 Volt is within a range of 40-200 nm. Since, the Q-factor for the same system in water decreases to 3000, the amplitude of vibration is diminished to 1-6 nm.

In chapter 2.3.5 a model will be introduced that allows for calculating the frequency shift and dissipation observed upon adsorption as a function of the viscoelastic properties of a film.

The interpretation of QCM data obtained from experiments in liquids is further complicated by water sensed as an additional mass [Larsson, 2003]. Responsible are factors that force the water to move synchronously with the surface of the quartz, for instance the entrapment of water in cavities of the film or viscous drag [Höök, 2001]. This means the layer is essentially sensed as a viscoelastic "hydrogel" composed of macromolecules and water. It is not possible to separate the mass contributed by the "dry" film and by water without applying other methods, which are solely sensitive to the mass of the macromolecules, e.g. SPR. Thus, the observed difference between the mass up-take measured by QCM, Δm_{QCM}, and the optical mass, Δm_{opt}, corresponds to the amount of water sensed by the QCM.

$$\rho_{effective} = \frac{\rho_{biomolecule} \cdot \Delta m_{opt}}{\Delta m_{QCM}} + \rho_{water}\left(1 - \frac{\Delta m_{opt}}{\Delta m_{QCM}}\right)$$

Eq. 2.26

Knowing the effective density gives access to the effective thickness simply by:

$$d_{effective} = \frac{\Delta m_{QCM}}{\rho_{effective}}$$

Eq. 2.27

ρ_{water} and $\rho_{biomolecule}$ are the densities of water (~1 g/cm^3) and biomolecules, being 1.1 g/cm^3 for lipids, 1.4 g/cm^3 for proteins and 1.7 g/cm^3 for oligonucleotides .

2.3.3 The dissipation factor

The dissipation factor, D, or the inverse of D, the quality factor Q [Smith, 1986] describes the energy loss of an oscillatory system during one period of oscillation. A general definition of the dissipation factor is given by:

$$D_{total} = \frac{E_{dissipated}}{2\pi E_{stored}}$$

Eq. 2.28

where $E_{dissipated}$ is the dissipated energy and E_{stored} is the energy stored in the oscillating system. Accordingly, D_{total} includes all channels for energy loss existing in a particular

system. Typical mechanisms causing energy dissipation in QCM measurements are a) viscous coupling of adsorbed moleculaes to the solvent b) internal friction in the quartz crystal c) losses due to crystal mounting d) oscillatory motions induced in the adlayer. Viscous coupling designates movement of the liquid non synchronously to the surface causing a progressive phase lag with increasing distance from the surface. Spencer and Smith [Spencer, 1966] found that the amplitude of a quartz crystal decays as an exponential sinusoidal described by the general form: $A(t) = A_0 \exp(-t/\tau) \cdot \sin(2\pi ft + \phi)$ with A being the amplitude, t the time, τ the decay time and f the frequency. The dissipation factor D is inversely proportional to the decay time τ of the sinusoidal:

$$D_{total} = \frac{1}{\pi f_0 \tau}$$

Eq. 2.29

Hence interrupting the driving electric field and measuring the decay time τ of the quartz crystal provides a method to determine the dissipation factor.

2.3.4 Viscoelastic film properties

For measurements in liquids, the QCM-D response is significantly influenced by the viscoelastic properties of the material adsorbed on top of the quartz crystal. When stress is applied to a viscoelastic material, it results in a combination of elastic deformation (reversible energy storage) and dissipation (irreversible energy loss). For a purely elastic deformation, the stress (T) is proportional to the strain (S). The strain is given by Hook's law: $T=\mu S$, in which μ is the stiffness of the material. In contrast, purely viscous dissipation, as present in a Newtonian fluid, depends on the strain rate: $T=\eta(dS/dt)$, where η is the viscosity, t the time and dS/dt the strain rate. Viscoelastic properties can be approximated by various combinations of springs and dashpots [Aklonis, 1983], representing the elastic and the inelastic part, respectively. In the present study, a viscoelastic representation based on the Voigt model has been used to simulate the QCM-D response. The Voigt model consists of a parallel combination of a spring and a dashpot. In a circuit like this, the strains across the elements are equal, while the stresses are additive giving rise to a constitutive relation:

$$G = \frac{T}{S} = \mu_f + i2\pi f\eta_f$$

Eq. 2.30

where η_f is the shear viscosity, μ_f the shear elastic modulus and f the frequency. G defines a new measure, which is the complex shear modulus. The subscipt "f" indicates

that shear viscosity and elastic modulus are properties of the adsorbed film. Eq. 2.30 can be also expressed in terms of the characteristic relaxation time, $\tau = \eta_f/\mu_f$, of a system:

$$G = \mu(1 + i2\pi f\tau)$$

Eq. 2.31

From this form it is obvious that the storage modulus is independent of the frequency, while the damping part of the complex shear modulus depends on it.

2.3.5 Modeling of the QCM-D response

This thesis is mainly concerned with monomolecular DNA films. As discussed in a recent publication [Larsson, 2003], the QCM-D response observed for DNA films is governed by changes in viscoelasticity. In this section, a description of the viscoelastic representation will be given that was used to analyze the QCM-D raw data presented in the result chapters. Limits set by the model and the fitting procedure will be addressed, providing the reader with an appropriate background on which basis to judge the conclusions drawn from the model.

Based on the mechanical Voigt model (c.f. 2.3.4), Voinova et al. [Voinova, 1999] solved the wave equation describing the shear oscillation of a quartz plate covered by a viscoelastic film that adjoins to a semi-infinite Newtonian liquid under "no-slip" conditions. The general solution of this wave equation is referred to as β-function. The shift in resonance frequency, Δf, and dissipation factor, ΔD, can be obtained from the imaginary and the real part of the β-function.

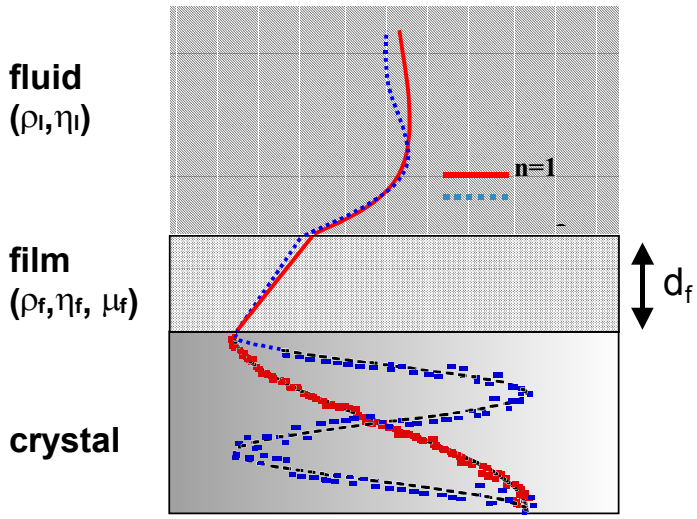

Figure 2.12: Schematic presentation of an acoustic wave propagting through a viscoelastic material. The geometry and parameters the Voigt model-based viscoelastic representation refers to is also illustrated. With permission of Q-Sense AB.

In this picture, the film is represented by a uniform thickness d_f, density ρ_f (whereby, $d_f \cdot \rho_f$ equals the coupled mass Δm_{QCM}) and the complex shear modulus G:

$$G = G' + iG'' = \mu_f + i2\pi f\eta_f \qquad \text{Eq. 2.32}$$

where μ_f is the elastic shear (storage) modulus and η_f the shear viscosity (loss modulus). Fig. 2.12 gives a schematic illustration of the geometry and the parameters used to simulate the response of a quartz crystal upon mass load in contact with bulk liquid. For a single layer, the changes in the resonant frequency Δf and the dissipation factor ΔD are:

$$\Delta f = \frac{\mathrm{Im}(\beta)}{2\pi d_q \rho_q} \qquad \text{Eq. 2.33}$$

$$\Delta D = -\frac{\mathrm{Re}(\beta)}{\pi f d_q \rho_q} \qquad \text{Eq. 2.34}$$

with

$$\beta = \xi_l \frac{2\pi f\eta_f - i\mu_f}{2\pi f} \frac{1-\alpha\exp(2\xi_l d_f)}{1+\alpha\exp(2\xi_l d_f)}$$

$$\alpha = \frac{\frac{\xi_l}{\xi_2}\frac{2\pi f\eta_f - i\mu_f}{2\pi f\eta_l} + 1}{\frac{\xi_l}{\xi_2}\frac{2\pi f\eta_f - i\mu_f}{2\pi f\eta_l} - 1}$$

$$\xi_l = \sqrt{-\frac{(2\pi f)^2 \rho_f}{\mu_f + i2\pi\eta_f}}$$

$$\xi_2 = \sqrt{i\frac{2\pi f\rho_l}{\eta_l}}$$

where d_q and ρ_q are the quartz thickness and density, respectively, and $f=n\cdot f_0$ with n (=1, 3, 5...) being the overtone number and f_0 the fundamental resonance frequency. ρ_l and η_l are the bulk liquid density and viscosity; note that the model also accounts for the bulk-liquid contributions to Δf and ΔD by subtracting them from the changes in f and D induced upon e. g. adsorption of a viscoelastic film.

Since the present system, consisting of a DNA film on top of a surface-tethered 2D arrangement of streptavidin, can hardly be considered homogenous, a two- or even three-layer model seems to be more appropriate to represent the true situation. However, since the thiol and streptavidin layer have negligible contributions to the dissipation factor, they can be considered perfectly elastic and excluded from the modeling. Indeed, the results obtained from a single-layer model were in excellent agreement with results produced applying a multi-layer model. However, treating the DNA films, prior and after template hybridization and replication, as a single layer does not allow to account for density fluctuation during the reactions. Since d_f ($=\Delta m_{QCM}/\rho_f$),

assuming a fixed density might cause errors in the determination of the thickness, if the density variations are large.

The Voigt-based viscoelastic model contains four unknown parameters. But combined frequency and energy dissipation monitoring yield only two experimental observables, which leads to a non-unique system. The approach chosen in the present work to circumvent this limitation is to switch extremely fast between different excitation frequencies during a measurement, which enables simultaneous data acquisition at higher harmonics (n=1, 5, 7…). Since the availability of SPR data for the present system allowed us to estimate precisely the density of the DNA films and therefore to keep this value fixed during the fitting, the responses from two harmonics are sufficient to create an over-determined system. Using this approach, the best fits between the Voigt-based model and the measured parameters ($\Delta f_{n=\alpha}$, $\Delta D_{n=\alpha}$, $\Delta f_{n=\alpha\pm|2\beta|}$ and $\Delta D_{n=\alpha\pm|2\beta|}$ where α=1, 3, 5... and β is a non-zero integer different from α) was done using a Simplex curve-fitting algorithm that searches for the unknown model parameters (d_f, η_f, μ_f) by minimizing the chi square, χ^2, given by:

$$\chi^2 = \sum_n \left(\frac{(\Delta f_n^{Voigt} - \Delta f_n^{measured})^2}{\sigma_n^f} \right) + \left(\frac{(\Delta D_n^{Voigt} - \Delta D_n^{measured})^2}{\sigma_n^D} \right)$$

Eq. 2.35

where Σn is the sum over all harmonics, n, measured; Δf_n^{Voigt} and ΔD_n^{Voigt} are given by eq. 2.33 and 2.34, respectively, $\Delta f_n^{measured}$ and $\Delta D_n^{measured}$ are the experimental values. σ_n^f and σ_n^D are the standard deviation for f and D at harmonic n.

To check whether the model inherent frequency dependence holds true, modeling was carried out on two sets of harmonics, n=3/5 and n=5/7 using identical start parameters. Both data sets led to the same qualitative picture, yet introduction of an additional linear frequency dependence for the elastic shear modulus and viscosity was sometimes necessary to produce equally good fits:

$$\mu(n) = \mu_{n=1}(1 + (n-1)\xi_\mu) \quad \text{and} \quad \eta(n) = \mu_{n=1}(1 + (n+1)\xi_\eta)$$

Eq. 2.36

where ξ (typically $-0.04<\xi<0.04$) determines the slope of a straight line. In this way, no additional unknown parameters are introduced, thus allowing an evaluation of the precision of the fit for various types of frequency dependencies.

2.4 DNA detection

Numerous genetic diseases are known, which are caused by single base mutations or deletions in the human genome. Methods capable of identifying those aberrations from small sample volumes with high specificity and sensitivity have great potential in the diagnostic and therapy of genetic diseases. The public is also interested in fast methods for the control of food products regarding genetically engineered ingredients In fundamental research, the sequencing of the genomes of many organisms currently produces a wealth of DNA material that has to be deciphered. For these reasons, much effort is currently made in order to improve existing surface-based DNA detection systems and to develop novel detection schemes [Zhai, 1997, Niemeyer, 1999], which are compatible with microarray formats. The improvement of available detection schemes requires a detailed knowledge of the DNA hybridization reaction. Surface-coupling chemistries and the control of the lateral density of DNA probes are crucial for the efficiency of those methods [Peterson, 2002]. Analytical approaches that have been proven efficient for this objective, include methods that utilize either fluorescence for end-point measurements [Niemeyer, 1999], evanescent field sensors for the analysis of reaction kinetics [Liebermann, 2000], piezoelectric [Larsson, 2002] and electrochemical [Heaton, 2001] biosensors. In the present work, two types of biosensor, QCM and SPFS, were used to study DNA hybridization and replication reactions at surfaces. The following chapter describes the building blocks of DNA and the conditions, which determine its stability in solution.

2.4.1 Structure and stability of DNA

The monomers of DNA, which are referred to as nucleotides (nt), consist of three subunits: a deoxyribose sugar, a base and a phosphate group [Saenger, 1983]. Linking the 3’ and 5’ OH of the sugar units via phosphodiester bonds creates a DNA strand. Therefore, the ends of a DNA strand are designated as 3’ and 5’-terminus. The C1 atom of the ribose is attached to one of the four naturally occurring bases, the purines, adenine and guanine, or the pyrimidines, cytosine and thymine. In single-stranded (ss) DNA, the distance between two successive phosphates is about 0.7 nm. The factors ruling DNA stability are manifold. In a DNA hybridization reaction, two complementary single strands of DNA become oriented in an anti-parallel manner to form double-stranded (ds) DNA via Watson Crick base pairing like depicted in fig. 2.13 [Watson, 1953].

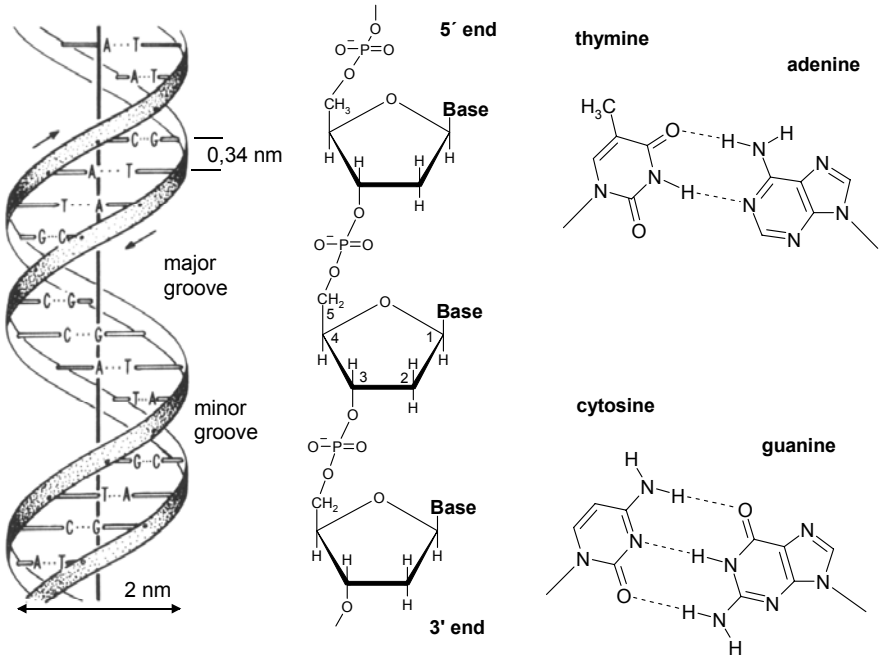

Figure 2.13: Schematic representation of the double helix (left) showing the minor and the major groove, a DNA single-strand illustrating the way the sugar units are linked via phosphodiester bridges (middle) and the H-bonding between specific Watson-Crick base pairs (right).

Base pairing is not solely driven by H-bonding between the complementary GC and AT base pairs, but also by nearest neighbor dependent base stacking interactions and the hydrophobic effect. DNA profits entropically from burying the hydrophobic bases in the inner part of the duplex by contacting the aqueous environment primarily via the charged phosphate-sugar backbone. A DNA duplex can adopt several conformations; the B-form is by far the most common one. The wound double helix is not perfectly symmetrical, it forms a 0.6 nm wide minor and a 1.2 nm wide major groove. The helix has a pitch height of 10.4 base pairs (bp) with a spacing of 0.34 nm between two stacked bases. The various factors stabilizing B-DNA also govern its local rigidity. The persistence length of ds-DNA is 45 nm, while ss-DNA is more flexible with a persistence length of ~1 nm at 150mM monovalent salt [Tinland, 1997]. Having a line charge density of 2 electrons per base pair, electrostatic forces contribute substantially to stability and flexibility of the DNA chain. At physiological conditions (0.1 M NaCl), the accumulated charge is compensated by Na^+ counter ions in proximity to the phosphate groups. The Debye-Hückel model is not ideally suited to calculate the charge distribution in the intimate proximity of DNA, since there, the electrostatic field is large compared to the thermal energy kT. It applies only for high ionic strength and in larger distances; the electric field is well described by the Debye-Hückel model for distances larger than twice the helix diameter in a 0.1 M solution of a 1,1-electrolyte (Debeye length ~ 1 nm). For a better approximation, one additionally introduces a Stern double layer in intimate contact to DNA and a Gouy layer bridging Stern and Debeye Hückel

regimes [Daune, 1997]. In the Stern regime the cylindrical shape of the electric field disappears and counter ions occupy distinct binding sites, which is accompanied by partial disruption of their hydration shells. The Gouy layer describes a condensed ion phase with only temporary formation of ion pairs. Within this regime, the surface concentration of counter ions does hardly depend on the ionic strength of the bulk solution. The interface between Stern and Gouy layer is responsible for the hydrodynamic behavior of a polyelectrolyte; here, bound solvent molecules are clearly distinguished from free bulk molecules. For DNA this interface has cylindrical shape with a radius of ~ 1.2 nm. The prevalence of electrostatic effects can be neglected in 100 mM monovalent salt solutions and higher.

Since DNA stability is ruled by many factors, it is difficult to predict the hybridization behavior of a certain sequence only on the basis of the calculated gain in Gibbs free energy. This is particularly true for hybridization reactions on metal surfaces, because the planar electric double layer formed at the metal/water interface superimposes with the electrical field of the immobilized DNA probes in a complex manner. Especially at high surface densities of DNA probes steric hindrances and electrostatic repulsions come into play, which are not accounted for by conventional computer routines calculating ΔG. However, we want to summarize the general features important for DNA stability:

- Content of GC base pairs: A high content stabilizes DNA, since GC base pairs are thermodynamically more stable than AT base pairs. In genomic DNA, the GC and AT content is identical, but the effect can be dramatic for short strands like applied in biosensors.

- Length of the DNA sequence: The melting temperature increases with length of the sequence.

- Nearest neighbor and end effects: The extent of base stacking interactions does not only depend on the number of neighbors, but also on their identity. Following trend has been reported for the influence of the two directly neighbored bases [Johnson, 1998]:
  GC>CG>GG>GA~GT~CA>CT>AA>AT>TA
  Frayed ends contribute an additional term to the stability.

- Presence of mismatched bases: As rule of the thumb, the melting temperature of ds-DNA is reduced by 1 % per introduced base mismatch for

DNA strands <100 bp. The destabilizing effect decreases if the overall length of DNA increases.

- Hairpin formation and self-complementarity: If DNA probes form stable hairpin structures, opening of the secondary structure consumes energy. Thus, ΔG_{ds} calculated for the hybridization reaction has to be corrected by ΔG_{hp} for hairpin formation: $\Delta G_{total}=\Delta G_{ds}-\Delta G_{hp}$. Hairpin stability depends on the identity and number of bases in the loop region as well as on the structure of the stem region. The minimum number of bases required to form a loop region is 4-5. The stability of the loop bases follows the trend: T-loop>C-loop>G-loop>A-loop [Senior, 1988].

- Buffer conditions: Destabilization of the DNA structure can be intentionally achieved by exposure to H-bond disrupting agents like urea or formamide or chaotropic salts that interrupt base stacking interactions. pH and ionic strength are crucial to hybridization, because duplex formation requires shielding of the charged phosphate backbone. In order to enhance the potential for single base mismatch discrimination, DNA hybridization can be carried out under destabilizing so called “low stringency” conditions that enable exclusively the fully complementary target DNA to hybridize.

2.5 Function of DNA polymerases

All living organisms require a mechanism for the efficient and accurate synthesis of DNA, thereby ensuring the faithful transmission of genetic information from one generation to the next. To achieve this objective, all organisms encode DNA polymerases that carry out the replication and repair processes required for normal cellular function [Kornberg, 1992]. These enzymes faithfully copy a DNA template by the stepwise addition of the appropriate deoxynucleoside triphosphate (dNTP) onto the terminal 3´-OH group of a DNA primer. The reaction occurs through a nucleophilic attack of the 3'-OH group of the growing DNA chain on the α-phosphoryl atom of an incoming dNTP. The reaction is energetically driven by the subsequent hydrolysis of the eliminated pyrophosphate, $P_2O_7^{2-}$ (fig. 2.14). In addition to the polymerase activity, many DNA polymerases exhibit a 3' to 5' exonuclease activity that allows for removal of incorrect nucleotides.

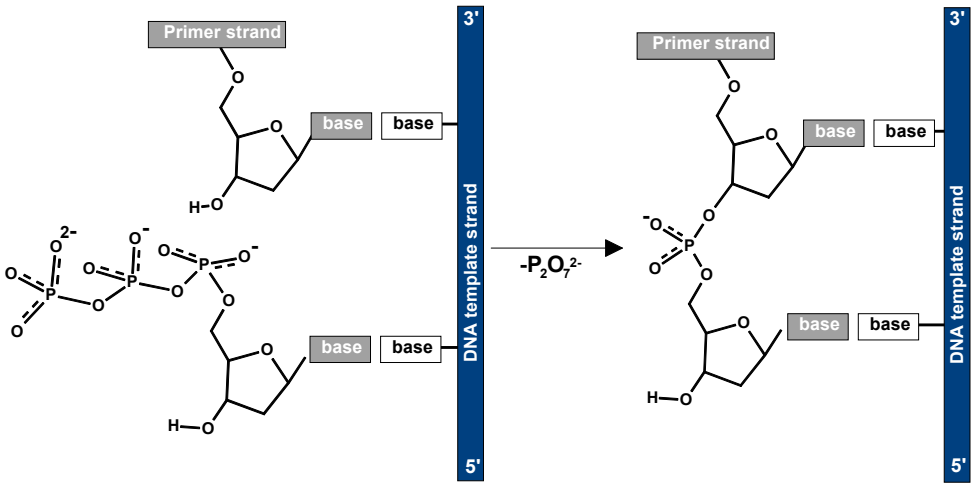

Figure 2.14: Reaction catalyzed by DNA polymerases. DNA polymerases incorporate deoxynucleoside triphosphates on single-stranded DNA templates such that the growing strand is elongated in 5' to 3'-direction.

DNA polymerases are a very diverse group of enzymes that differ vastly in size, cellular roles and replication fidelities. Despite this diversity, essential features of the active site have been conserved throughout evolution. From amino acid sequence comparisons, DNA polymerases can be organized into five families [Delarue, 1990]. This thesis focuses on the Klenow fragment of *E. coli,* which belongs to the best studied members of the Pol I family.

Detailed insights into the kinetic scheme of DNA replication and the molecular structures of DNA polymerases have been gained using rapid stopped/quenched flow fluorescence methods and X-ray crystallography. X-ray crystallography has provided

information on the three-dimensional structures of DNA polymerases (reviewed in [Jager, 1999, Steitz, 1999]). Polymerases from four of the five existing families fit the same pattern of "fingers", "palm" and "thumb" subdomains arranged in the form of half-open right hand. Co-crystal structures of DNA polymerases from the pol I and pol α families, with DNA substrates bound at the polymerase or 3´-5´ exonuclease sites, have also been reported [Beese, 1993]. Structural data are also available for ternary complexes of DNA polymerase, duplex DNA and nucleotide substrates. The ternary complex structures reveal two different conformations of the fingers subdomain that may correspond to the active (closed) and inactive (open) forms in the kinetic scheme. Figure 2.15 shows a schematic of the Klenow fragment in complex with a DNA duplex and the transition between an editing and an non-editing mode. The structure of the enzyme nicely exemplifies the hand-shaped structure of most polymerases.

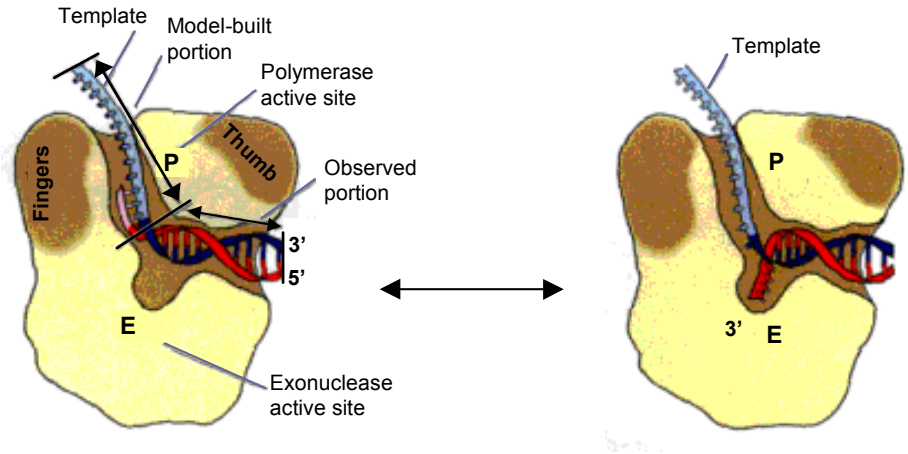

Figure 2.15: Schematic presentation of the Klenow fragment bound to DNA in the polymerizing (left) and the editing (right) mode. Due to the spatial separation of the two functional domains, the 3'-terminus has to translocate between the polymerase (P) and exonuclease (E) active sites.

In the kinetic scheme proposed to account for polymerase activity, the initial binding event of a DNA_n substrate (where n denotes the length of the primer strand) to the polymerase is followed by nucleotide binding and a subsequent slow rate-limiting "nonchemical" step that occurs at a rate of 50 s^{-1} [Kuchta, 1988]. Based on crystal structures of the ternary polymerase-DNA-nucleotide complex of the Klenow fragment and other DNA polymerases, the rate limiting step has been attributed to a conformational change of the polymerase-DNA-nucleotide ternary complex. The conformational change may correspond to a transition of the fingers domain between the open and closed conformations captured in the crystal [Li, 1998]. The crystal structures of the ternary complex also reveal differences in the local conformation of bases within the single-stranded template oligonucleotide. Depending on the conformational state, whether the first or the second base of the single stranded region

of the template, is rotated >90° from its normal position. This structural change is referred to as base flipping mechanism [Patel, 2001]. Transition from the open to the closed form is followed by the chemical step of nucleotide incorporation, another conformational change (presumably back to the inactive form), release of pyrophosphate, and finally, release or translocation of DNA_{n+1} product [Dahlberg, 1991].

This multistep process presents the polymerase with several points at which to discriminate between correct and incorrect nucleotides. The initial nucleotide binding step favors the correct nucleotide substrate, whereas the subsequent rate-limiting conformational change is strongly inhibited by an incorrect nucleotide substrate. The error rate for selecting the correct nucleotide is 10^{-5}-10^{-6}. If the polymerase does add an incorrect base, subsequent polymerization is slowed down greatly, which allows an opportunity for the misincorporated base to be removed by the polymerase's 3´ to 5´ exonuclease activity. This proofreading function reduces the error rate for DNA replication further to 10^{-10} [Kunkel, 2000]. To remove the misincorporated base, the 3'-terminus of the primer must translocate to reach the exonuclease site where it will be edited. This mechanism is known as active-site switching.

Different polymerases display different processivities, which refers to the tendency of a polymerase to be released from the DNA substrate after incorporation of a certain number of nucleotides. Low processivity combined with slow replication rates are typical of polymerases playing a leading role in DNA repair processes. The Klenow fragment is a typical representative of this class of polymerases with a low processivity of 1-100 bases and a replication rate of only 15 $nt \cdot s^{-1}$ [Dahlberg, 1991].

2.5.1 Relevance of DNA polymerases in biotechnology

Basically all methods for DNA detection make use of the specific hybridization of DNA probes of known sequence with complementary analyte DNA. The fact that each cell contains only a single copy of the DNA sequence of interest, makes high demands on the sensitivity of detection methods. Therefore, methods for DNA detection rely whether on the pre-amplification of analyte DNA or on the enhancement of the signal created by the hybridization reaction. In 1985, K. Mullis developed the polymerase chain reaction (PCR) [Mullis, 1990], which has rapidly emerged to be the most popular method to create high copy numbers of DNA. The technique employs repeated heating/cooling cycles to denature double-stranded DNA (template) that is subsequently hybridized to short primer oligonucleotides at moderate temperatures. The reaction mixture contains thermostable DNA polymerases, which specifically bind to primer-template complexes and faithfully replicate the template. Using this approach, initial

DNA concentrations of 10 copies per sample are sufficient to generate a considerable yield of DNA product. The presence of a particular base sequence in the PCR product can be easily proven by using conventional techniques such as fluorescent or radioactive labeling combined with gel electrophoresis. A recent advance in PCR was the development of homogenous assays that allow for the real-time detection and quantification of the PCR-amplified products. These methods make use of the possibility to create or extinguish a fluorescent signal as a function of the amount of amplification product. Commercially available is the TaqMan™ assay, in which an oligonucleotide labeled with a fluorophor in proximity of a quencher molecule at the 5'-terminus binds to the template DNA [Holland, 1991]. In the process of DNA replication, Taq polymerase removes the quencher molecule through its 5'-3' exonuclease function, and thereby spatially separates quencher and dye so that a fluorescence signal is obtained. Similarly work molecular beacons [Tyagi, 1996] like Amplifluor™ [Nazerenko, 1997] or Scorpions™ [Whitcombe, 1999] consisting of hairpin structures with a target recognition loop flanked by a fluorophor and a quencher on opposing ends. Binding to or incorporation into amplified DNA opens the hairpin and thereby abolishes the quenching effect.

The outstanding sensitivity of PCR makes it susceptible to contamination. Moreover; it needs further improvement regarding its performance in discrimination of point mutations and single nucleotide polymorphisms (SNPs). Therefore, the current trend points towards the combination of PCR with other enzymatic reactions in order to improve its specificity. Examples are the ligase chain reaction (LCR) [Barany, 1991], strand displacement amplification (SDA) [Little, 1999] or immuno-PCR [Sano, Smith and Cantor, 1992]. The interested reader is referred to the web page www.pcrlinks.com that extensively reviews variants of PCR techniques. Some of them are applicable in a microarray format meeting the emerging demand for high-throughput methods capable of screening a complex mixture of DNA or RNA for several target sequences. Since the present work is concerned with surface-based methods for DNA detection, the further discussion will concentrate on techniques compatible with microarray formats.

In LCR, two primers are hybridized to PCR-amplified DNA at adjacent positions. DNA ligase will join the primers only upon perfect hybridization. Favis *et al*. combined solution LCR and DNA microarrays for the detection of ligation products: Prior to exposure to the microarray, an allele specific probe was ligated to a fluorescently labeled probe [Favis, 2000] upon target hybridization. The allele specific probe additionally exhibited a zip-code permitting capture of the LCR product on a DNA array. This procedure uncouples signal detection completely from mutation identification occurring in solution.

Although PCR is efficient in amplifying target DNA, it requires sophisticated instrumentation to achieve fast and effective temperature control. Since realization of this requirement is especially challenging for array techniques, many isothermal methods working at a fixed (low) temperatures have been developed. The most promising surface-based approaches are strand displacement amplification (SDA) and rolling cycle amplification (RCA). SDA uses two types of primers (a bumper primer that displaces the amplification primer and a cleavable amplification primer) and two enzymes (DNA polymerase and a restriction enzyme) to produce single stranded amplicons asynchronously. The technique was successfully adapted for the amplification on a microelectronic chip [Westin, 2000]. Firstly, an electric field localized the biotin-labeled amplification primers. Than, template hybridization was performed applying another electric field and SDA was carried out in situ. The extended amplification primers were detected by hybridization to fluorescently labeled reporter oligonucleotides. Using this method 104 target molecules could be easily detected.

RCA is a new isothermal amplification method [Lizardi, 1998] that is useful for both, signal and target amplification, in a microarray format. One distinguishes linear RCA where circular DNA is hybridized to an immobilized complementary primer and amplified by polymerase extension of the primer. Up to 105 tandemly repeated, concatemerized copies of the DNA cycle are generated by each matching primer. Upon incorporation of radioactive or fluorescent labels, the signal caused by one hybridization event is strongly amplified. Though, the sensitivity of linear RCA is excellent allowing for detection of single molecules, it has the drawback to be limited to circular nucleic acids, such as circular viruses, plasmids and circular chromosomes. Exponential RCA uses a second primer complementary to the DNA cycle. Noncircular DNA was targeted and detected with outstanding allele discrimination using a combination of a ligase reaction with linear RCA. An anchored primer and a primer being complementary to a small surrogate DNA cycle were ligated upon hybridization to an DNA target. Successful ligation was indicated by repeated extension of the surrogate DNA cycle.

Adopting PCR to an anchored format is difficult due to technical constrains. Yet, methods capable of multiplexing are urgently needed to cope with the wealth of data available from the increasing number of genomes to be sequenced. Fast RNA expression profiling is as important as the quantification and functional study of translation products. The examples described above intriguingly demonstrate the efforts made to develop chip compatible methods for DNA detection, taking advantage of the fastness and accuracy of DNA polymerases in DNA replication. However, the majority of the methods rely on the analysis of the fluorescently labeled reaction products only, without providing insights into enzyme/DNA interactions. It is anticipated that studying these interactions in real-time not just satisfies a fundamental scientific interest, but provides valuable information having the potential to contribute to the improvement of

enzyme-based DNA detection methods. Future work should focus on the design of surface architectures not perturbing enzyme activity and on the elucidation of the influence of DNA secondary structures on the error rate and processivity of DNA polymerases.

3 Materials and Methods

3.1 Surface plasmon fluorescence spectroscopy

3.1.1 Experimental set-up

The set-up used for combined fluorescence and SPR measurements is depicted in fig. 3.1. The core parts of the SPR set-up are a HeNe laser (Uniphase, 5 mW, λ=632.8 nm), two polarizers, a 2-phase goniometer (Huber) and a photodiode. The flow cell is sandwiched between a quartz plate and a high index prism (Schott, 90°, LASFN9 glass) and mounted on the goniometer. The light ray is aligned such that it passes through the polarizers first and than hits the centre of the base of the prism. The function of the polarizers is to ensure TM-polarization of the excitation light and to adjust its intensity. After being reflected from the base of the prism, the light is collected by a lens (f=50mm, Ovis) and detected via a photodiode at an angle rectangular to the incident beam. In order to allow for noise reduced and daylight independent measurements of the reflected intensity, the photodiode is connected to a lock-in amplifier. The chopper modulates the incoming light with an adjustable frequency, usually 1300 Hz, that is identified and read out by the detector.

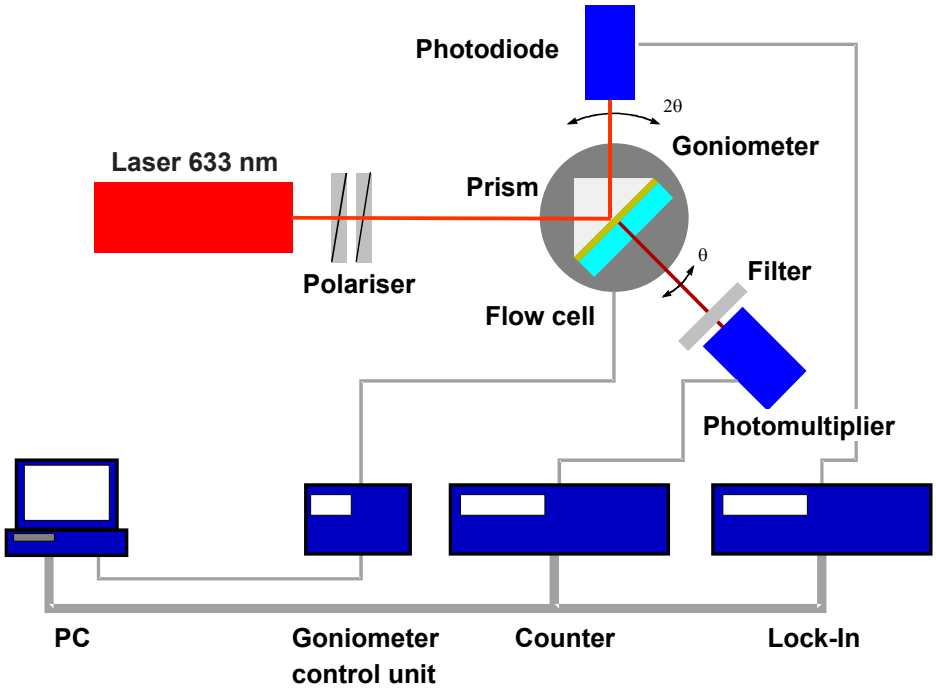

Figure 3.1: Set-up for combined SPR and fluorescence measurements.

Pinholes are inserted in the optical path to facilitate alignment of the incoming and reflected beam and to block scattered light. In order to take a scan measurement, the sample is rotated by moving the 2-phase goniometer stepwise (smallest step 0.001°). The whole set-up including the motors of the goniometer are remote controlled by a personal computer using the software WASPLAS. The sample is mounted onto two xy-tables and a tilting table, which allows for the optimal adjustment of the set-up.

In order to detect the fluorescence light irradiated from the sample through the quartz plate on the backside of the flow cell, a photomultiplier tube (PMT, Hamamatsu) is attached to the optical track behind the sample. This way, the PMT keeps its position perpendicular to the gold chip during rotation. Fluorescence light is focused using a collecting lens (f=50 mm, Ovis) and passes an interference filter ($\lambda = 670 \pm 2$ nm, LOT) before hitting the PMT. The PMT is connected to a counter (HP) via a photomultiplier protection unit. The protection unit closes the implemented shutter in front of the PMT if the irradiation exceeds a predefined level in order to avoid damage of the sensitive fluorescence detection equipment. In addition an external shutter is introduced into the optical path that opens only during data acquisition in order to prevent the sample from photo-bleaching.

3.1.2 Preparation of the flow cell

Side and top view of the flow cell are shown in fig. 3.2. It is a home-built cell constructed from a quartz plate (Herasil, Schott) with an inlet and an outlet (diameter: 1 mm) at indicated positions. The circular inner part of the cell has a radius of 3 mm and a height of 2 mm confining the volume to ~60 µl. The flow cell is sandwiched between a quartz plate (Herasil, Schott) and a glass waver which is evaporated with a thin gold film. The gold covered surface points towards the cell. The contact areas between these components are sealed by O-rings made from Viton. A high refractive index prism (LaSFN9; n=1.845) is mounted on top of the glass waver. In order to improve the coupling between incident light and SP modes, the glass waver and prism are connected via a thin film of refractive index matching oil (n=1.7). The use of matching oil with a refractive index lower than that of the prism is reasoned by the high vapour pressure of oils exhibiting higher refractive indices. A metal sample holder holds the sample in place on the goniometer during the measurement. All measurements were performed upon a constant flow rate of 2 ml/ min.

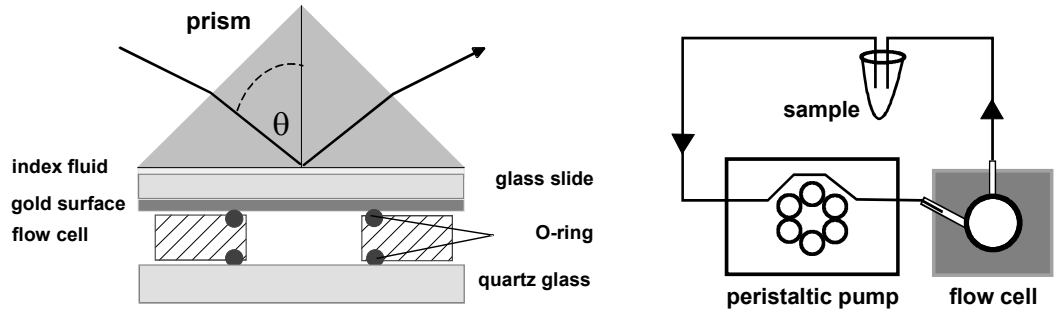

Figure 3.2: Construction of the measurement chamber (left) and top view of the flow cell including a schematic of the circulation loop (right).

The flow cell is connected to a peristaltic pump (Ismatec) and the sample reservoir using tygon tubes with an inner diameter of 0.76 mm. Thus a closed circulation loop is formed which is disconnected during the injection phase. The total volume of the loop amounts to 300 µl, therefore injection volumes between 1-1.5 ml have been used to ensure the desired analyte working concentration.

3.1.3 Recording of SPFS spectra

In general, one has two options to record the shift in the resonance angle for SP excitation induced by interfacial refractive index changes: the scan and the kinetic mode.

Scan mode

A scan curve monitors the intensity of the light reflected at the base of the prism as a function of the angle of incidence. Experimentally, it is monitored by rotating the goniometer over a certain angle range, while the photodiode records the intensity of reflected light. A typical example for a SPR scan spectrum is given in fig. 3.3A.

Kinetic mode

Alternatively, one might fix the angle of incidence and monitor the changes in reflectivity as function of time. The kinetic mode allows to observe surface reactions in real-time. By definition, the angle chosen for kinetic measurements was the one corresponding to 30% reflectivity. If gold films of similar thickness (~50 nm) were employed, which in turn means that the depths of the SP curves are identical, this angle corresponds to the linear region of the SP curve. If so, the created reflectivity signal is proportional to the change of the resonance angle. The causal connection between scan and kinetic curves is explained in fig. 3.3B.

Every SPR experiment started with monitoring a scan spectrum of the blank gold surface immersed in the respective buffer. Thereby, the angle range to sweep through was chosen such that the region for total internal reflection and the whole resonance minimum of the SP could be observed. That way, the angle range contains all information critical for determination of the film thickness. In aqueous solution this angle range is between 44° and 65° (for an LASFN9 prism). Thereafter, the adsorption of a thin film was observed in the kinetic mode until adjustment of a new equilibrium. Finally, a second scan spectrum was recorded in order to make sure that reflectivity changes observed in the kinetic mode did not originate from changes in the shape of the SP or shifts of the critical angle.

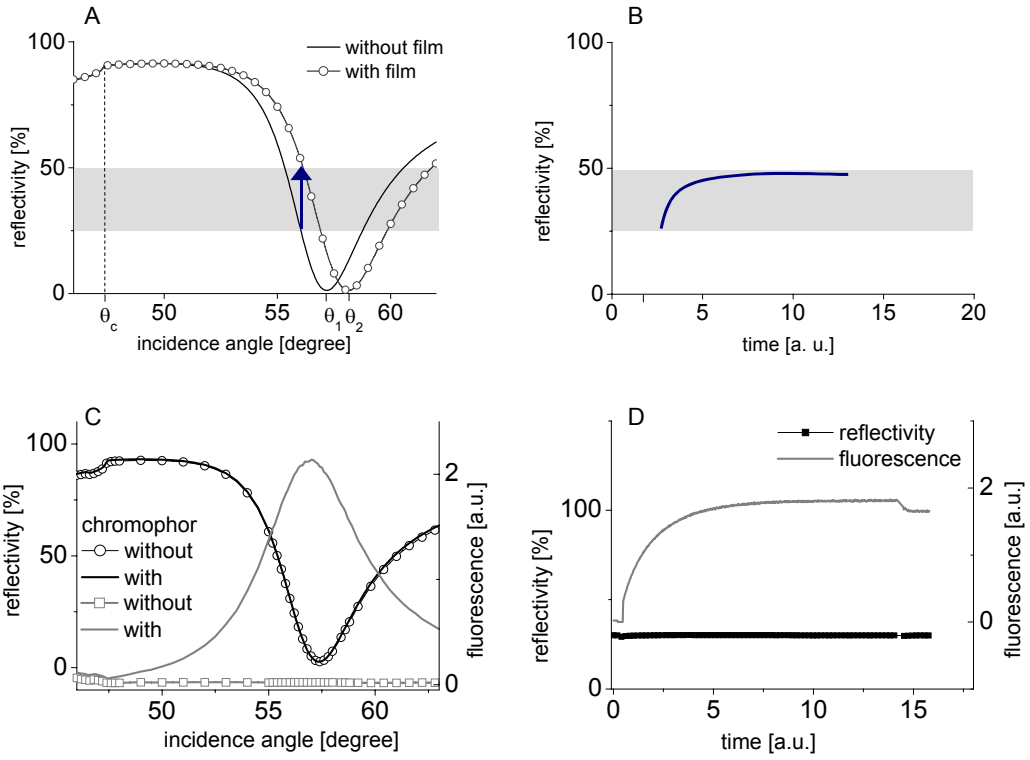

Figure 3.3: Connection between SPR measurements acquired in scan mode (A) and kinetic mode (B). Note that the reflectivity is increased if one observes the shift of the scan curve at a fixed angle of incidence (indicated by the black arrow). Also shown are scan (C) and kinetic (D) modes as obtained from SPFS experiments.

Fluorescence monitoring

The fluorescence light emitted from dye-labeled probes was either monitored in the scan or in the kinetic mode like described for the SPR spectra with the PMT on the backside of the flow cell switched on. If the use of fluorescent probes was limited to surface reactions that were attributed to very low mass changes, the resonance angle for SP excitation remained unchanged, corresponding to a horizontal line in the SPFS kinetic spectrum (3.3D). As depicted in the SPFS scan spectrum (3.3C), the fluorescence increased from the background value to a value determined by the dye

concentration. Thus, if the resonance curve of the SPs does not shift, a linear relation between dye concentration and fluorescence intensity exists. The quantification of the fluorescence signal in the kinetic mode is more complicated in such cases, where the resonance angle changes simultaneously with the surface concentration of dye. Than, the intensity of the evanescent field of the SP changes for a fixed angle of incidence and hence, the intensity of the excitation field. In this case, deviations from the linear relation between concentration and fluorescence intensity are expected. For the reactions presented in this thesis, those deviations play a minor role since the observed mass changes were small.

3.1.4 Data analysis

If the geometry and the dielectric constants of a layer system are known, the SPR scan spectrum can be theoretically predicted using a transfer matrix algorithm giving the thickness increase caused by a surface reaction [Karthe, 1991]. The software WINSPALL working on the basis of this algorithm was used to analyze the experimental data.

In a first simulation, the reference scan spectrum that was monitored before film adsorption was analyzed. This spectrum is the result of the reflection and emission of electromagnetic waves in a layer system consisting of prism, metal and solvent at resonance conditions. As the optical constants for the prism and the buffer were known (ε'_{LASFN9}=3.4069 and ε'_{Buffer}=1.778 for λ=632.8 nm) and the thickness of these layers could be assumed as being infinite, only the parameters for the metal layer had to be adjusted. The start parameters used for the simulation of a gold layer were ε'= -12,3, ε''= 1.29 and thickness, d= 50 nm. Using an iterative fitting routine, these parameters were varied until the best agreement between fit and raw data was achieved. The thickness of any further adlayer was determined by comparison of the reference scan spectrum with the scan spectrum obtained upon completion of the adsorption process. In order to model the corresponding spectrum all parameters were kept fixed except for the thickness of the newly-created adlayer (as a pre-requisite the optical constants of the adlayer must be known). By knowing the final thickness increase for an adsorption process, the reflectivity data recorded in the kinetic mode can be easily translated into thickness data. Note that the optical thickness does not necessarily correspond to the real dimensions of a film but should rather be considered as an effective thickness. Only if the films are dense and perfectly homogenous, the transfer matrix algorithm gives a good estimation of the real thickness.

Thickness data acquired by SPR spectroscopy were converted into a mass-uptake per area using eq. 2.19 (c. f. chapter 2.1.5).

3.2 QCM-D technique

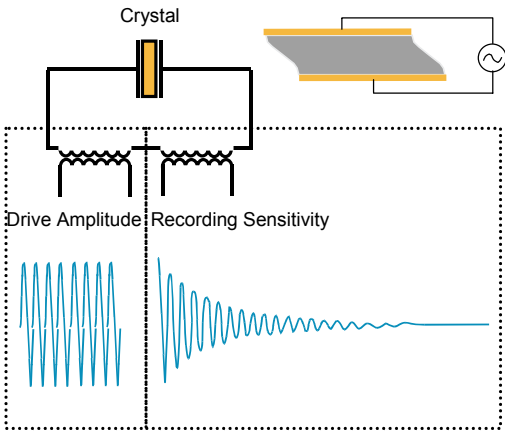

Figure 3.4: Principle underlying the QCM-D measurements. The quartz crystal is driven to perform shear oscillations by applying an alternating voltage. After disconnection from the driving circuit, the voltage over the resonator decays as an exponentially damped sinusoidal. Numerical fitting of the sinusoidal provides the resonance frequency and dissipation factor of the system.

The QCM-D measurements were done using a commercial set-up, the Q-Sense™ D300 system (Q-Sense AB, Göteborg). For a detailed technical description of the set-up see the references [Rodahl, 1995, Rodahl, 1996]. Using this technique, changes in the resonance frequency, Δf, and in the dissipation factor, ΔD, of a quartz crystal were recorded simultaneously as a function of the mass-load. The principle of the measurement is the periodical disconnection of a quartz crystal, being a piezoelectric resonator, from an electric driving circuit. After disconnection of the driving voltage, the voltage over the resonator decays as an exponentially damped sinusoidal. Thereby, the dissipation factor is inversely proportional to frequency and relaxation time of the quartz (see chapter 2.3.3). The decay of the oscillation is monitored on a digitizing oscilloscope and the signal numerically fitted with a time resolution of max. 10 data point per second. The principle of the measurement is depicted in fig. 3.4.

The smallest detectable signals in Δf and ΔD are 0.02 Hz and 0.1×10^{-6} at optimal conditions when data points are acquired with a rate of 4 points per second. This corresponds to a mass sensitivity of about 3.5 ng/cm^2.

The QCM-D measurements were performed using AT-cut quartz crystals with fundamental frequencies of 5 MHz (Q-Sense AB, Göteborg). The electric field is applied via polished gold electrodes deposited on the quartz in a keyhole pattern (fig. 3.5A). In each experiment, Δf and ΔD were recorded up to the 4th harmonic of the quartz simultaneously. The QCM-D set-up was controlled using the software QSoft 3.01™, curve fitting was performed using QTools™2. The Voigt-based viscoelastic presentation used for the modeling of the experimental data is explained in chapter 2.3.5.

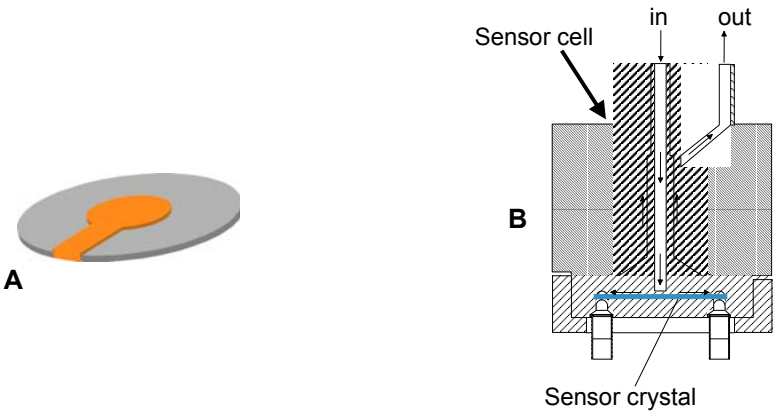

Figure 3.5: Quartz crystal with keyhole-shaped electrodes (A). Axial flow chamber used for QCM-D measurements.

Measurement Chamber

Experiments were performed either in batch mode, in a cell that provides a rapid (<1 s) non-perturbing exchange of buffer solutions (axial flow chamber, Q-Sense AB, Göteborg) or under a constant buffer flow of 0.2 ml/ min using the same cell driven by a peristaltic pump (fig. 3.5B). In the axial flow chamber, the quartz crystal is seated horizontally with the inlet approaching the inner volume of the cell from the top (along the surface normal). The volume of the chambers is adjustable from 50 to 100 µl, the minimum injection volume was 1 ml. During data acquisition the reaction cell was temperature-stabilized with an accuracy of ±0.1°C.

3.3 Surface modification techniques

The surface architecture, invariably used in QCM-D and SPFS experiments, consisted of a gold surface modified by a self-assembled monolayer (SAM) of biotin-modified thiols that functioned as anchor for the immobilization of a streptavidin monolayer. Depending on the experiment, biotinylated oligonucleotides of different base sequence were bound on top of the streptavidin layer. Experiments were carried out aiming at the properties of the oligonucleotide probes in hybridization assays and at their elongation using the Klenow fragment of E. *coli* DNA polymerase I. In the following, some fundamentals regarding the functionalization of gold films with thiols and the streptavidin/biotin affinity system will be given. Cleaning procedures, assay conditions and the sequences of the oligonucleotides can be found in the appendix.

3.3.1 Self-assembled monolayers on gold

The surface material to be modified in all experiments was gold. In the ideal crystalline structure of gold, the gold atoms are ordered in a face centred cubic (fcc) lattice, where each gold atom has twelve nearest neighbours. This symmetry is disturbed at the surface; here, gold forms terraces with a so called (111) structure. In this structure, the number of nearest neighbours is reduced to six for a gold atom located at the surface. However, gold surfaces prepared by thermal evaporation are actually polycrystalline. Irrespective of their precise structure, gold surfaces are highly reactive due to the unpaired 6s electron of the gold atoms. The remarkable reactivity is responsible for the self-assembly of molecules at the solid-liquid interface. Self-assembled monolayers (SAMs) are known to be molecular, highly ordered assemblies formed spontaneously by the immersion of an appropriate substrate into a solution of an active surfactant in an organic solvent [Ulman, 1991]. SAMs are thermodynamically extremely stable; thus, they provide a simple and efficient method for surface modification. Several excellent reviews are concerned with their application in the field of biosensors, biomaterial, lubricants and anti-corrosion films [Swalen, 1987, Wink, 1997].

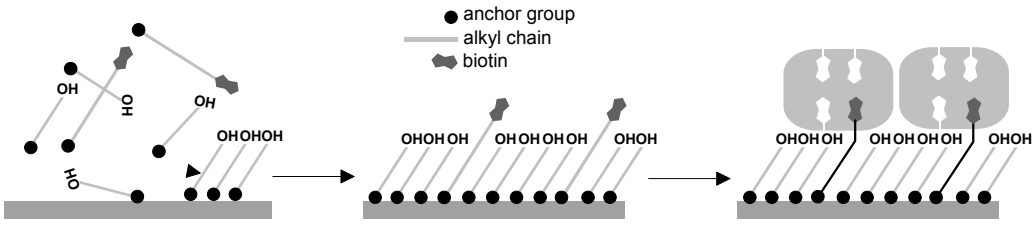

Figure 3.6: Schematic of the self-assembly process. The anchor group, in this case S-H, has a strong chemical affinity to the gold surface. A covalent Au-S-bond is spontaneously formed by the mere exposure of the thiol solution to the gold surface. In the course of the reaction, all available binding sites on the gold surface are occupied by thiol molecules. The alkyl-chains adopt a parallel orientation with a uniform tilt angle of 30° relative to the surface normal. Such a highly ordered surface architecture meets perfectly the steric requirements for streptavidin binding (right cartoon).

From the thermodynamic point of view, the self-assembly process is promoted by several factors: One driving force is chemisorption, which is based on the high chemical affinity between the head group of the surfactant and the surface. These interactions are strongly attractive and lead to formation of a thermodynamically favored covalent bond. As a result, the surfactant molecules try to occupy every available binding site on the surface. Well-studied representatives of this class are alkanethiols assembled on noble metal surfaces such as gold, silver or platinum. The second driving force is physisorption. This process is not accompanied by a chemical reaction but relies on electrostatic interactions between adsorbed molecules. A typical example is the

alternating adsorption of polyelectrolyte layers of opposite charge. SAMs are often further stabilized by interactions between neighbored molecules in the film. For instance, alkyl chains may interact via van der Waals forces or the presence of polar bulky groups can give rise to electrostatic interactions.

In the present work, a binary mixture of thiols was routinely used to functionalize a gold surface. The typical picture for the chemisorption of thiols on gold is that the thiol loses its hydrogen atom and becomes a thiolate covalently bound to the gold surface. The exact mechanism for Au-S bond formation has not been entirely elucidated. The literature suggests two models which only differ in the oxidant involved in the reaction, which is either protons or oxygen [Ulman, 1991]:

$$2\,R-SH+2\,Au(0)\longrightarrow 2\,R-S-Au(I)+H_2$$

$$2\,R-SH+2Au(0)+\frac{1}{2}O_2\longrightarrow 2\,R-S-Au(I)+H_2O$$

Typical of thiol SAMs is a uniform tilt angle of ~30° against the surface normal for each thiol chain [Samant, 1991, Siepmann, 1993], whereby each molecule occupies a surface area of ~21 Å [Swalen, 1987].

The used thiol mixture consists of a long chain thiol modified with a biotin head group (11-mercapto-(8-biotinamido-4, 7, dioxaoctyl-)-undecanoylamide) and 1-mercapto-undecanole at a ratio of 1 : 9 in ethanol. The chemical structures are shown in fig. 3.7. Fig. 3.6 shows schematically the formation of a mixed thiol SAM and its subsequent coverage with streptavidin molecules. The binding properties of a biotinylated SAM can be largely improved by spacer thiols of appropriate length and by a considerable dilution of the biotin binding sites. This is attributed to steric requirements of the binding reaction during which the biotin has to reach the binding pocket which is relatively deep inside the protein. The OH-terminated thiol has two functions: firstly, it acts as lateral spacer optimizing biotin binding and secondly, it creates a chemical environment being resistant to unspecific adsorption of many biomolecules. As described in recent publications, the mixing ratio has been optimized to bind a maximum amount of streptavidin [Knoll, 2000].

The SAM was prepared ex-situ by immersion of a gold slide in a 0.1 mM solution of thiols in ethanol for at least one hour. During incubation, the gold slide was kept in a chamber whose atmosphere was saturated with ethanol. After rinsing with ethanol, the gold slide was dried in a nitrogen stream and mounted onto the flow cell.

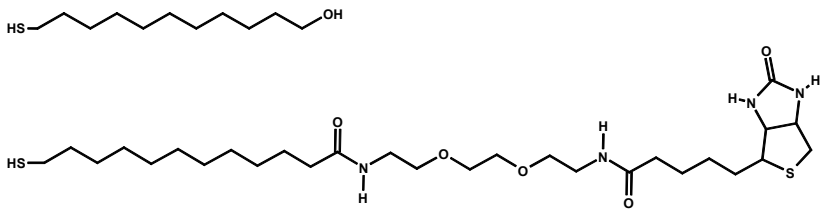

Figure 3.7: Chemical structure of 11-mercapto-(8-biotinamido-4, 7, dioxaoctyl-)-undecanoylamide (bottom) and 1-mercapto-undecanole (top).

3.3.2 Streptavidin

In the present work, a streptavidin layer, anchored to the gold surface via biotin-modified thiols, was used to couple biotin-modified oligonucleotides to the sensor surface. Streptavidin is a tetrameric protein (molecular weight 4 × 15 kDa), which was isolated from the actinobacterium *Streptamyces avidinii*. Each subunit is able to bind a molecule of d-biotin with an extraordinary high binding affinity and an exceptionally slow dissociation rate in solution ($K_d=10^{-15}$ M^{-1}) [Chilkoti, 1995, Weber, 1989].

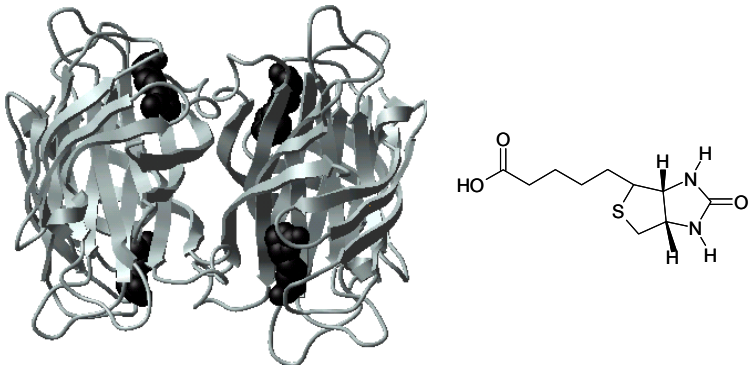

Figure 3.8: Molecular structure of a single streptavidin tetramer. Four biotin molecules (chemical structure on the right side) are depicted using a ball and stick model.

Providing a method for irreversible coupling, combined with its outstanding resistance against chemicals and temperature fluctuations, makes streptavidin immobilization a widely spread method in bioanalytical applications like the construction of biosensors and DNA microarrays [Wilchek, 1988]. Grown on biotin-doped lipids, streptavidin was shown to form 2-dimensional (2D) crystals [Darst, 1991], with two of the four binding sites contacting the lipid bilayer and the other two pointing into the bulk phase. The height of such a 2D crystal was confirmed to be 4.7 nm by high-resolution atomic force microscopy [Scheuring, 1999] as well as ellipsometric data [Reiter, 1993]. The dimension of a single tetrameric streptavidin molecule was determined to be 5.6 nm × 4.2 nm × 4.2 nm by x-ray crystallography (fig. 3.8) [Weber, 1989]. As will be shown in chapter 4.2, the thickness of the thiol-supported streptavidin layer measured

by SPR is in good agreement with the height of a single streptavidin molecule. In the scope of this work, the usefulness of the streptavidin monolayer as laterally diluted, highly reproducible platform for oligonucleotide immobilization will be demonstrated. The lateral dilution of biotin binding sites guarantees a low coverage with oligonucleotides. That reduces fluorescence quenching between neighbored DNA chains and steric hindrance during DNA hybridization and replication reactions.

4 Real-time monitoring of DNA replication using SPFS

4.1 Experimental design

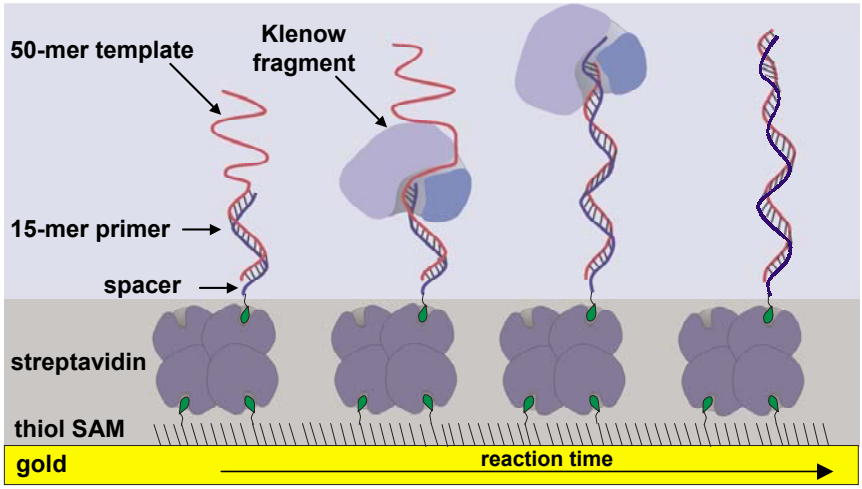

Figure 4.1: Schematic representation of the sensor architecture utilized for studies of DNA hybridization and polymerization reactions. In the course of DNA replication, primer oligonucleotides are elongated in the presence of a DNA polymerase and dNTP substrates leading to completely double-stranded DNA.

Fig. 4.1 shows the surface-coupling chemistry used in SPFS and QCM-D experiments. A self-assembled monolayer of biotinylated thiols served as a matrix for binding of streptavidin. The streptavidin layer was utilized to bind 5'-biotinylated oligonucleotides (denoted as primer or probe) consisting of a 15-mer recognition sequence and a poly-thymine spacer. Depending on the length of the spacer sequence, the primers are referred to as P15 (no spacer), P30 (15 thymine) and P45 (30 thymine). A 50-mer oligonucleotide (template or target) with a 15-mer sequence being complementary to the primer's recognition sequence was hybridized in order to create a substrate for DNA polymerase binding. The hybridization reaction produces a DNA substrate with a 5' overhang of 35 nucleotides. Template-directed DNA synthesis requires such a double-stranded DNA with a recessed 3'-terminus. The longer, coding strand is referred to as template, while the shorter strand is designated as primer. The Klenow fragment (KF) binds specifically to the 3'-terminus of the primer and recognizes the first base on the single-stranded part of the template. Addition of the complementary deoxynucleoside 5' triphosphate (dNTP) to the 3'OH of the primer strand creates a 3'-5' phosphodiester bond upon release of pyrophosphate. As a consequence, the primer is extended in 5' to 3'-direction. For mechanistic details see chapter 2.5.

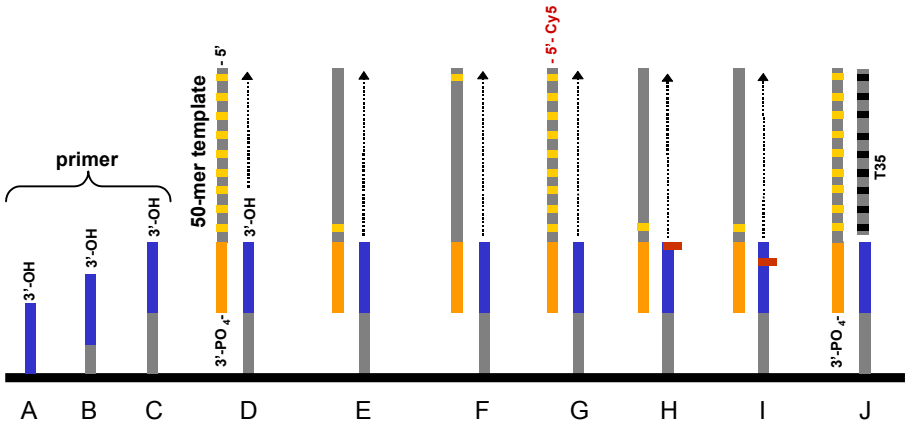

Figure 4.2: Nomenclature of the DNA substrates. The 15-mer primers (blue) had identical base sequences but differed in the length of their poly-thymine spacers (gray). All primers were modified with biotin at the 5'-terminus via $[-(CH)_2-]_6$ linkers. The 50-mer templates differed in the number and position of guanine bases. Each yellow square symbolizes a guanine base that can be paired with Cy5-labeled dCTP during the polymerization process. The red squares indicate the presence of a GG mismatch in the primer/template part. The DNA substrates were named as follows:

- **A: P15 → 15-mer primer without spacer**
- **B: P30 → 15-mer primer + spacer of 15 thymines**
- **C: P45 → 15-mer primer + spacer of 30 thymines**
- **D: P45/T50 → P45 hybridized to T50 etc.**
- **E: P45/T50G1close**
- **F: P45/T50G1far**
- **G: P45/ 5'-Cy5-T50**
- **H: P45 tG/T50G1close**
- **I: P45 iG/T50G1close**
- **J: P45/T35/T50 → P45 hybridized to T50 and to T35, a 35-mer oligonucleotide being complementary to the single-stranded part of the template.**

Labeling of the synthesized strand is achieved by incorporation of Cy5-labeled dCTP at the positions opposite to guanine bases on the template strand. Wild type KF also corrects for mistakes in DNA by removing mismatched nucleotides from the 3'-primer terminus. This 3' to 5'-exonuclease activity can be removed by a double amino acid exchange (Asp^{355}→Ala; Glu^{357}→Ala) without affecting the binding characteristics and the polymerase activity. If not mentioned explicitly otherwise, the commercially available exonuclease-free mutant has been used in the experiments.

Scheme 4.2 illustrates the various primers and templates that were used during the course of this thesis; important features like the number of guanine bases, single base mismatches and the length of the oligonucleotides are schematically depicted. The reader is asked to consult this chapter for the nomenclature of the templates and DNA constructs.

4.2 Characterization of the standard surface architecture

Basis for all experiments was the reliable immobilization of DNA strands on gold surfaces. Towards this aim, surface modification was routinely carried out by formation of a multi-layer architecture consisting of a self-assembled monolayer of biotinylated thiols, a 2D streptavidin arrangement and a layer of 5'-biotinylated DNA hybridized to complementary unmodified DNA. Surface preparations are described in the appendix a-e. Whereas thiol and streptavidin layers were identical in all experiments, DNA strands varied in length and sequence. The by far most often used DNA construct was a 5'-biotinylated P45 being a 45-mer oligonucleotide with a 30-mer poly-thymine spacer and a 15-mer recognition sequence. P45 was utilized as catcher for T50, a 50-mer oligonucleotide being partially complementary to the recognition sequence. 35 of the 50 nucleotides are not involved in hybridization and remain single-stranded, acting as a template in DNA replication. Complete DNA replication generates complementary 35-mer strands that are covalently linked to the 3'-terminus of P45. The sequences of the oligonucleotides can be found in appendix f.

Fig. 4.3a shows SPR kinetic curves for the adsorption of every single layer of the surface architecture except for the thiol SAM, which has always been prepared ex situ. The SAM has been extensively studied in previous works [Knoll, 2000, Häussling, 1991] and was found to be ~1.5 nm thick. A reaction step shown in addition to the probe immobilization and template capture is the hybridization of T35 to P45/T50. The oligonucleotide T35 exhibited exactly the sequence to be synthesized in the course of DNA polymerization. It was hybridized to the single-stranded part of the template in order to simulate the SPR response expected for complete replication of the template. Scan curves were monitored before and after each immobilization step (fig. 4.3b). Using the software WINSPALL that utilizes a Transfer-Matrix algorithm to simulate the amount of reflected and transmitted light at each layer, the corresponding scan curves were theoretically reproduced. Assuming a fixed complex dielectric constant ($\varepsilon' = \varepsilon' + i \cdot \varepsilon''$) for each type of molecule, effective thickness (d) values were derived and converted into surface coverage using eq. 2.19. The experimental variation was ±0.1 nm for streptavidin and ±0.25 nm for the various DNA films. The results are summarized in table 1.

The thickness of the streptavidin layer was found to be about ~4 nm. The dimensions of a single streptavidin tetramer are 5.6 nm × 4.2 nm × 4.2 nm as determined by X-ray scattering [Weber, 1989]. Accordingly the height as well as the experimentally found surface coverage is in good agreement with a monomolecular arrangement of streptavidin. Each streptavidin molecule offers two binding pockets for biotin with a center-to-center distance of 2.5 nm [Darst, 1991]. Considering the helix diameter of 2 nm, two DNA strands bound to the same streptavidin molecule are likely to contact each other, which causes electrostatic repulsion.

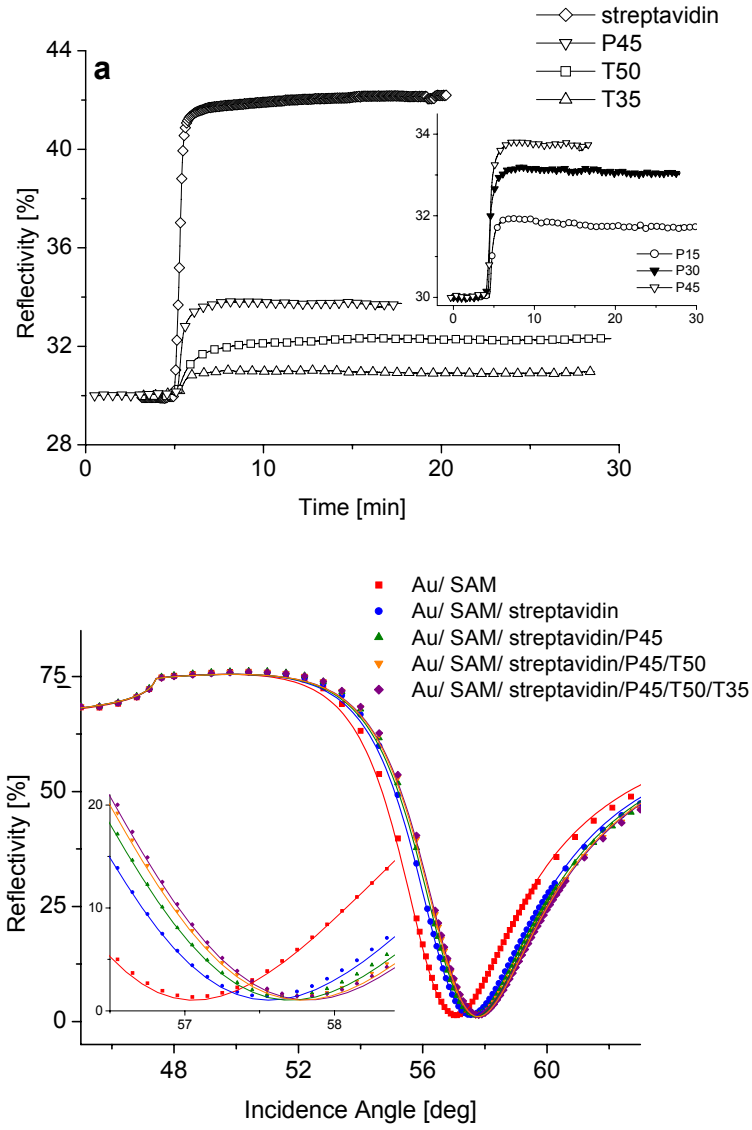

Figure 4.3: a) SPR kinetic curves for the stepwise formation of a multi-layer system consisting of: Au/thiol SAM/streptavidin/duplex P45/T35/T50. The inset compares the kinetics for binding of the primers P15, P30 and P45, respectively. b) SPR scan curves recorded after each immobilization step shown in a. The red curve corresponds to the gold surface covered by the thiol SAM. The streptavidin layer (blue) was utilized as platform for primer binding. P45 (green) was immobilized and hybridized to T50 (orange) and T35 (purple) in two steps. Hybridization of T35 to duplex P45/T50 simulates the response expected for complete replication of template T50. Raw data are plotted as scatter, plasmon fits produced using the program WINSPALL are given as solid lines.

According to the molar surface concentrations for streptavidin and P45, only 62 % of the biotin-binding pockets harbor DNA strands (assuming two available biotin binding sites per streptavidin molecule), which is probably due to steric hindrance. Note that the assumption of identical optical constants for single- and double-stranded DNA gives possibly rise to errors. Therefore one should be careful when calculating the efficiency of target hybridization from molar surface coverages obtained from SPR experiments. For instance, the molar concentrations determined for T50 hybridization (2.3 pmol/cm^2) corresponded to only 48 % coverage of the primer strands (5.6 pmol/cm^2). This is

remarkably small for a 15-mer recognition sequence with a GC content of 60 %. Even more unlikely is that hybridization of T35 results in a surface concentration of 1.6 pmol/cm^2, although a 35-mer should be more stable than a 15-mer. Causing a shift in reflectivity of only ~1 %, the mass added upon hybridization of T35 is very close to the detection limit. Experiments in which T50 has been hybridized to oligonucleotides P15 and P30 (identical to P45 but without and with 15-mer thymine spacer, respectively) demonstrated that the mass detected in this reaction did not depend on its position relative to the surface. Rather, the SPR signal for T50 hybridization was identical in the three sets of experiments, although the DNA probes exhibited different spacing distances to the surface. From these experiments, one can conclude that it is not the weaker plasmon field at larger distances to the surface that causes a reduced sensitivity for target detection. The error is more likely caused by using identical refractive indices for single-and double-stranded DNA, which hold strictly only for dense, homogenous layers but not for laterally diluted films.

The inset in fig. 4.3b also shows immobilization of the probes P15 and P30. Similar to QCM-D measurements, the mass increase observed for P15, P30 and P45 immobilization were almost linear with a small deviation for P15. The amount of P15 and P30 bound on top of streptavidin was 31 ng/cm^2 (6.9 pmol/cm^2) and 51 ng/cm^2 (5.6 pmol/cm^2). Thus, a slightly higher surface coverage was achieved for binding of the shorter oligonucleotide P15, being most likely reasoned by reduced Coulombic repulsion between the two binding pockets on one streptavidin molecule.

Table 1: Thickness parameters of the components of the DNA biosensor as obtained from SPR.

Layer	$d_{effective}$ [nm]	ε’	ε’’	Surface Coverage [ng/cm^2] (pmol/cm^2)	Refractive Index Increment [ml/g]
Gold	48	-12.3305	1.4991		
Thiol SAM[a)]	1.5	2.25	0		
Streptavidin	3.8	2.1025	0	209 (3.5)	0.212[b)]
P15	1.3	1.8903	0	31 (6.9)	0.19[c)]
P30	2.1	1.8903	0	51 (5.6)	0.19
P45	2.8	1.8903	0	66 (4.7)	0.19
T50	1.5	1.8903	0	36 (2.3)	0.19
T35	0.7	1.8903	0	17 (1.6)	0.19

a) Using electrochemical methods, the surface coverage was determined to be 4.5×10^{14} molecules/cm^2 [Zitzlsperger, 1998].
b) [Liebermann, 1999]
c) [Larsson, 2003]

4.3 Binding of DNA polymerase to surface-attached oligonucleotides

The previous section discussed the construction of DNA substrates suited for DNA polymerase binding. 12 % of the streptavidin molecules were found to carry two primer strands, the remaining molecules exhibited only one primer strand. Yet, it is not entirely clear from the available data, if they quantitatively hybridize to the template strand. Considering KF's hydrodynamic radius of 3 nm, a surface area of $4.2 \times 5.6\ \text{nm} \approx 24\ \text{nm}^2$ as provided by a streptavidin molecule carrying only one DNA duplex, should be sufficient to prevent from strong steric hindrance between neighboring KF molecules. However, small separation distances between KF and the surface might also impair the function of the enzyme. Therefore, KF was bound to two different, namely duplex P15/T50 and duplex P45/T50. Duplex P15/T50 is identical with P45/T50 except for the fact that the spacer region is missing. The double-stranded part of the primer/template hybrid is 15 bp in both cases and the single-stranded part of the template is 35 bases long. Co-crystal structures of KF bound to duplex DNA revealed that the enzyme directly contacts 7-8 nucleotides of the duplex via its sugar-phosphate backbone [Li, 1998]. Accordingly a 8 bp primer/template duplex would offer enough space for KF binding; but a 8 bp duplex is thermodynamically too unstable at room temperature and needs to be stabilized by introduction of covalent bonds. However, longer duplexes bear the risk of forming multiple complexes with more than one KF molecule bound per DNA substrate. Since typical binding sites for DNA

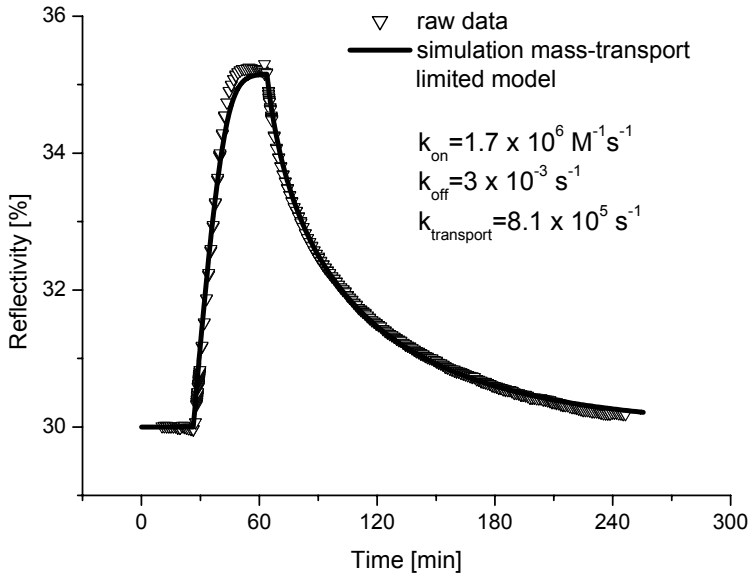

Figure 4.4: Single binding curve for the immobilization of the KF on duplex P45/T50. KF was bound from a 7.6 nM solution and could be entirely removed by rinsing with buffer, which demonstrates the reversibility of the reaction. A mass-transport limited 1:1 binding model was employed to represent the binding curve.

polymerases exhibit 5'-overhanging bases, formation of a 2:1 KF: DNA complex is not very likely as long as this site is unique. Yet, introducing a poly-thymine spacer like in P45/T50 creates a second recessed 3'-terminus. In order to inhibit its extension, the template's 3'-terminus has been protected using a phosphate group. Although this excludes the polymerase reaction, KF binding could still be possible. Therefore the overall binding capacity of the DNA substrates described above was examined and compared in titration experiments.

Before doing so, the reversibility of the reaction was tested in a single binding experiment (fig. 4.4). Immobilized P45/T50 was exposed to 7.6 nM KF until equilibrium was reached, and subsequently KF was entirely rinsed off within 2.5 hours. The association rate was found to depend strongly on the flow rate, which is a typical

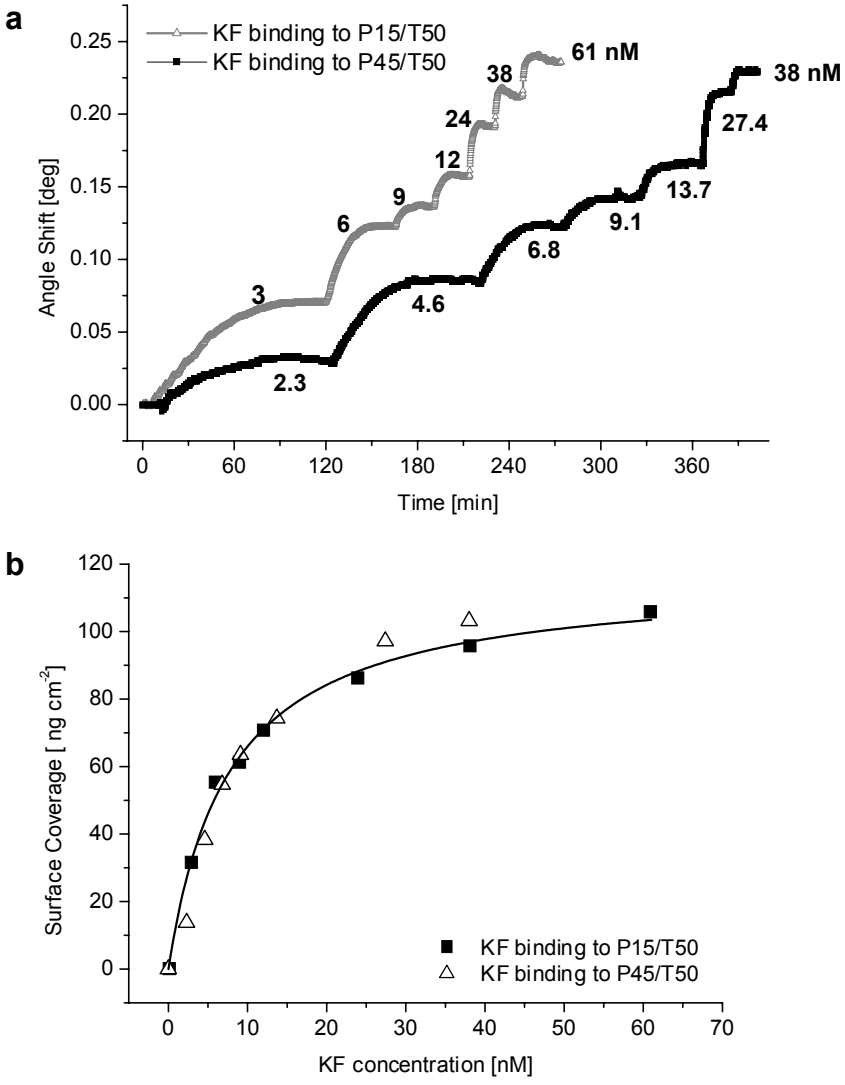

Figure 4.5: a) Titration curves for binding of KF to duplex P15/T50 (gray triangles) and P45/T50 (black squares). The KF concentration was gradually increased according to the steps designated in the plot. b) Langmuir isotherm. Plots of surface coverage versus KF concentration according to raw data shown in a. Both DNA substrates are equally favored by the KF. The black line corresponds to the Langmuir fit giving the affinity constant to $K_A=1.3\times10^8\ M^{-1}$.

indication for mass-transport limited reactions. Although, the KF was applied in a extremely low concentration in this experiment, rising the concentration did not eliminate the mass-control of the binding reaction. Therefore, it was impossible to describe the binding kinetics with a simple Langmuir 1:1 model. Alternatively, a mass-controlled bimolecular model, implemented in the software CLAMP 99 [Myszka, 1998], was able to represent the experimental data. In order to prevent the model from producing arbitrary solutions, a fixed dissociation rate, k_{off}=0.003 s^{-1}, was assumed as reported for similar systems [Matsuno, 2001]. Using this approach, an association rate of k_{on} =1.7×10^6 $M^{-1}s^{-1}$ and a rate for mass-transport, $k_{transport}$ =8×10^5 s^{-1}, was obtained.
In order to make the adsorption process as fast as possible, the experiments were performed at flow rates of 2 ml/min as KF binding could not be accelerated any further. Addition of KF prior to template hybridization did not cause a detectable signal, thereby proving the specificity of KF binding (data not shown).

Fig. 4.5a compares curves displaying the changes in resonance angle versus time obtained from titrating P15/T50 and P45/T50 with increasing concentrations of KF. The changes in reflectivity and angle shift, respectively, were converted into changes in thickness by fitting the scan curves monitored before KF binding and at full coverage. The resulting thicknesses were translated into surface concentration using eq. 2.19 (n_{KF}=1.45, dn/dc=0.212 ml/g). As it is clearly visible from the binding isotherms (fig. 4.5b), the used DNA substrates did neither differ in their binding capacities nor in their affinities. The measured data points were perfectly described by a Langmuir isotherm yielding the affinity constant to K_A=1.3×10^8 M^{-1}. This compares fairly well with the association and dissociation rates obtained from the single binding kinetics data (K_A=k_{on}/k_{off} =5.1×10^8 M^{-1}). The maximum surface load of 106 ng/cm^2 (1.7 pmol/cm^2) reveals that the coverage of streptavidin with DNA polymerase is low; only 46 % of the streptavidin molecules exhibit a binary polymerase/DNA complex. The element of uncertainty is the number of available DNA duplexes. If one trusts the SPR data for template hybridization, one has to assume that only 37 % of the biotin binding sites carry a DNA duplex, while 37 % of the primers remain single-stranded. This would explain the low coverage with KF. On the other hand, the low coverage could equally well be caused by steric hindrance.

4.4 Detection of nucleotide incorporation during DNA strand synthesis

Fig. 4.6 shows a typical result obtained from an enzymatic primer extension assay monitored by SPFS in the kinetic mode. The experiment exemplifies the way the majority of the DNA replication experiments have been carried out. The subchapters 4.4.1-4.4.4 are concerned with benefits and pitfalls of the method.

After the successful preparation of a streptavidin monolayer and the attachment of the DNA substrate P45/T50G1close (see E in fig. 4.2), a mixture of KF (7.6 nM) and Cy5-dCTP (1 µM) in HSM buffer was added with a constant flow rate of 2 ml/min. The increase in intensity of reflected light clearly demonstrates KF binding to DNA, while background fluorescence remains constant at ~1×10^5 cps. DNA extension does not take place at this stage because the first base of the template sequence required addition of a nucleotide different from dCTP. At high dNTP concentrations, KF has been reported to incorporate also incorrect nucleotides [Joyce, 1989], yet, much slower; this has not been observed in the present case at moderate dNTP concentrations. Consequently, this experiment shows that the absence of the correct nucleotide is effective in inhibiting DNA replication. At equilibrium, DNA extension was initiated by adding a mixture of KF (at a concentration identical to that used for prior immobilization) and all four

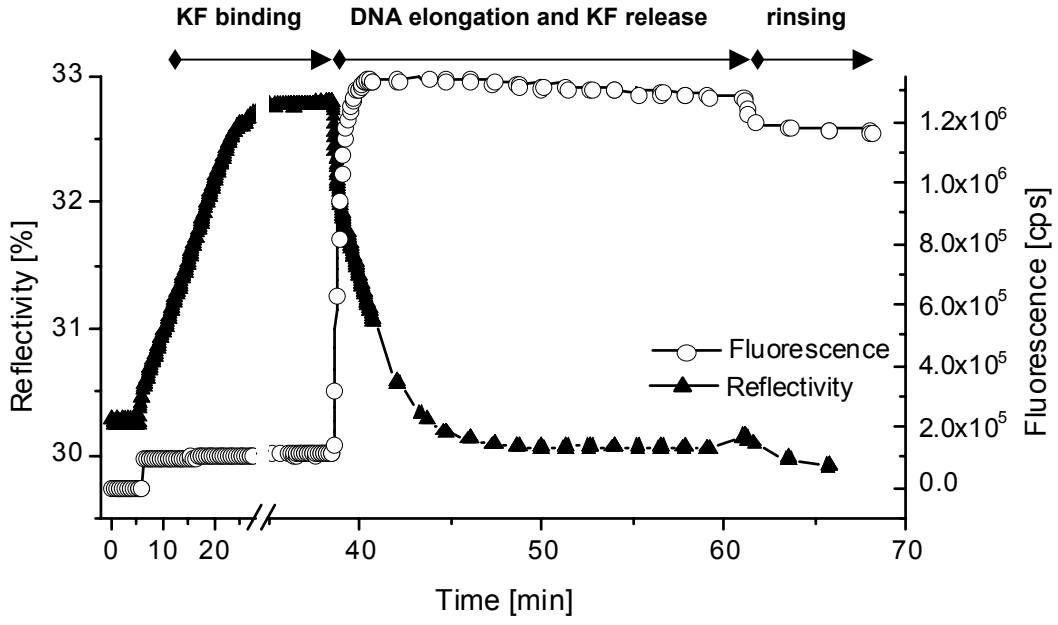

Figure 4.6: Example for a primer extension assay monitored by SPFS. Firstly, KF (7.6 nM) was added together with Cy5-dCTP (1 µM). DNA replication was not initiated in the absence of nucleotides being complementary to the first templating base. The reflectivity increase after KF injection is attributed to the formation of a binary DNA/KF complex (black triangles). Injection of the complete dNTP mixture (1 µM each) caused the release of KF and a rapid fluorescence increase (open circles) demonstrating incorporation of Cy5-labeled nucleotides into surface-attached DNA. The mass increase due to DNA synthesis was below the detection limit of SPR and did not show up in the reflectivity curve.

dNTPs (1 µM each, dCTP was fully substituted by the labeled analogue). The system responded with a nearly instantaneous jump in fluorescence intensity and a decrease in reflectivity. These opposite effects were attributed to DNA growth due to the incorporation of dNTPs including the Cy5-dCTP and the simultaneous release of the enzyme from the double-stranded DNA. Within a few minutes, the reflectivity signal returned to its initial values. As discussed in section 4.2, the incorporation of 35 nucleotides could hardly be detected by SPR. Therefore the changes in reflectivity can be solely attributed to changes in the surface concentration of KF. The SPR scan curves recorded before and after incorporation of Cy5-dCTP were identical, which rules out the possibility that the changes in reflectivity are caused by broadening of the plasmon curve. Those effects have been reported for the adsorption of large amounts of dye, if this turns a non-absorbing dielectric in an absorbing one. After enzyme release was finished, excess dNTPs were removed by rinsing with buffer. Upon rinsing the fluorescence intensity remains unaffected (besides small bleaching effects), indicating the covalent incorporation of Cy5-dCTP into the DNA. In a control experiment, different concentrations of Cy5-dCTP were exposed to the DNA in the absence of KF. The bare presence of the labeled compound caused a background fluorescence that increased linearly with the concentration and originates from molecules in the bulk staying within the range of the evanescent field. Since it can be quantitatively removed by rinsing, unspecific adsorption to the matrix can be excluded (fig. 4.10c).
In summary, the curve shown in fig. 4.6 has the potential to give information regarding the association of KF to different DNA substrates, the rate and yield of Cy5-dCTP incorporation and the release of KF from complete DNA duplexes.

4.4.1 Fluorescence yield

The fluorescence light produced in the course of the polymerization reaction shown in fig. 4.6 was collected with a 1.3 dB attenuator mounted in front of the photomultiplier. According to the template sequence one labeled nucleotide has been incorporated per DNA duplex in the optimal case of efficient replication. Fig. 4.7 shows the corresponding SPFS scan curves monitored before and after DNA elongation with and without attenuator. The resonance and the critical angle of the plasmon curves were identical. Also the depth of the plasmon curves remained unchanged, indicating that the DNA layer is still non-adsorbing (although chromophors have been introduced). As theoretically predicted, the peak of the fluorescence curve is slightly shifted to smaller resonance angles. The fact that the peak region of the fluorescence curve recorded without attenuator is broadened demonstrates that the saturation level of the photomultiplier was reached. The attenuation factor was experimentally determined to

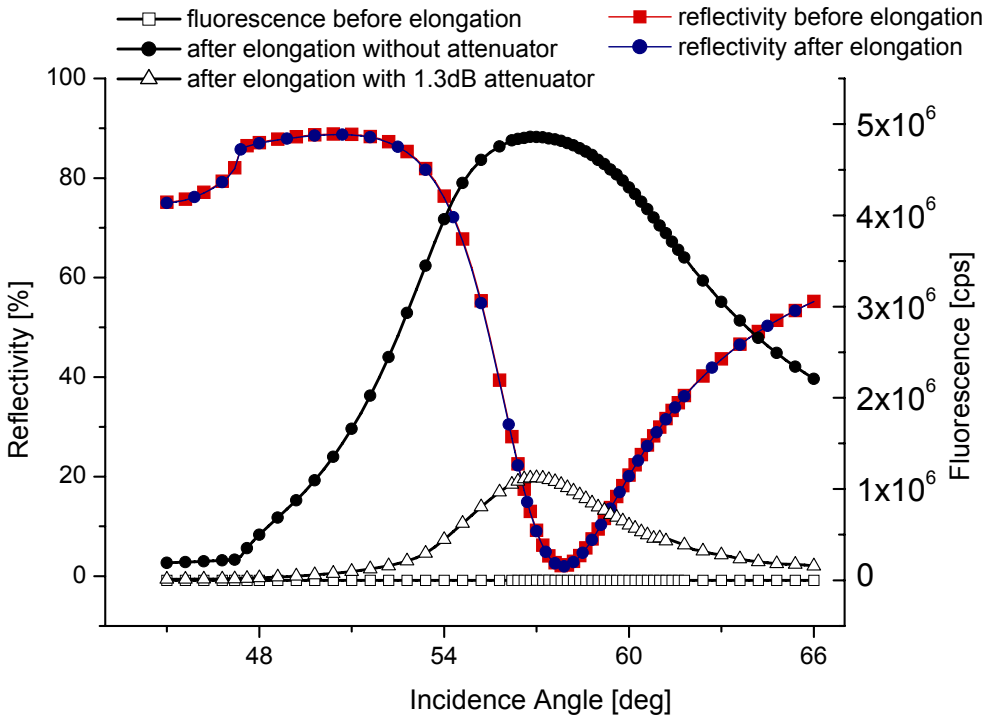

Figure 4.7: Fluorescence and reflectivity scan curves recorded before and after incorporation of Cy5-dCTP into surface-attached DNA. Fluorescence intensity was measured without (black circles) or with (gray triangles) 1.3 dB attenuator mounted in front of the photomultiplier. Note that the attenuation is smaller than expected (the attenuation factor was experimentally determined to be ~19). Thus, the photomultiplier goes into saturation without an attenuator. Data were obtained from the kinetic experiment shown in fig. 4.6.

be ~19 in five independent experiments yielding different surface concentrations of dye. In fig. 4.7 the signal was attenuated by a factor of 5 only, further supporting that the saturation level was exceeded. Accordingly, a linear relationship between fluorescence light and the label's surface concentration is not given anymore. If not mentioned explicitly otherwise, this problem was circumvented by using an 1.3 dB attenuator.

The detection limit can be estimated from the experiments discussed in detail in chapter 4.7 where elongation of P45/T50G1close was carried out at varying ratios of Cy5-dCTP : unlabeled dCTP. In the following, this ratio will be given as mole fraction x_{Label} = c(Cy5-dCTP) : c(dCTP+Cy5-dCTP). Utilizing a mole fraction x_{Label}=0.001 (1 nM Cy5-dCTP : 1µM dCTP) for the elongation reaction still resulted in ~8500 cps fluorescence yield (measured without attenuator, see fig. 4.8). Since the experiments have shown that incorporation of labeled dCTP increases linearly with the mole fraction, x_{Label} at least for $x_{Label} < 0.5$, one can assume that ~1/1000 of the surface-attached DNA strands had been labeled in the reaction. Thus, using SPFS enables to detect a label at least concentration of about 4.7 fmol/cm^2 (c. f. primer density in chapter 4.2), corresponding to 29 Cy5-molecules per µm^2.

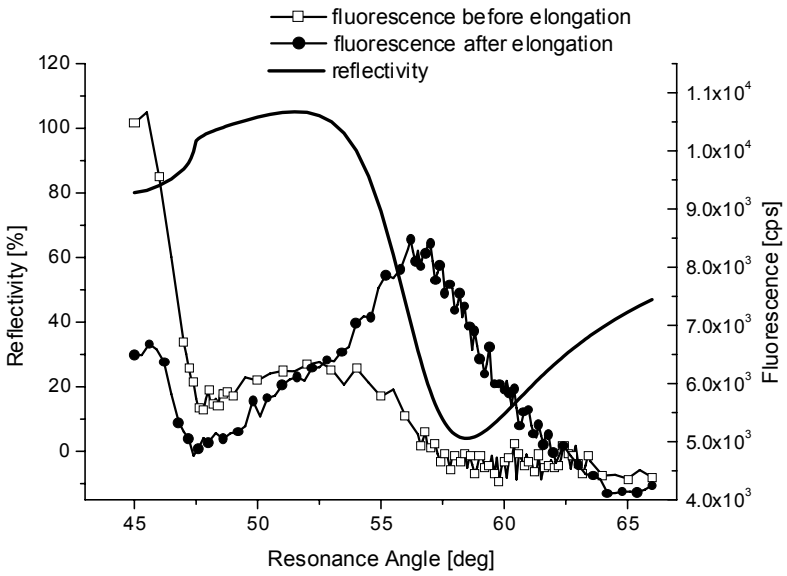

Figure 4.8: Evaluating the limits for fluorescence detection. Duplex P45/T50G1close has been elongated in the presence of 1 nM Cy5-labeled and 1 µM unlabeled dCTP.

4.4.2 Fluorescence quenching

As shown in the previous section, fluorescence detection using SPFS is extremely sensitive and even label concentrations down to ~4.7 fmol/cm^2 could be detected. This result was obtained from experiments utilizing an artificial template that exhibited a single guanine to be paired with cytosine. Yet, naturally occurring DNA has a GC content of about 50 %. Aiming at the application of the primer extension assays as method for DNA detection, the question arises whether the detection limit can be further improved by multi-labeling of the DNA strands. Fig. 4.9 depicts three extreme cases: First, ds-P45/T50 (containing 12 guanines) was extended in the presence of Cy5-dCTP at a molar fraction of x_{Label}=0.5 (curve 1). In the initial phase the fluorescence intensity raised substantially to 650.000 cps and dropped down to 150.000 cps if the reaction proceeded. Thus, the fluorescence was gradually quenched with the increasing label density. Curve 2 and 3 in the same plot correspond to extension of P45/T50G1close and P45/T50G1far (E and F in fig. 4.2), respectively, carried out at identical conditions. The duplex P45/T50G1close has a single guanine at the second and P45/T50G1far at the last position of the template sequence (seen from 3' to 5'). The fluorescence yield obtained for elongation of P45/T50G1close was ~5 times larger than for elongation of P45/T50G1far; however, one would intuitively expect a smaller yield for the former because the label should be closer to the gold surface than for the substrate P45/T50G1far provided the strand is oriented perpendicular to the surface. The theoretical quenching profile describing the distance dependence of radiation-less

energy transfer from the dye to the metal is shown in chapter 2.2.4. For distances between 7 and 20 nm, which is the region of interest for the present DNA architecture, the profile predicts a large fluorescence increase with increasing distance. Yet, due to the long 30-mer spacer, the DNA duplex is very likely to adopt a secondary structure that brings the 5'-terminus of the template closer to the surface than the position on the strand where Cy5 was incorporated in P45/T50G1close. Indeed, if one compares the total fluorescence yield achieved by hybridizing T35 to P45/5'-Cy5-T50 ($\rightarrow 9\times10^5$ cps) and by incorporating Cy5-CTP (x_{Label}=1) in P45/T50G1close ($\rightarrow 1.2\times10^6$ cps), the fluorescence emitted from the DNA construct being Cy5-labeled at the 5'-terminus of the template is lower, demonstrating a smaller separation distance. Of course, this reasoning holds only true if both processes (hybridization and incorporation of dye) occur with similar efficiencies, as it had been reported recently [Krieg, 2003].

Still, the signal for P45/T50G1far should be only 25 % lower and not 80 % like depicted in fig. 4.9. Therefore the missing fluorescence intensity can be attributed to incomplete DNA replication that stopped before adding the terminal 3'nucleotide.

It was beyond the scope of this work to examine in detail how many labels are incorporated opposite to a template strand with a natural GC content at certain mole fractions x_{Label}. The factors contributing to the fluorescence yield observed are too numerous to be assessed: Intramolecular quenching and quenching due to the proximity to the gold surface, both depending on the secondary structure; possibly termination of

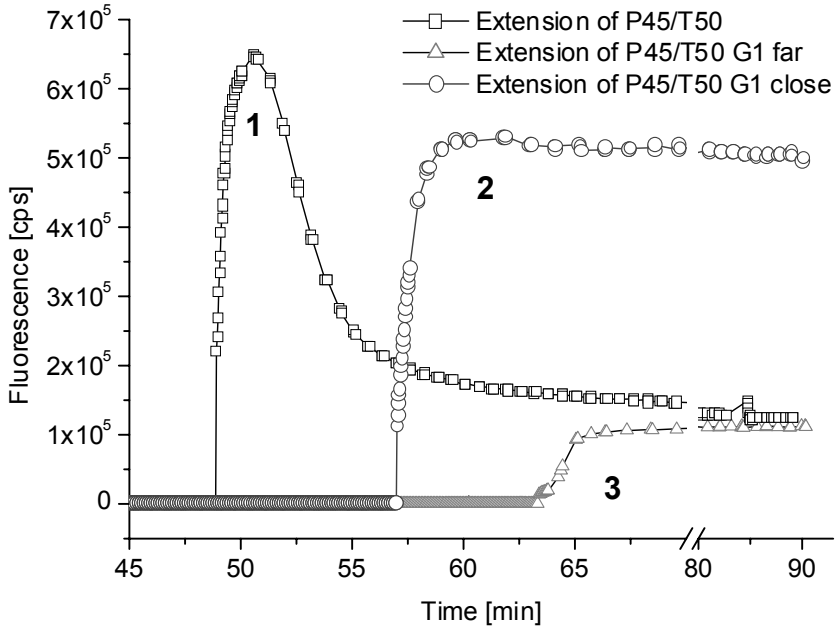

Figure 4.9: Fluorescence intensities yielded for the replication of three different templates that differ in number and position of guanine bases. Duplex P45/T50 contains 12 randomly distributed guanines (squares), whereas P45/T50G1close (circles) has a single guanine at the beginning and P45/T59G1far (triangles) at the 5'-end of the template strand.

the replication reaction and variation of the strength of the interfacial evanescent field in dependence on the position of the dye relative to the surface. Yet, it was experimentally found that extending P45/T50 at a mole fraction x_{Label}=0.1 yielded similar fluorescence intensities as extension of P45/T50G1close with x_{Label}=1. In both cases, in average one Cy5-molecule should be attached per DNA strand, excluding intramolecular quenching effects.

4.4.3 Experimental errors due to primer degradation

Some of the experiments discussed here, relied on the exact determination of the extremely rapid fluorescence increase after initiation of the polymerization reaction. Fig. 4.10c demonstrates that the bare presence of Cy5-dCTP in the absence of KF gave rise to a substantial background fluorescence that increased linearly with concentration. For instance, the presence of 1 µM Cy5-dCTP is attributed to a background value of 1×10^5 cps. If Cy5-dCTP was not added together with KF prior to the initiation of DNA replication, the fluorescence increase observed in the early stage after injection of all four dNTPs (including Cy5-dCTP) originates from background fluorescence caused by the presence of Cy5-dCTP in the bulk solution and from its incorporation into the DNA strands. If the Cy5-dCTP concentration was fixed for a set of experiments, every experiment was equally influenced by the background fluorescence which made the results comparable. In other cases, the measurements were carried out such that Cy5-dCTPs were added at the concentration of interest together with KF before injection of the dNTPs necessary to launch DNA replication. That way, background contributions were excluded from the signal.

However, the fluorescence increase observed after injection of KF together with Cy5-dCTP was often unreasonably high. To find an explanation one has to recall the primer sequence: it terminates by three cytosine, while the first templating base requires incorporation of adenine. In paragraph 4.4 it was stated that the absence of the required base is sufficient to inhibit the replication. If some of the 3'-bases of the primer were missing due to degradation, cytosine could be added there.

To check whether degradation of the primer terminus caused the high fluorescence increase, primer and template were pre-hybridized before immobilization and than incubated with KF and unlabeled dCTP ex situ (20 µl primed template (50 µM), 20 µl HSM buffer, 4 µl dCTP (0.5 mM), 0.2 µl KF (15.2 µM). After this treatment, DNA was immobilized as usual but in PBS buffer to disrupt KF binding. Fig. 4.10a shows the comparison of two primer extension assays performed under identical reaction conditions except for the fact that the DNA used in experiment 2 had been pre-incubated with unlabeled dCTP. The first fluorescence increase differs clearly by a

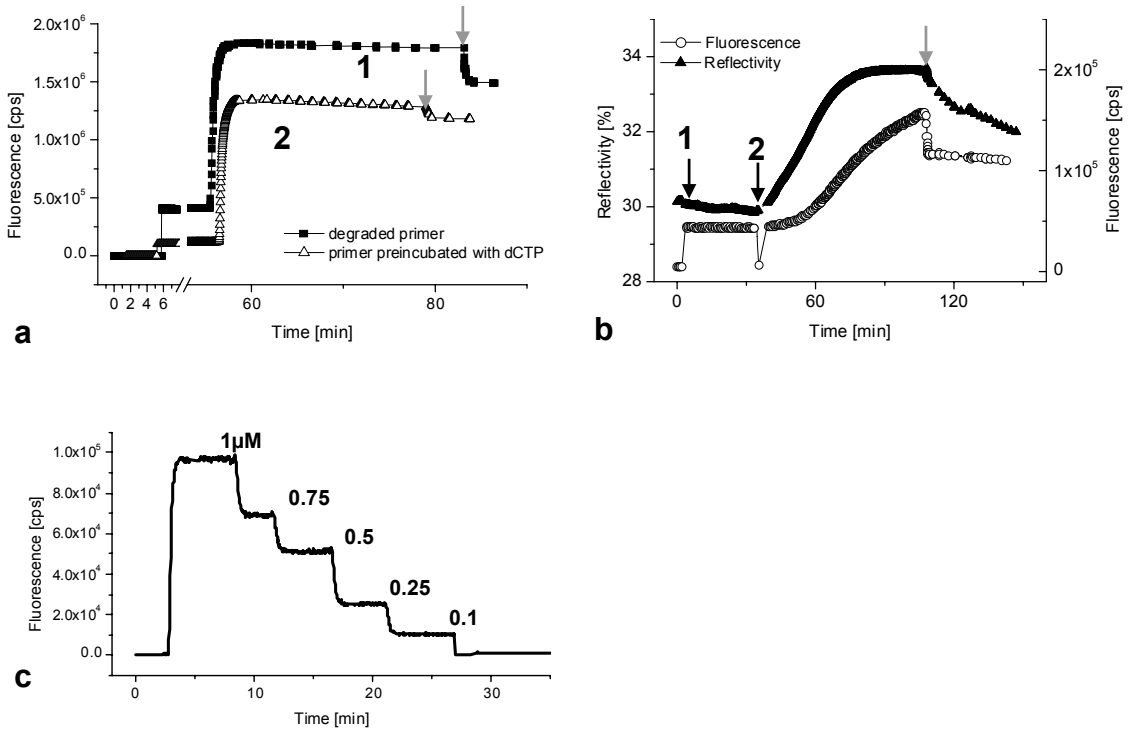

Figure 4.10 a: Fluorescence curves for the elongation of P45/T50G1 close with (2, open triangles) and without (1, black squares) pre-incubation of the primed template with KF and unlabeled dCTP. All dNTPs including Cy5-dCTP were applied at 1 µM concentration. Gray arrows indicate rinsing with buffer. b: Primer extension of P45/T50G1 close with Cy5-dCTP at extremely low concentration (25nM) slowing down the process. Point 1: Addition of Cy5-dCTP. Point 2: Addition of Cy5-dCTP+KF. c: Various Cy5-dCTP concentrations were exposed to surface immobilized DNA in the absence of KF in order to test for unspecific binding and bulk contributions to the fluorescence yield. Rinsing removed unincorporated nucleotides quantitatively.

factor of 4 (and is in good agreement with the experimental background curve in fig. 4.10c), demonstrating the effectiveness of this procedure to eliminate the consequences of primer degradation. In fig. 4.10b an extremely low Cy5-dCTP concentration was applied together with KF in order to slow down the incorporation reaction and to visualize what was seen as a jump in the reactions in a. As equilibrium for KF binding was adjusted, non-covalently linked dNTPs were rinsed off with buffer, proving that Cy5 incorporation had occurred.

These results show that even if the oligonucleotides are handled with care, damage of their sequence occurs, which in turn provokes deviations of their hybridization kinetics from a simple bimolecular model by introducing surface heterogeneities.

4.4.4 Efficiency of DNA replication

In the present studies synthesis of DNA was visualized by incorporation of fluorescently labeled nucleotides into DNA. Using this method, only the presence of labels placed at a few designated positions of the DNA sequence can be directly observed. Since the intensities of the reflected light before and after DNA elongation were found to be identical, one cannot make use of the SPR signal in order to quantify the amount of synthesized DNA. According to the SPR signal obtained for hybridization of T35 (see chapter 4.2), complete DNA replication should result in an reflectivity shift of ~1 %. Since this shift was never detected for the incorporation a mixture of labeled and unlabeled dNTPs, one might suspect that DNA replication is terminated before the completion of the primer strand.

One possibility to use fluorescence as indicator for the completeness of DNA replication is to attach a single label at the very end of the surface-attached DNA strand in the course of the replication process (at or opposite to the 5'-terminus of the template). Here, the difficulty is to predict the fluorescence yield expected for 100 % replication. Depending on the chromophore's distance to the surface, fluorescence intensity can be lost due to radiation-less transfer of energy to the gold surface (primarily at distances smaller than 20 nm). Since the exact separation distance between dye and surface depends on the unknown secondary structure of the immobilized DNA duplex, it is not possible to predict theoretically the fluorescence yield expected for 100 % labeling at a certain position. Therefore one has to find a way to measure experimentally the fluorescence yield expected for complete replication of the template.

Here, this was attempted by monitoring the changes in fluorescence of duplex P45/5'-Cy5-T50 (G in fig. 4.2) during hybridization of T35. This reaction produces a complete double strand being singly labeled at the 5'-terminus of the template. Fig. 4.11a shows SPR and fluorescence kinetic curves corresponding to binding of biotinylated P45 (1 µM) to the streptavidin matrix and the subsequent hybridization to an excess of 5'-Cy5-T50. The fluorescence signal raised to 7×10^5 cps upon capture of the template, which is referred to as 100 % fluorescence in the graph. Hybridization of T35 caused a further fluorescence increase of ~29 %. During hybridization, the coiled dangling 5'terminus of T50 stretches out while adopting an ordered helix structure, thereby, the distance of the chromophor relative to the surface was increased which reduced quenching effects. In an equivalent experiment, replication of duplex P45/5'-Cy5-T50 in the presence of 7.6 nM KF and 100 µM unlabeled dNTPs was employed to create a double strand (fig. 4.11b).

In this case, the fluorescence increase was only 7 %, whereas the SPR signal was almost identical to the experiment above. Continuing with hybridization of T35 produced a further fluorescence increase of 12 % accompanied by a small increase in reflectivity. Thus, there were still hybridization sites for T35 left, proving that DNA replication was

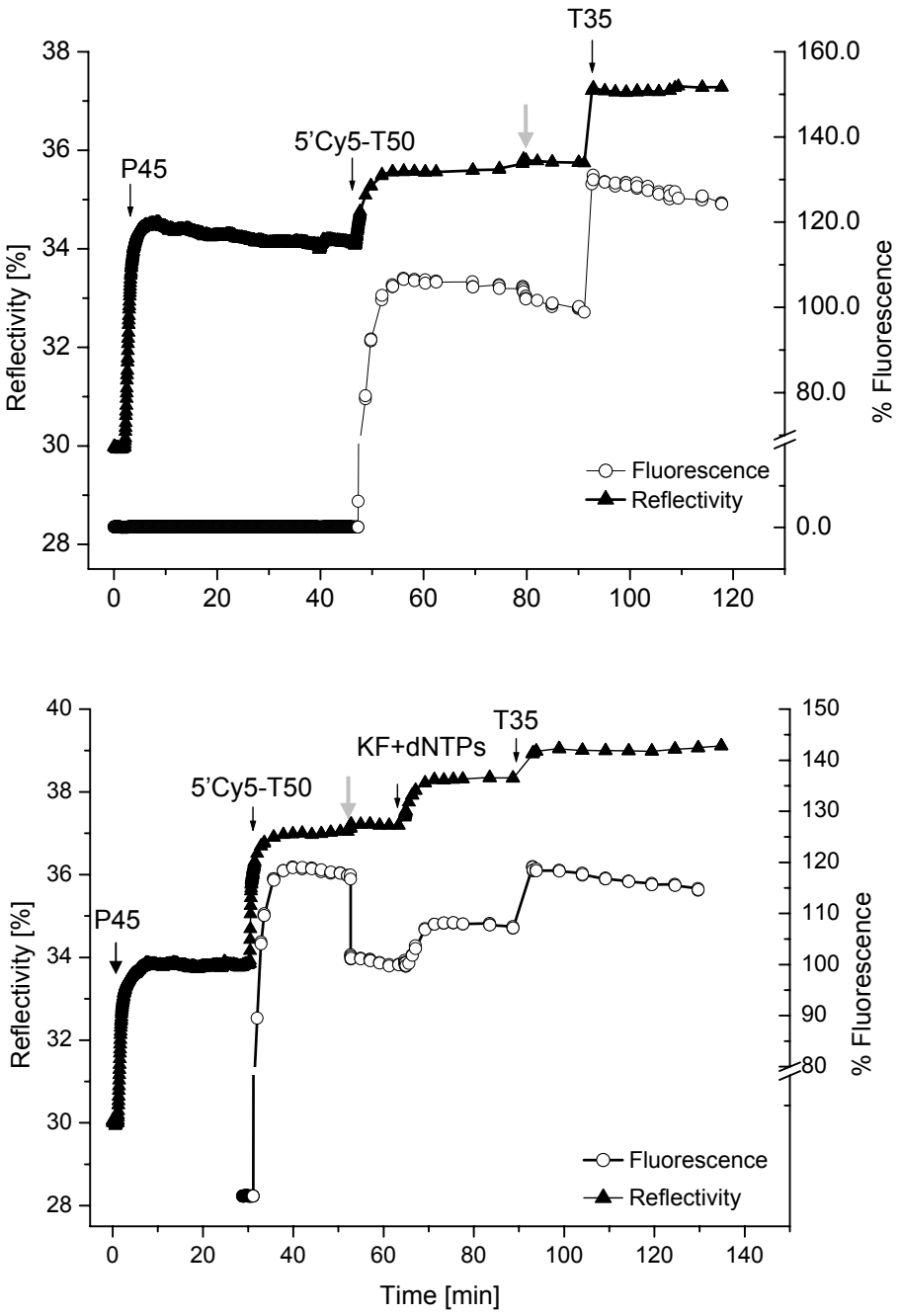

Figure 4.11: a) SPFS experiment showing immobilization of P45 and the subsequent hybridization of 5'Cy5-labeled T50. Hybridization of unlabeled T35 caused a further increase in fluorescence that originates from changes in the separation distance between dye and metal surface. b: Addition of KF (7.6 nM) together with unlabeled dNTPs (100 µM) caused a first, hybridization of unlabeled T35 a second increase in fluorescence.

not perfectly complete. However, hybridization of T35 does not necessarily require the existence of the whole single-stranded part of the template (35-mer). Also prematurely terminated replication products, having shorter overhanging strands, would be sufficient to create stable duplexes upon hybridization with T35 as long as their length exceeds ~12 nt. Shorter overhangs that remain unpaired would diminish the fluorescence yield, which explains why the overall yield upon stretching differed by 10 % in the two experiments described.

In experiment b, only ~50 % of the overall fluorescence increase (caused by replication plus subsequent T35 binding) originated from duplex formation due to DNA replication. Consequently ~50% of the DNA duplexes were not replicated to the terminal base. This is also in good agreement with the experiment discussed in paragraph 4.4.2, in which the extension of P45/T50G1far resulted in a fluorescence intensity being ~80 % smaller than that obtained for P45/T50G1close under identical conditions. In an afford to explain this difference, 25 % of the intensity were attributed to a loss due to quenching at the metal surface, the loss of the remaining 50 % were probably also caused by an incomplete polymerization reaction.

4.5 Effect of DNA Polymerase concentration

In order to ensure that it is the enzyme bound to surface-attached DNA that is actually active in DNA polymerization, DNA extension assays were performed utilizing different KF surface coverages. Identical surfaces were prepared by immobilization of pre-hybridized P45/T50 (1 µM solution) on top of the streptavidin layer. DNA immobilization was followed using SPR and found to result in identical shifts of the resonance angles. KF at solution concentrations ranging between 1.5 nM and 30 nM was bound to the DNA substrate and primer extension initiated by addition of a 10 µM solution of dNTP. The ratio between Cy5-labeled and unmodified dCTP was 1 : 40, which reduced the label density in the synthesized DNA strand in order to avoid intramolecular quenching effects. After the KF binding reached its equilibrium state, a scan curve was taken prior to DNA polymerization to be able to calculate the amount of bound enzyme precisely. For a clearer presentation, SPR and fluorescence curves for primer elongation carried out using different KF concentrations are shown in separate figures (fig. 4.12a and b, respectively).

The DNA synthesis started instantaneously after dNTP addition (note that time of injection is set to zero in fig. 4.12b and the curves are slightly shifted relative to each other); final fluorescence values were reached within one minute. Due to the velocity of the reaction, dNTP injection was carried out without closing the shutter of the photomultiplier in the darkness to exclude ambient light. Fig. 4.12a demonstrates that the amount of immobilized KF rose with increasing solution concentrations according to the corresponding Langmuir isotherm (see chapter 4.3). Solution concentrations of 1.5, 3, 7.6, 15 and 30 nM, respectively, resulted in surface coverages of 19, 33, 80, 92 and 108 ng/cm^2, as calculated from SPR scan curves (n_{KF}=1.45).

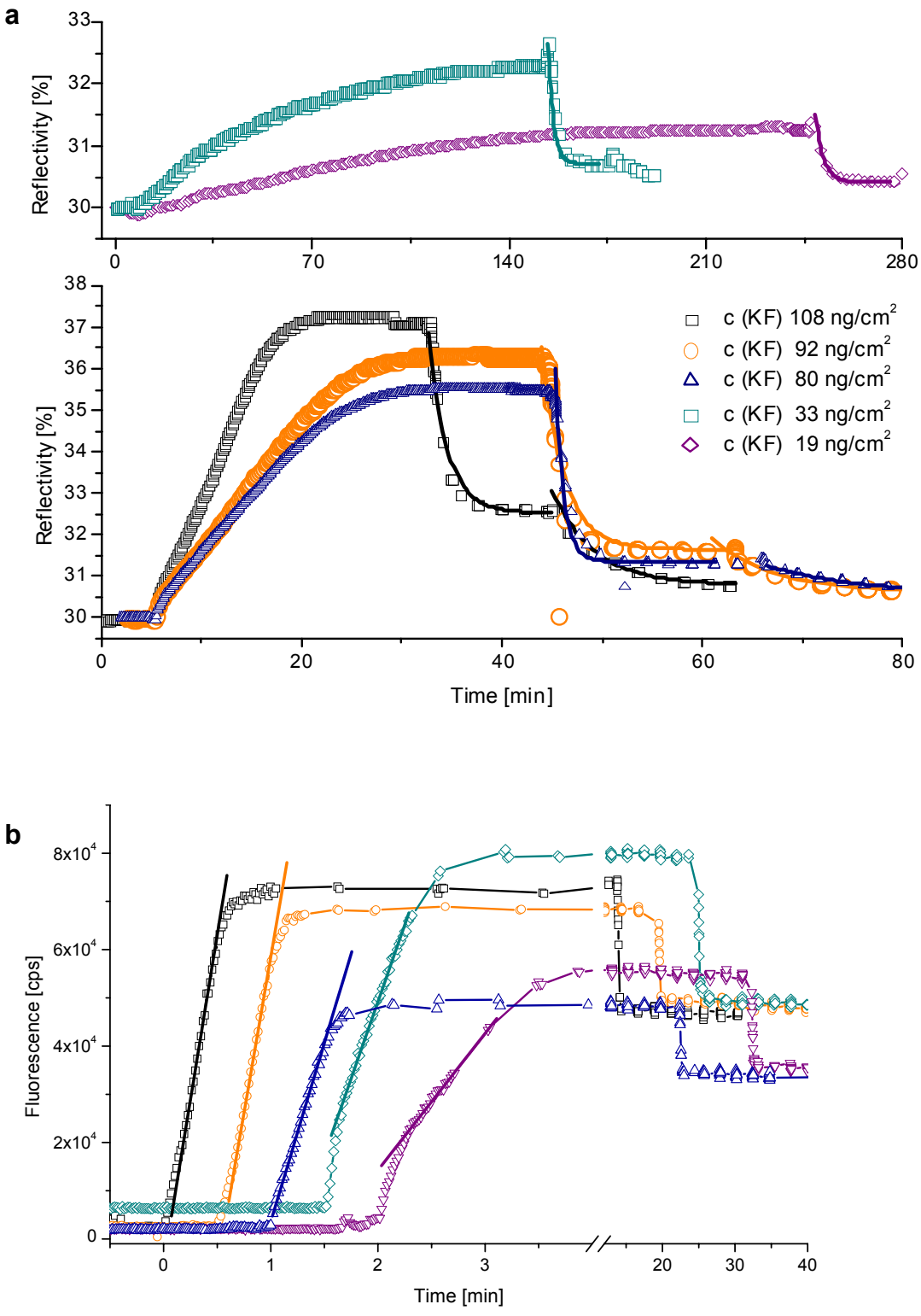

Figure 4.12: Influence of KF concentration on KF binding, velocity of DNA replication and KF release. Bulk concentrations of KF were varied between 1.5 nM and 30nM, while the dNTP concentration was fixed at 10 µM (ratio labeled dCTP:unlabeled=1/40). a) Time evolution of the reflectivity. Due to different time courses, curves corresponding to very low KF concentrations are shown in a separate panel (top). Single exponential fits describing enzyme release are shown as solid lines in the respective color. b) Fluorescence curves monitored in parallel to the reflectivity curves shown above. The time of dNTP injection is offset to zero and the curves are shifted relative to each other for a clearer presentation. Linear regressions of the initial slopes are given as straight lines.

The lower the KF concentration applied, the slower the adsorption process. Injection of dNTP solution caused a rapid increase of the fluorescence accompanied by a decrease in reflectivity. Whereas the initial slopes of the fluorescence curves became steeper with increasing KF concentrations, the single exponential decay of the SPR signal did occur with similar rates irrespective of the KF concentration. The averaged rate was $k_{off} = (9 \pm 3) \times 10^{-3}\ s^{-1}$ (fig. 4.13b).

This result is in agreement with the Langmuir picture, in which the dissociation rate does not depend on the surface coverage if the bulk concentration of the analyte is zero. Although, the KF was not removed from solution, this fact indicates that rebinding of the enzyme to double strands does not play a major role under these conditions.

For experiments performed at KF concentrations higher than 33 ng/cm^2, a second single exponential decay was observed upon buffer rinsing. In contrast to the decay rates in the presence of bulk KF, these rates depend linearly on the KF concentration. Rates of 1.9×10^{-3}, 2.8×10^{-3} and $4 \times 10^{-3}\ s^{-1}$ were found at 80, 92 and 108 ng/cm^2 surface coverage, respectively. This effect might be reasoned by some unspecific binding to the matrix at high KF concentrations. Occupation of the 3'phosphorylated terminus by KF molecules was largely excluded by the titration experiments discussed in section 4.3.

As plotted in graph 4.13a the initial slopes of the fluorescence curves increased linearly with increasing KF surface coverage. The final fluorescence achieved was about 50.000 cps in all sets of experiments, except for KF surface coverages of 19 and 80 ng/cm^2. In both cases the final value was 35.000 cps. This deviation was considered to be within the experimental error because there was no trend visible. The way the elongation process was accelerated with increasing amounts of KF bound to DNA, clearly demonstrates that bound KF is the catalytically active species. This means the enzyme is not deactivated in the proximity to the surface, which underlines the

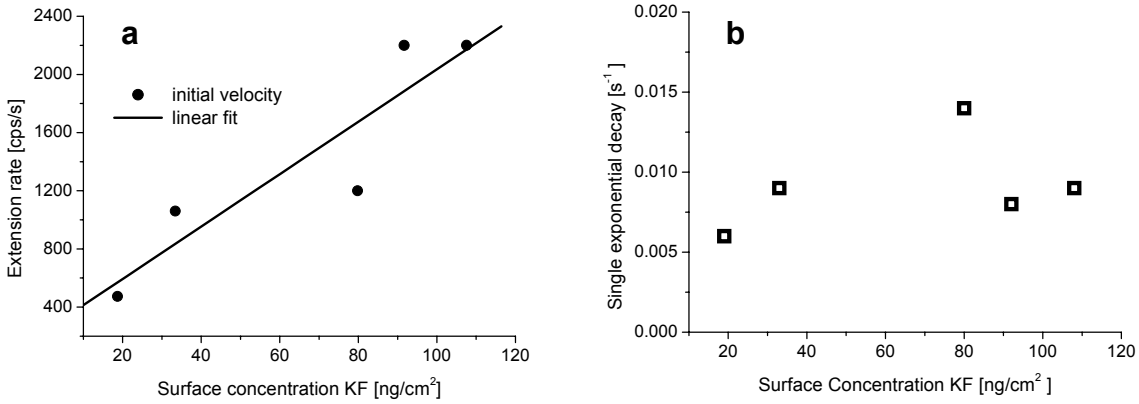

Figure 4.13: Plot of fluorescence slopes caused by incorporation of labeled nucleotides versus KF surface concentration (a). The extension rate increased linearly with KF surface concentration. In contrast, the single exponential decay of the SPR signal does not correlate with the KF concentration (b).

suitability of the surface architecture for the polymerization reaction.

In a comparable set of experiments, KF and dNTPs were added in one step without prior binding of KF to the DNA. Although the experimental conditions were not identical, insofar as the total dNTP concentration was 0.5 µM and the ratio between Cy5-labeled and unmodified dCTP was adjusted to 1 : 10, the experiment nicely demonstrates that the binding of the enzyme was the rate-limiting step under these conditions. DNA polymerization did not start immediately after injection but with a time delay of up to 20 minutes for the lowest KF concentration resulting in fluorescence curves of a sigmoid shape (fig. 4.14). Plotting the slopes of their linear regions versus the KF bulk concentration, resulted in a hyperbolic curve well described by a Langmuir isotherm with a $K_A = 3 \times 10^8\ M^{-1}$, which perfectly compares with the affinity constant found for KF binding to P45/T50.

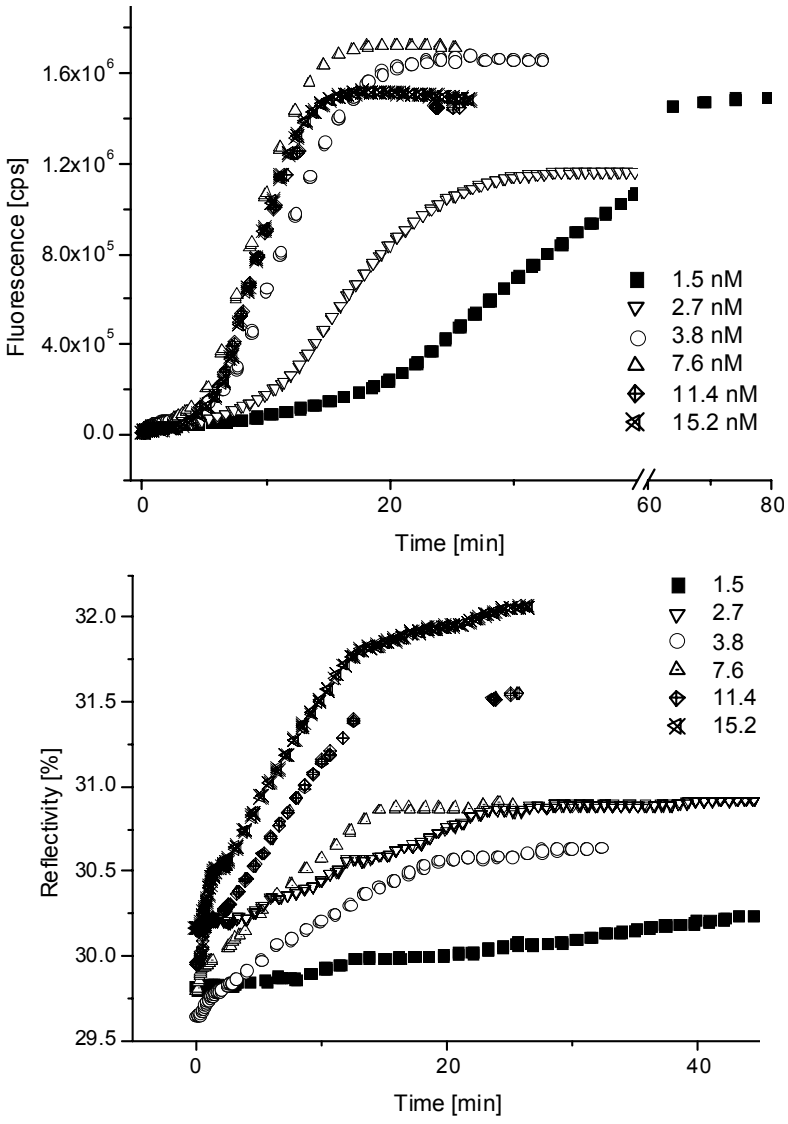

Figure 4.14 Elongation of DNA using varying KF concentrations without binding of the enzyme prior to initiation of the polymerization reaction. Top: Fluorescence data. Bottom: Reflectivity data. Under these conditions, KF binding became the rate-limiting step.

Note that almost no enzyme mass was accumulated at the surface under these conditions, demonstrating the short dwell times of the enzyme on the DNA substrates during the catalytic process. A mass signal appears only at high KF concentrations, which is in good agreement with the reflectivity data shown in fig. 4.12, where KF is not entirely released at high concentrations.

4.6 Effect of dNTP substrate concentration

The Michaelis Menten approach is a simple kinetic model suited for the description of the enzymatic DNA extension process. Herein, the immobilized KF/DNA complex is considered as the catalytically active species and the dNTPs as the substrates, which become covalently linked to the nascent DNA strand in the course of the reaction.

$$\left(\mathrm{KF/DNA_n}\right)_{\mathrm{im.}} + \mathrm{dNTP} \underset{k_{-1}}{\overset{k_1}{\rightleftarrows}} \left(\mathrm{KF/DNA_n/dNTP}\right)_{\mathrm{im.}} \xrightarrow{k_{cat}} \left(\mathrm{KF/DNA_{n+1}}\right)_{\mathrm{im.}} + \mathrm{P_2O_7^{-4}}$$

where n denotes the number of nucleotides in the DNA strand. The initial velocity of nucleotide incorporation, V_i, depends on the substrate concentration as follows:

$$V_i = \frac{k_{cat}[\mathrm{KF/DNA_n}]_0[\mathrm{dNTP}]}{K_M + [\mathrm{dNTP}]} \qquad \text{Eq. 4.1}$$

with

$$K_M = \frac{k_{cat} + k_{-1}}{k_1}$$

The Michaelis Menten constant, K_M, is a measure for the stability of the ternary KF/DNA_n/dNTP complex. The common method to determine the catalytic constants according to this model, is to vary the dNTP concentration over at least two orders of magnitude. In the Michaelis Menten picture, plotting the initial rates of nucleotide incorporation versus the substrate concentration results in a hyperbolic curve, with the maximum rate corresponding to the reaction velocity achieved at saturation of the enzyme with substrate. In such a plot, the Michaelis Menten constant, K_M, denotes the substrate concentration at which the reaction velocity is at its half maximum. Using the QCM-D technique, the dependence of the DNA extension rates on substrate concentration was studied between 1 and 200 µM dNTP and found to be in good agreement with the described model. The hyperbolic shape of the curve was well reproduced. Since the use of QCM in liquids entails the difficulty to quantify the amount of synthesized DNA and a clear separation of the signals caused by enzyme and

DNA mass could be only achieved by lowering the enzyme concentration, SPFS was applied as a complementary method. SPFS is superior to QCM-D with respect to separation of enzyme and DNA response, in that the "heavy" enzyme influences the SPR signal only, while the incorporation of Cy5-dCTP is sensitively monitored as fluorescence increase. Nevertheless, the maximum Cy5-dCTP concentration that can be applied is limited by two factors: Firstly, background fluorescence caused by bulk molecules excited within the evanescent field at the interface. In principle dilution of Cy5-dCTP with unmodified dCTP and using Cy5-dCTP only as an indicator would be effective in reducing the background fluorescence, if KF would not strongly prefer its natural substrate (see chapter 4.7). Experiments have shown that the mole fraction of labeled dCTP should not be smaller than 0.5 in order to ensure sufficient incorporation of dye-labeled nucleotides.

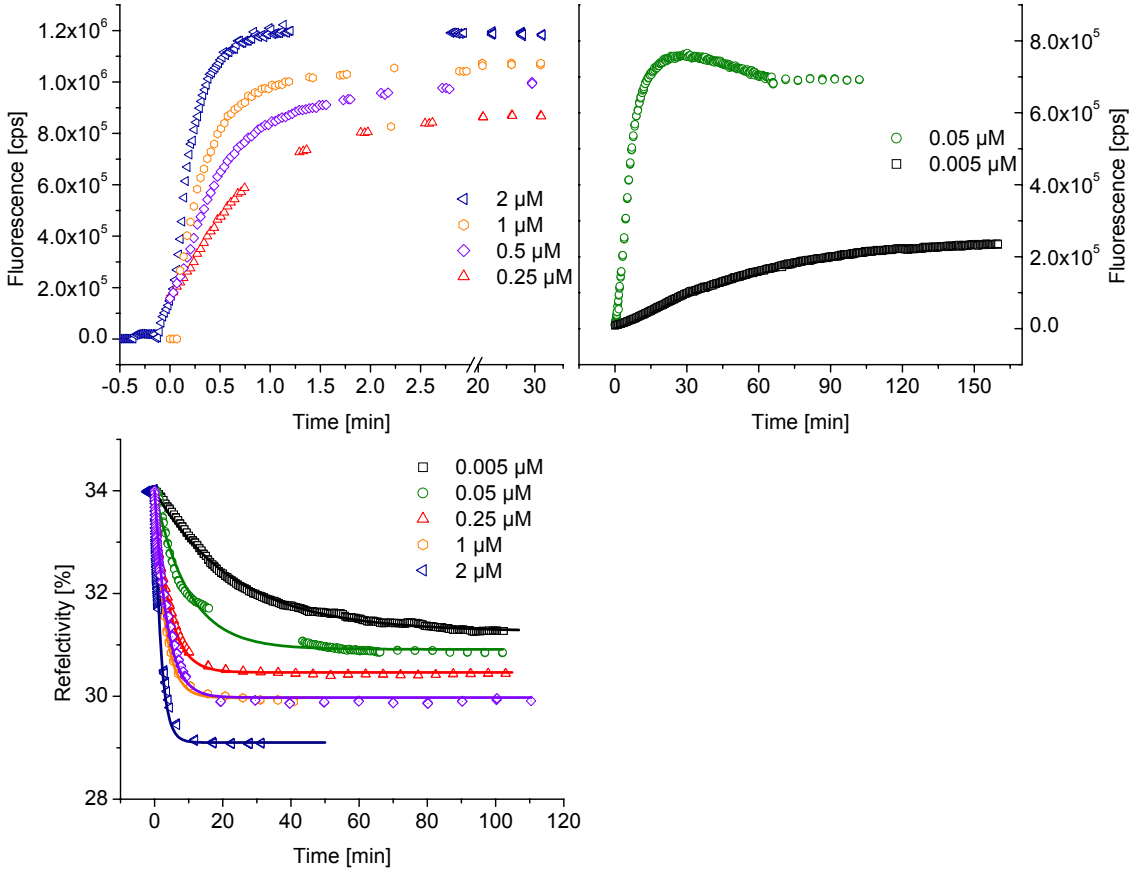

Figure 4.15: Replication rates as a function of total dNTP concentration. x_{Label} was 0.5 and identical surface concentration of KF were applied (80 ng/cm^2). Top: The fluorescence slopes were proportional to the dNTP substrate concentration. Bottom: Time courses of the reflectivity corresponding to enzyme release after DNA replication. The enzyme release is also influenced by the substrate concentration.

In the present set of experiments immobilized ds-P45/T50G1close (E in fig. 4.2) was used as template for DNA replication employing a fixed KF concentration of 7.6 nM. The template contained a unique guanine at the second position of the single-stranded region to pair with cytosine. Using this substrate the reaction observed was limited to a single incorporation event at the beginning of the polymerization reaction. Making a compromise between the above mentioned limiting factors, experiments were performed using total dNTP concentrations between 5 and 2000 nM at a mole fraction of x_{Label}=0.5.

In all experiments the KF immobilization caused a uniform reflectivity shift of ~ 4 %; this step is not presented here. Fig. 4.15 summarizes the SPR and fluorescence curves, respectively, obtained after exposure to different dNTP solutions (ranging from 50-2000 nM dNTPs) starting at the time of dNTP addition. The decay of the SPR signal and the increase of the fluorescence occurred in parallel in every experiment. Reducing the dNTP concentration had the following effects: The final values of fluorescence were decreased indicating a reduced number of incorporated Cy5-dNTP molecules. The decreasing fluorescence slopes correspond to a slowdown of the polymerization reaction, which is also reflected in lower time constants for the single exponential decrease of the SPR signal. While the SPR signal returned to the baseline in the presence of high dNTP concentrations, the reflectivity decrease was smaller at lower concentrations. This result might indicate an increasing amount of KF that remains bound due to incomplete DNA replication leaving recessed 3'-termini. Fig. 4.16 shows plots of the fluorescence slopes and the decay constants versus the dNTP concentration. Since it was known from QCM experiments (chapter 5.4.2.4) that the polymerization reaction obeys the Michaelis Menten model, data were evaluated on the basis of the

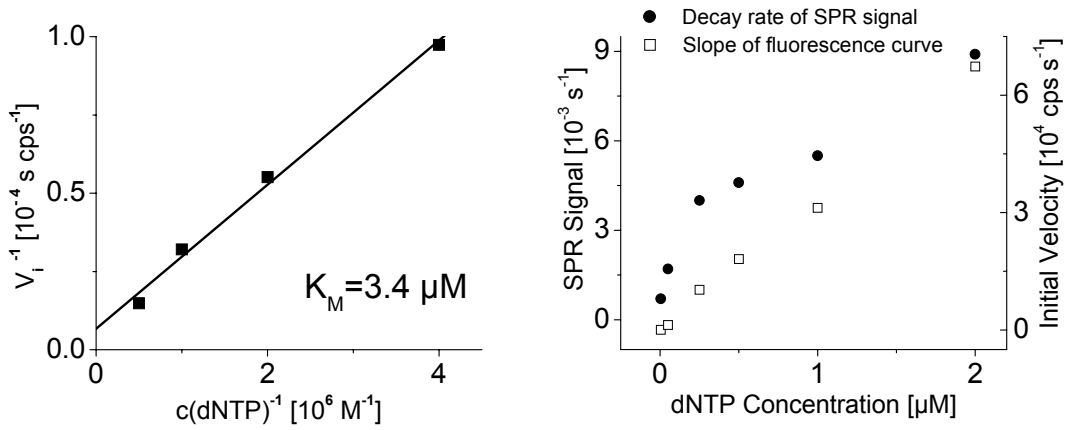

Figure 4.16: Lineweaver-Burk plot for the incorporation of labeled nucleotides (left). The data correspond to the experiments presented in fig. 4.15. Decay rates of SPR curves are presented together with the fluorescence slopes on the right side. Omitting the results obtained for 5 and 50 nM dNTP, the Michaelis Menten constant was calculated to be K_M=3.4 µM from the Lineweaver-Burk representation.

Michaelis Menten model. K_M was calculated from the linear Lineweaver Burk presentation, plotting V_i^{-1} versus $c(dNTP)^{-1}$. For the low dNTP concentrations employed, plotting of V_i versus c(dNTP) also results in a linear curve. The values corresponding to 5 and 50 nM dNTPs were omitted because a pre-requisite for using the Michalis Menten kinetics is the excess of substrate over the enzyme concentration, which is not fulfilled in these cases. K_M was found to be 3.4 µM, which compares well with results obtained from QCM-D (c.f. 3 µM) and literature values (c.f. 5 µM).

In contrast to the fluorescence slopes, the decay rates of the reflectivity did not increase linearly with the dNTP concentration. Ignoring the data point collected at c(dNTP)= 2 µM, the plot of the decay rate versus c(dNTP) rather resembles a hyperbolic curve. Upon interpreting this difference between the fluorescence and the reflectivity signal, one should consider the processes that these measurements account for. While the fluorescence increase is the consequence of a single KF/DNA encounter, the reflectivity refers to the replication of the whole template strand that is the result of frequent dissociation and rebinding events. In solution, the processivity of KF was found to vary between 10 and 100 bases. Using P45/T50G1close as a DNA substrate implies that the dye-incorporation takes place before KF dissociates the first time from the template strand. Therefore the fluorescence signal created here does not depend on the binding step. The fact that the decay rates of the reflectivity adopted a hyperbolic shape probably indicates that the KF binding is the rate-limiting step in the replication process (see fig. 4.14).

4.7 Effect of Cy5-dCTP concentration on label efficiency

The modification of nucleic acids using nucleotides linked to fluorophors is a common experimental tool in modern molecular biology. For instance the Sanger method for DNA sequencing, real-time PCR reactions or single molecule exonucleolytic sequencing strongly depend on the enzymatic incorporation of labeled nucleotides into DNA. Since DNA polymerases, the enzymes commonly utilized in these reactions, have a high specificity for their natural substrates, chemical strategies for the modification of nucleotides aim at optimizing their acceptance by DNA polymerases. On the mechanistic level, similar factors might be relevant as for the selection of the correct nucleotide being complementary to the templating base. Ignoring the proofreading activity of some polymerases, discrimination of nucleotides occurs at three stages of the reaction cycle: First, DNA polymerases bind correct dNTPs with about 10-1.000 fold higher affinity than they bind incorrect dNTPs. In a second rate-limiting step, binding of the correct dNTP induces conformational changes, which are a pre-requisite for phosphodiester bond formation. This transition can be more than 10.000 times slower

for incorrect dNTPs. And third, the rate of chemical bond formation is extremely slowed down in the presence of the incorrect dNTP [Kunkel and Bebenek, 2000]. Relevant for the identification of correct nucleotides are not the free energy differences resulting from H-bonding between AT and GC base pairs, since the differences between mismatched and matched base pairs in aqueous solution are too small [Loeb and Kunkel, 1982]. Although it was further suggested that exclusion of water from the active site may amplify the free energy differences between correct and incorrect base pairs [Petruska, 1986], this criterion is not sufficient to ensure high replication fidelity. More likely, the selectivity depends primarily on the base pair geometry [Goodman, 1997]. The geometry of the binding pocket formed during the rate-limiting step is such that non-Watson-Crick base pairs would not fit in. While attachment of a dye to a dNTP does not interfere with Watson-Crick base pairing, it changes the geometry of the labeled base pair, even if long alkyl chains are used as linkers between dye and dNTP. Rigler and coworkers tested the versatility of several labeled nucleotide analogues for low density labeling of natural DNA in PCR reactions using Taq polymerase [Földes-Papp, 2001]. The covalent incorporation of dye-dNTP decreased in the following order: rhodamine-green-5-dUTP, tetramethylrhodamine-4-dUTP, and Cy5-dCTP. For Cy5-dCTP, the number of chain termination products was significantly higher. The absolute number of rhodamine-green-5-dUTP molecules incorporated into a 217 bp PCR product was determined by exonucleolytic sequencing and analysis of the degradation product using two-color fluorescence correlation spectroscopy. For labeling at a molar ratio of x_{Label}=0.18, 17 green labels were found. Unfortunately comparable data are not available for Cy5-dCTP. Kinjo et al. found a linear relationship between Fluorescein-dUTP concentration and fluorescence intensity (the reaction mixture contained up to 50 % labeled dUTP) for labeling of a 4000 bp fragment [Kinjo, 1997]. The linear relationship proves that the label did not interfere with polymerase activity so that the incorporation can be considered as a statistic process.

However, in this chapter we describe the influence of various mole fractions of Cy5-dCTP (x_{Label}= c(Cy5-dCTP) : c(dCTP+Cy5-dCTP)) on the yield of incorporated labels in surface immobilized DNA. A template containing only a single guanine base (duplex P45/T50G1close, E in fig. 4.2) was elongated in the presence of dNTPs at a fixed total concentration of 1 µM and mole fractions x_{Label}=1, 0.9, 0.75, 0.5 and 0.25, respectively, using the KF (7.6 nM). The K_D for dNTP binding to a binary KF/DNA complex was previously determined to be 5 µM [Kuchta, 1987], which means that the elongation reactions were carried out below half saturation, which is not common for PCR reactions and might explain discrepancies in the results. Because we cannot estimate the total amount of synthesized DNA from the SPR signal, it was advantageous to incorporate only a single label to avoid quenching effects and the possibility that the data were influenced by the termination of DNA synthesis due to high label densities.

Referring to fluorescence intensities only, it would not be possible to differentiate between chain termination and a low label density. Fig. 4.17a shows SPFS scan curves obtained for a set of primer extension assays carried out at different mole fractions of Cy5-dCTP.

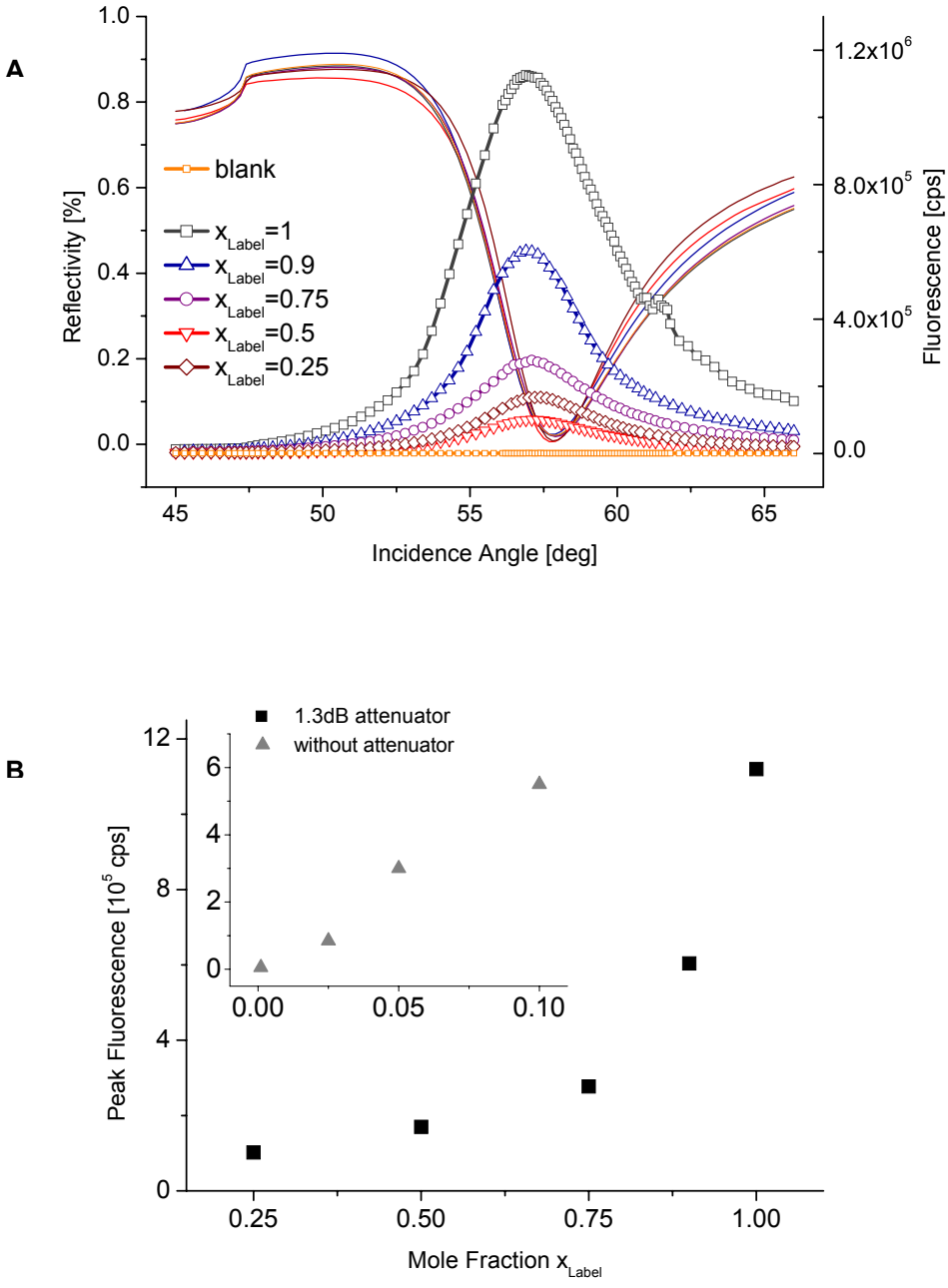

Figure 4.17: SPFS scan curves recorded before (orange) and after elongation of P45/T50G1close using different mole fractions of Cy5-dCTP, x_{Label} (a). The total dNTP concentration was 1 µM and KF was bound to DNA from a 7.6 nM solution prior to dNTP addition. Reflectivity curves are shown as solid lines, fluorescence curves as scatter in identical colors. b: Plot of final fluorescence values versus x_{Label} according to the raw data shown on top. Surprisingly, the plot is not linear, which means that Cy5-dCTP incorporation is not a statistic process. The inset displays results obtained from experiments performed at $x_{Label} \leq 0.1$; here data were acquired without using an attenuator (gray triangles).

The SPR scan curves were identical in shape and the height of the fluorescence scan curves increased with increasing x_{Label}. The small variation of the scan curves is caused by small differences in the thickness of the gold samples used in the experiment. Plotting the peak fluorescence values obtained from the scan curves versus x_{Label} revealed that the fluorescence yield increased sub-linear (fig. 4.17b). Thus, incorporation of labeled dNTP is not a statistical process at very high label concentrations. The inset displayed in fig. 4.17b, shows additional data points monitored at very low mole fractions without using an attenuator. There, the increase is linear, which is in agreement with the slow overall increase. The result is in good agreement with the literature, as label incorporation was never investigated for $x_{Label} > 0.5$ and the data reported here also increase linearly within in the range x_{Label} $0 \leq 0.5$.

4.8 Influence of base mismatches

DNA polymerases have the ability to copy DNA with extremely high fidelity; for DNA polymerase I, the probability of an error during replication is $<10^{-6}$ per nuctleotide addition [Bebenek, 1990]. The mechanisms available to reduce the error rate are 1) selection of the correct dNTP, 2) inefficient extension of mispaired 3'-primer termini and 3) excision of the mispaired base from the primer terminus by the proofreading 3'-5' exonuclease activity [Echols, 1991]. In KF's crystal structure the polymerase and exonuclease active sites are spatially separated by 30 Å. While DNA was shown to bind as double strand at the polymerase site, the exonuclease domain strongly favors single-stranded DNA. Upon proofreading the primer terminus must shuttle from one active site to the other. For KF two pathways are reported: the intermolecular pathway postulates dissociation of the polymerase/DNA complex and subsequent rebinding at the exonuclease site. Alternatively, the primer terminus translocates intramolecularly from the polymerase to the exonuclease domain by melting of 3-4 bp at the primer terminus [Freemont, 1988]. Fluorescence anisotropy measurements using dansyl-labeled DNA substrates exhibiting terminal, internal or consecutive mismatches within the last four bases of the primer terminus revealed substantially increased partitioning constants K_{pe} (giving the ratio of DNA bound to the exonuclease : KF bound to the polymerase domain) [Carver, 1994]. These results demonstrate that proofreading is not a randomly occurring process but it is triggered by aberrations in the geometry and melting capacity of the primer terminus. Using KF derivatives having mutations in the polymerization site, particular amino acids involved in mismatch recognition could be identified [Thompson, 2002]. Although this intramolecular pathway for travelling between the exonuclease and polymerase site is available to the enzyme, it is not invariably used; in

any case, the dissociation rate will increase upon introduction of a mismatch to the primer terminus causing lower affinities to this substrates.

In this chapter, the influence of two types of base mismatches in the primer/template region on the elongation of DNA will be demonstrated: a terminal base mismatch has been introduced into P45/T50G1 close by substitution of the terminal cytosine by guanine (P45 tG/T50 G1close, H in fig. 4.2), resulting in a G-G mismatch. The other substrate tested had a G-G mismatch three nucleotides upstream of the 3'-terminus of the primer (P45 iG/T50 G1 close, I in fig. 4.2):

P45 tG/T50 G1 close

```
5'-Biotin-(T)30 ACG TCA GTC TCA CCG-3'
            3'-TGC AGT CAG AGT GGG TG TTA TAA GTG AGT CGG TGA TGA TGG AGA CAT TGA-5'
```

P45 iG/T50 G1 close

```
5'-Biotin-(T)30 ACG TCA GTC TCA GCC-3'

            3'-TGC AGT CAG AGT GGG TG TTA TAA GTG AGT CGG TGA TGA TGG AGA CAT TGA-5'
```

Carver et al. used similar primer/template duplexes, also having three terminal cytosines, in time-resolved fluorescence studies and found partitioning coefficients K_{pe} of 0.22 for terminal G-G mismatches and 0.46 for an internal G-G mismatch 3 nt upstream of the 3'-primer terminus (c. f. $K_{pe} = 0.07$ for fully complementary oligonucleotides) [Carver, 1994]. Thus, the internal mismatch had stronger impact on K_{pe} than the terminal one.

Since the introduction of a single mismatch is likely to destabilize a 15-mer duplex substantially, which in turn would alter the number of DNA substrates available at the surface for KF binding, the stability of the different DNA substrates has been checked using SPR (fig. 4.18).

While immobilization of three different primers differing in a single base caused identical reflectivity shifts (corresponding to a surface coverage of ~65 ng/cm^2), the reflectivity shift observed for the formation of the fully complementary duplex (37 ng/cm^2) was almost twice as high as that found for the singly mismatched duplexes (21 ng/cm^2). Thus, in experiments probing KF binding to mismatched DNA substrates, only half the number of binding sites was available. Fig. 4.19 compares the enzymatic extension of DNA substrates being either fully complementary or mismatched, carried out at otherwise identical conditions: 7.6 nM KF were immobilized prior to the addition of 0.5 µM dATP, dGTP, dTTP and Cy5-dCTP. In the SPFS experiments presented, the reflectivity has been converted into mass per mole immobilized DNA. While about ~16 ng/pmol KF bound to the perfectly matched DNA substrate (fig. 4.19a), only 10 ng/pmol and 5 ng/pmol KF were observed for the DNA substrates having an internal (fig. 4.19b) and a terminal mismatch (fig. 4.19c), respectively.

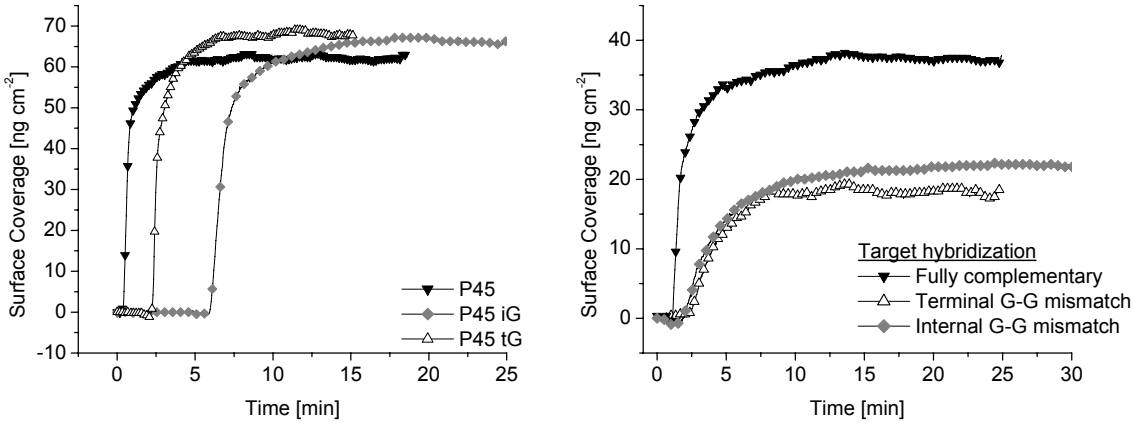

Figure 4.18: SPR data for the immobilization of primer strands P45 (black triangles), P45 iG (gray diamonds) and P45 tG (open triangles) and its subsequent hybridization to an identical target T50G1close forming fully complementary, or DNA substrates with an internal or terminal G-G base mismatch.

However, the association rate of binding to mismatched DNA seemed to be faster than that for the matching DNA substrate and lacks the initial linear binding phase. Addition of dNTP substrates did not initiate DNA polymerization in the presence of a terminal mismatch, although it caused the enzyme's release. The replication process was tremendously slowed down for the substrate P45iG/T50G1close; it finished after 80 minutes compared to 3 minutes for P45/T50G1close. From these data it becomes obvious that the rate of enzyme release does not necessarily correlate with the velocity of DNA synthesis like shown in chapter 4.6 where the rate of enzyme release was reported to increase with the concentration of dNTP substrates. In the case of P45iG/T50G1close, the majority of the enzyme molecules was released prior to completeness of the polymerization reaction, which could indicate a lower processivity caused by translocation between the exonuclease and the polymerase domain via the intermolecular pathway. Thus, the reaction is often interrupted by dissociation and rebinding events. The experiments shown here, demonstrate that surface-based primer extension assays are efficient in detecting point mutations in DNA.

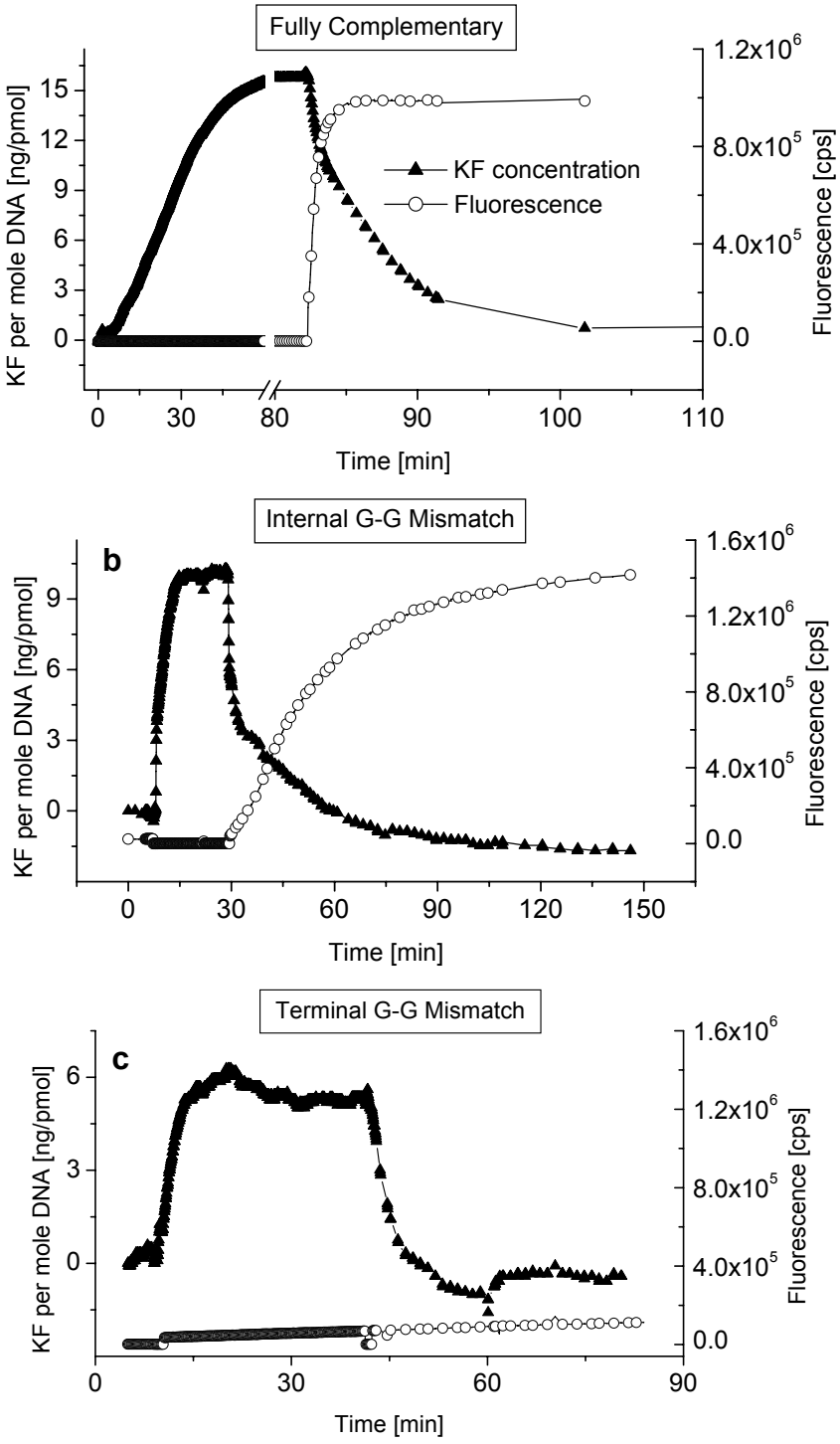

Figure 4.19: Influence of single base mismatches in the primer/template region on DNA replication and KF binding. a: Fully complementary primer. b: Internal G-G mismatch. c: Terminal G-G mismatch. While the internal mismatch 3 nt upstream the 3'-terminus of the primer decelerated the elongation process, a terminal mismatch inhibited the reaction entirely.

4.9 Conclusions

The enzymatic in vitro synthesis of DNA gained increasing interest within the last years. A number of biotechnological processes are known that employ DNA polymerases as tool to incorporate dye-labeled nucleotides into DNA. DNA sequencing techniques and real-time PCR are typical applications. The current trend for miniaturization and for methods capable of high-throughput screening has promoted the development of DNA microarrays that are compatible with enzyme reactions. In microarray formats, DNA polymerases have been utilized for single base mismatch detection [Little, 1999, Lizardi, 1998, Schweitzer, 2001, Westin, 2000], as tool to create double-stranded DNA for screening the affinities of DNA-binding proteins [Wang, 2003] and for re-sequencing of single-stranded DNA on the single-molecule level [Braslavsky, 2003].

An advanced understanding of the fundamental processes these reactions rely on can substantially improve the design of DNA constructs and surfaces beneficial for enzyme reactions. Therefore, this thesis aimed at the investigation of the versatility of SPFS spectroscopy as tool for studying DNA polymerization. The major advantage of SPFS is the wealth of information accessible by combining a mass-sensitive method like SPR with highly sensitive fluorescence detection. Using this technique, it was possible to observe binding of the Klenow fragment to immobilized DNA, its enzymatic elongation, and enzyme release from complete DNA duplexes in real-time.

The KF was shown to bind to DNA substrates exhibiting a 35-mer base overhang with an affinity constant of $K_A=1.3\times10^8\ M^{-1}$. This is comparable with results obtained in solution indicating that the binding events were not perturbed by the proximity to the surface. A 2D streptavidin arrangement employed for immobilization of biotin-modified DNA strands seems to provide a well-suited environment for DNA polymerase action. Yet, binding appears to be sterically demanding if one considers the maximum surface coverage of one KF per streptavidin molecule. Although 18% of the streptavidin molecules were found to carry a second DNA probe, it is not entirely clear if these probes hybridize to the template strand. Therefore the low surface coverage could as well be attributed to the absence of a second double-stranded DNA substrate per streptavidin molecule. The introduction of a spacer region into the primer strand was not found to be crucial for KF binding. Even biotinylated primers lacking a spacer region were bound by KF with identical affinity.

Incorporation of Cy5-labeled dCTP could be detected with high time resolution and sensitivity. Dye concentrations down to 4.7 fmol/cm^2 were successfully sensed, corresponding to single labeling of 1 out of 1000 available DNA strands. The number and position of the attached chromophors is central to the fluorescence yield observed in an extension reaction. Here, the relation between the number of labels and fluorescence yield is not simply linear but depends strongly on the distance between incorporated

dyes and between the dye and the gold surface. Maximum fluorescence intensity was yielded for attachment of one dye-label per DNA strand. Low label densities were either achieved by using templates processing only one guanine to pair with cytosine or by adding unlabeled dCTP to the reaction mixture. In contrast to previous reports, a strong preference for the natural dNTP substrate was found for Cy5-mole fractions ≥0.5. Thus, working with Cy5-mole fractions < 0.5 resulted in lower label efficiencies than expected for a linear relation between fluorescence yield and Cy5-mole fraction. By enzymatically labeling the position opposite to the 5'-terminus of template, DNA replication was shown to be efficient in leaving completely double-stranded DNA. However, indications were found that DNA polymerization was not complete in all cases and stopped before addition of the last complementary bases.

Varying the concentration of KF bound to surface-tethered DNA demonstrated that immobilization of KF prior to initiation of DNA polymerization does not inactivate the enzyme. A linear relationship between KF surface concentration and polymerization velocity confirmed bound KF being the catalytically active species. Since KF binding is slow compared to chemical bond formation and dNTP binding, this step controls the overall reaction velocity. An analysis of the elongation kinetics according to the Michaelis Menten model revealed kinetic constants very similar to those obtained from solution measurements.

Using SPFS, primer extension assays have been carried out in order to detect single base mutations in DNA. As known from microarray applications a terminal mismatch in the primer/template duplex inhibited DNA polymerization. Besides reproducing this observation it could be shown that monitoring the kinetics for primer extension also allows for discrimination of internal mismatches since the replication rate is significantly slowed down in this case. In this regard, the method is superior to DNA microarrays where the final fluorescence yield is the only means to judge the presence of a mismatch.

In summary, SPFS was shown to be a valuable tool for the biochemical characterization of enzyme activity uncoupled from the natural biological environment. Enzyme function was not found to be impaired so that one can fully profit from the advantages of a biosensor format.

5 QCM-D in studies of hybridization and replication of DNA

5.1 Experimental section

As reported in chapter 4, SPFS is a versatile tool for studying enzymatic DNA synthesis in real-time. Using dye-labeled nucleotides, the incorporation of these nucleotides into surface-attached oligonucleotides could be followed with a high time-resolution and sensitivity. However, the introduction of a label might influence the replication process, for instance by rising the number of prematurely terminated replication products and limits the range of dNTP substrate concentrations that can be applied. In order to confirm the findings reported in chapter 4 and to gain further insights, QCM-D was used as a complementary method (see chapter 2.3 for an introduction into this technique) to study the present polymerase/DNA system. Refer to the cartoons of the sensor architecture shown in chapter 4 (fig. 4.1 and 4.2). Cleaning procedures, buffer conditions and the base sequences of the used oligonucleotides can be also found in the appendix.

The clean gold electrodes of a quartz crystal were first functionalized with a self-assembled monolayer (SAM) of biotinylated thiols (see chapter 3.3.1). After the gold electrode was immersed for one hour in the thiol solution, it was rinsed with MilliQ water, dried in a stream of nitrogen and mounted into the Q-Sense reaction chamber. The quartz was thoroughly rinsed with PBS buffer for 15 min. Subsequently, the following immobilization steps were carried out: First, streptavidin was bound from a 1 µM solution to the SAM. The respective probe (primer) (1 µM) was bound to the streptavidin layer and hybridized to target (template) T50 (1 µM). The hybridization step was either carried out in PBS or HSM buffer. T50 was phosphorylated at the 3'-end in order to prevent it from being extended by the DNA polymerase; the biotin was attached via a -$[CH_2]_6$- alkyl linker to the 5' end of the probes. The specificity of the hybridization reaction was checked in a separate experiment in which the DNA probe was exposed to a completely non-complementary DNA target, which did not result in any shift (data not shown).

The DNA extension assays were carried out using the exonuclease-free Klenow mutant of the *E. coli* DNA polymerase I and the four deoxynucleotidetriphosphates (dNTP) in HSM buffer (10 mM HEPES pH 7.4, 150 mM NaCl, 10 mM $MgSO_4$). The particular concentrations are given in the respective result sections.

Three DNA constructs differing in the length of their poly-thymine spacers are relevant for the present work. Fig. 5.1 sketches the architectures built upon DNA hybridization and extension.

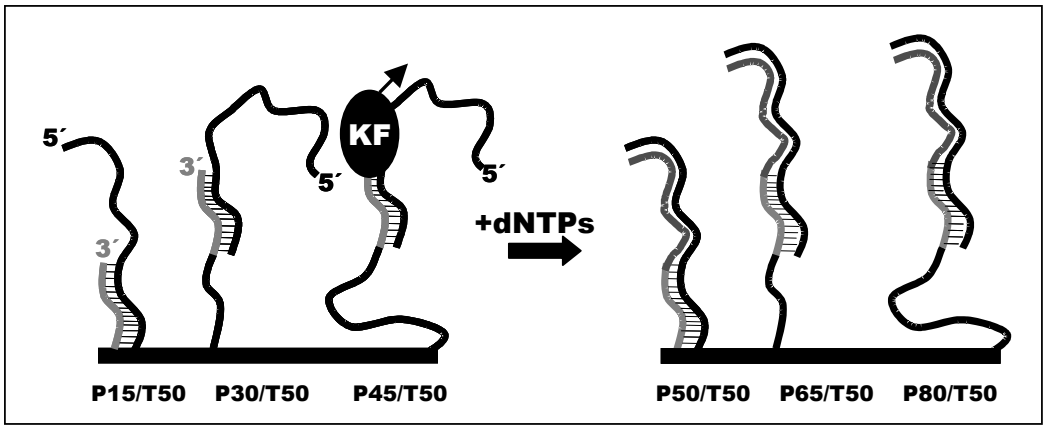

Figure 5.1: Picture of DNA duplexes formed upon enzymatic DNA extension. The names of the DNA substrates and reaction products are indicated.

The used quartz crystal had a fundamental frequency of 5 MHz; in each experiment, changes in frequency (Δf) and the dissipation factor (ΔD) were measured simultaneously at three overtones, n= 3, 5 and 7.

5.2 Streptavidin arrangement for DNA immobilization

Fig. 5.2 depicts the kinetics for the binding of streptavidin to a self-assembled monolayer of biotinylated thiols. The simultaneously measured changes in ΔD and Δf obtained at n=3 are plotted as a function of time. Note that frequency shifts will be always presented divided by their overtone number within this thesis.

The graph represents QCM-D raw data being typical of a rigid film. Two factors indicate this property: Firstly, the system response does not depend on the overtone number; accordingly, ΔD and Δf acquired at the overtones n=3, 5 and 7 are identical. Secondly, while the quartz responded with a large frequency shift to the injection of streptavidin solution, the energy dissipation remained almost constant (see chapter 2.3.3 for an explanation of ΔD). This means that the mass added upon streptavidin adsorption behaved nearly perfectly elastic and hence, coupled completely to the shear motion of the quartz. Data analysis based on the Sauerbrey equation (eq. 2.23) is rather reliable for such systems. However, a small negative shift in ΔD was observed immediately after the streptavidin injection in all experiments. It might be attributed to a reduction of energy dissipation in the initial binding phase of streptavidin resulting from processes increasing the order (orientation) within the SAM. The SAM consisted mainly of short-chain hydroxyl-terminated thiols serving as lateral spacer molecules and a small amount of biotinylated long-chain thiols. The free dangling ends of the long-chain thiols might

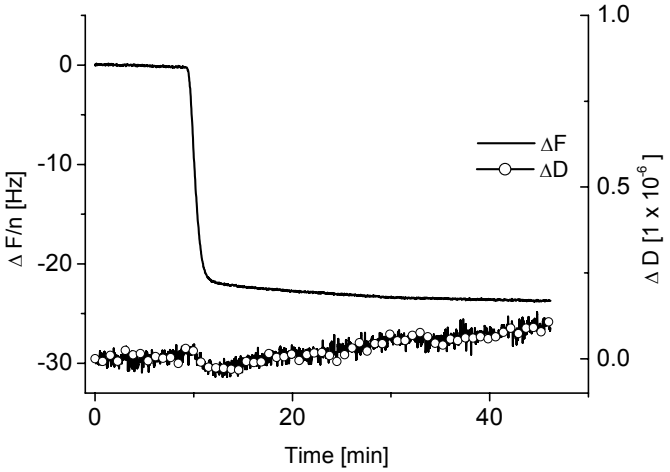

Figure 5.2: QCM-D response at n=3 for the immobilization of streptavidin on top of a SAM from biotinylated thiols. As typical for rigid films, the shift in energy dissipation, ΔD, was negligible. Note that the QCM-D response monitored at higher harmonics (n=5,7) was identical and is therefore omitted in the presentation.

cause some energy dissipation that is temporarily decreased when they become oriented upon streptavidin binding. Since the used thiols were only soluble in ethanol and the water/ethanol exchange was incomplete in the flow chamber, reference measurements giving the dissipation factor for an unmodified gold surface are not available to prove the assumption.

Using the Sauerbrey equation, the surface coverage of streptavidin was calculated to 424 ng/cm^2. The sample-to-sample variation was ± 30 ng/cm^2. Comparing SPR data obtained for the same system (209 ng/cm^2, see chapter 4.3), an effective layer density of 1.15 g cm^{-3} results, confirming a water content of 50 % for the streptavidin layer as reported elsewhere [Höök, 2001]. Using this density, the layer thickness can be estimated to 4 nm. The dimension of a single tetrameric streptavidin molecule was determined to be 5.6 nm × 4.2 nm × 4.2 nm from the crystal structure [Weber, 1989] supporting the assumption of a monomolecular streptavidin film. In such a monolayer, 56 % of the surface is covered with streptavidin molecules.

The result is in excellent agreement with literature data for thiol-supported streptavidin monolayers [Knoll, 2000]. Höök et al. found a thickness of 4.7 nm for streptavidin layers grown on biotin-doped lipid bilayer using QCM-D [Höök, 2001]. Under these conditions the protein is likely to form a 2D crystal [Darst, 1991], with two of the four binding sites contacting the lipid bilayer and the other two pointing into the bulk phase. The height of such a 2D crystal was confirmed to be 4.7 nm by high-resolution atomic force microscopy [Scheuring, 1999] as well as ellipsometric data [Reiter, 1993].

In conclusion, the streptavidin layer formed on top of the thiol SAM is very likely to be monomolecular. This interpretation is strongly supported by thickness data obtained

from optical and acoustic methods. However, from thickness data alone one cannot tell if 2D crystallization has occurred. Presumably the monolayer formed on the thiol SAM does not undergo the transition to a 2D crystal because of the lacking mobility of the supporting structure. Due to the high affinity of the biotin/streptavidin system, the streptavidin adsorption follows the random sequential adsorption model (RSA) [Onoda, 1986]. This implies that any kind of rearrangement within the protein layer, which is certainly needed for crystallization, has to be mediated by the supporting structure. A lipid bilayer with its fluid properties meets this requirement definitely better than thiols covalently attached to gold.

Irrespectively, the usefulness of the biotinylated thiol SAM for the built-up of a laterally diluted, highly reproducible platform for oligonucleotide hybridization has been proven before and will be demonstrated again in the following section about DNA hybridization.

5.3 Elongation of primers differing in spacer length

5.3.1 DNA hybridization and DNA extension: Sauerbrey interpretation

Fig. 5.3a-c displays the response in ΔD and Δf (n=3, 5 and 7) versus time for the enzymatic elongation of the duplexes P15/T50, P30/T50 and P45/T50, respectively. The QCM-D set-up was run in the batch mode, thus without circulation of the liquid, which is different from experiments that will be discussed in chapter 5.4. Each experiment started at point 1 with the immobilization of a biotinylated DNA probe (1 µM, PBS) on the streptavidin layer, followed by hybridization to the complementary target T50 (1 µM, PBS, point 2). The DNA probes share a 15-mer recognition sequence and differ only in the length of their spacers. They exhibit 0, 15 and 30 thymine bases attached to the biotin-modified 5'-terminus of the primer. Hybridization produces partially double-stranded DNA with a recessed 3'OH moiety (see fig. 5.1) that offered a binding site for a DNA polymerase. After the duplex formation was complete, the PBS buffer was exchanged against HSM buffer (point 3), giving rise to an instantaneous drop in energy dissipation, whereas the frequency remained constant. The analysis of QCM-D data obtained for identical DNA films either immersed in PBS or in HSM buffer, respectively, yielded a lower effective thickness for the DNA film immersed in HSM buffer. In this case, the DNA strands adopt more compact structures due to a reduced Coulombic repulsion in the presence of bivalent metal ions. These compact structures dissipate less energy, which is why ΔD drops down after the buffer exchange. The rapid drop during the buffer exchange is also caused by the properties of the bulk liquid since they also contributes to the QCM-D response.

Shortly after that, the DNA polymerase (7.6 nM, HSM) was added at point 4, not causing a detectable QCM-D signal. Exposure of the DNA substrate to a mixture of dNTPs (10 µM) and KF (7.6 nM), injected at point 5, initiated the enzymatic DNA extension. The same experiment performed with a DNA substrate that is identical but features a mismatched G-G base pair at the 3'-terminus, inhibited the reaction entirely, thereby confirming the specificity of the reaction (data not shown). In addition, the specificity was proven by first adding the dNTP mixture and than the DNA polymerase. The bare presence of dNTPs did not cause any signal.

The QCM-D response observed for surface modifications involving DNA was typical of viscoelastic films. The dissipation factor changed significantly upon DNA binding and the overall response was frequency-depended causing a separation of the responses acquired at different overtones. In the following section, analysis of the experimental data using the classical Sauerbrey theory will be compared with results obtained from a Voigt viscoelastic model. Although the Sauerbrey eq. allows for a qualitatively correct interpretation of the overall kinetics, the interpretation can be substantially improved using the Voigt model. Table 2 compares the results obtained from QCM-D and SPR measurements for the three different spacer systems. The experimental variation of the raw data was 2 % for streptavidin and 5 % for all other layers.

As calculated from SPR measurements, the surface concentration of streptavidin is about ~3.8 pmol/cm^2 (209 ng/cm^2). Theoretically each streptavidin molecule offers binding sites for two biotinylated molecules. Considering the surface concentration of ~4.6 pmol/cm^2 (66 ng/cm^2) for P45, we conclude that 62 % of the binding pockets are occupied by a probe molecule. The mass ratio $\Delta m_{QCM}/\Delta m_{SPR}$ is about 10 for both, single-stranded probes and probe/target duplexes, thereby intriguingly demonstrating two facts: firstly, the mass uptake sensed by QCM-D cannot correspond to the molecular mass of adsorbed molecules only. The excess amount must be attributed to water that couples as an additional mass via direct hydration, viscous drag and/or entrapment in cavities in the adsorbed film.

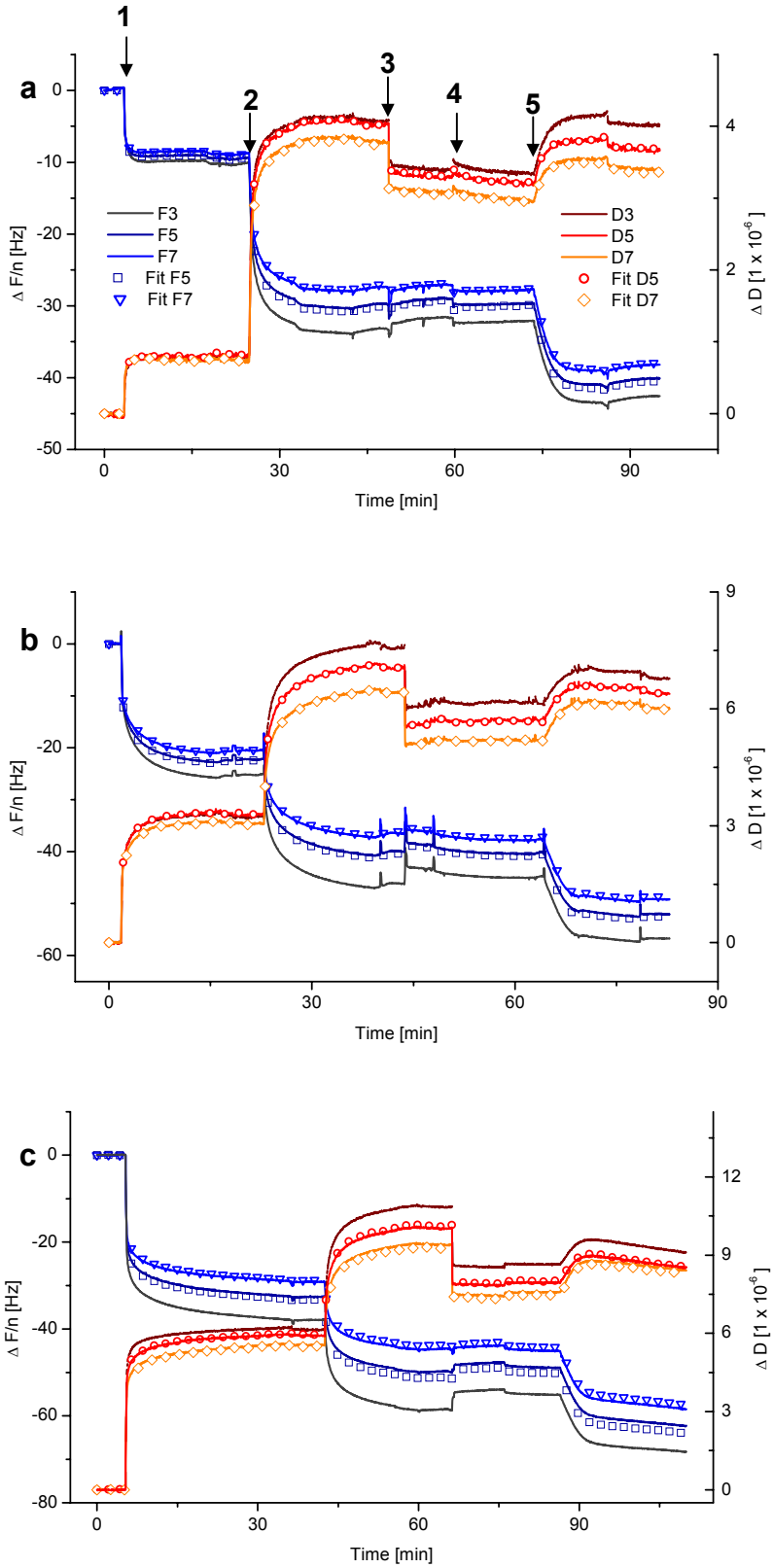

Figure 5.3. Plot of Δf and ΔD versus time for the immobilization of different primers (point 1; in a: P15; b: P30; c: P45) and the subsequent hybridization to an identical template T50 (point 2). After hybridization, PBS buffer was exchanged by HSM buffer (point 3) and a small amount of KF injected (point 4). Addition of the dNTP mixture initiated DNA elongation (point 5). Best fits obtained from the Voigt model (see the results in fig. 5.5) are shown as scatter for n=5 (open circles) and 7 (open diamonds).

For this reason, thicknesses obtained from QCM-D measurements are effective hydrodynamic thicknesses characterized by an effective density that is described by eq. 2.26. Since SPR is proportional to the mass of the "dry" film only, comparison of QCM-D data with optical data can provide valuable information concerning the water content of a film. Secondly, the amount of water that couples to the DNA strands increased linearly with DNA mass/length. Every single-stranded 15-mer contributes ~200 ng/cm^2. One may conclude that the probes do not significantly differ in their secondary structure and have similar chemical environments so that they couple to siliar amounts of water. The mass gain upon hybridization with T50 was ~430 ng/cm^2 for P15, ~370 ng/cm^2 for P30 and ~370 ng/cm^2 for P45, which is also a factor of 10 larger than Δm_{SPR}.

In the experiments shown above, binding of the Klenow fragment to DNA could not be monitored. This might be reasoned by low effective enzyme concentrations caused by losses due to unspecific adsorption of enzyme molecules to the tubing of the reaction chamber and depletion of the surface if the experiments were performed in batch mode. In later experiments, polymerase binding could be greatly improved by modifying the reaction conditions (see chapter 5.4).

However, addition of a mixture of KF and dNTPs (figures 5.3a-c; point 5, respectively) to surface-attached DNA substrates initiated DNA polymerization. The elongation of the DNA strands caused initially an almost linear decrease of Δf, being accompanied by an increase in ΔD. Thereby, ΔD and Δf differed slightly in their time evolutions, which distinguished the QCM-D response for DNA replication from that for DNA hybridization. The equilibrium was reached within ten minutes. A subsequent rinsing step confirmed the covalent incorporation of nucleotides. The three DNA substrates differing in their spacer lengths were elongated using identical reaction conditions. The changes in Δf and ΔD monitored for the elongation steps in the three sets of experiments were almost identical; the initial slope of Δf was found to be ~3 Hz/ min, while that for ΔD amounted to 0.3×10^{-6}/ min. The total mass increase according to the Sauerbrey picture was about ~220 ng/cm^2 irrespective of the spacer length. Therefore, one can conclude that neither the replication efficiency nor the replication velocity were influenced by the position of the DNA polymerase relative to the surface.

The following chapter will interpret the results obtained from the experiments presented here on the basis of the Voigt viscoelastic model.

Table 2: Comparison of the mass of DNA films measured by SPR and QCM-D.

Reactions in PBS buffer [a]	Δm_{SPR} [c] [ng/cm^2] (pmol/cm^2)	$\Delta m_{Sauerbrey}$ (from n=3, eq.2.23) [ng/cm^2]	$d_{effective}$ [d] (eq.2.27) [nm]
P15	31 (6.9)	170	1.6
P30	51 (5.6)	451	4.3
P45	66 (4.6)	623	5.9
P15/T50	68	595	5.6
P30/T50	89	818	7.7
P45/T50	117	986	9.3
Primer extension in HSM buffer[b]			
P50/T50		210	7.6
P65/T50		248	10.0
P80/T50		255	11.7

a) Total mass uptake refers to the streptavidin layer in PBS buffer.
b) Total mass uptake refers to the DNA duplexes in HSM buffer.
c) see chapter 4.3.
d) $d_{effective}$ ($=\Delta m_{Sauerbrey}/\Delta\rho_{effective}$) was calculated assuming $\rho_{effective}=1.06$ g/cm^3 as taken from related systems [Larsson, 2003].

5.3.2 Data analysis using the Voigt model

The frequency-dependent response of surface reactions involving DNA and the dissipative losses are attributed to the viscoelastic nature of the formed films. In this case, the system response does not only depend on the shear stress but also on the shear rate that is applied. In the following, data analysis will be carried out using a Voigt-based viscoelastic model and deviations from the Sauerbrey interpretation will be outlined.

The Voigt model represents every adsorbed layer as a homogenous viscoelastic film being characterized by an effective density (ρ), thickness (d), shear elastic modulus (μ) and shear viscosity (η) (see chapter 2.3.5). Although we are dealing with a multi-layer architecture, consisting of a thiol, streptavidin and DNA film, the experimental data were modeled as one homogenous film. To do so, Δf and ΔD values were offset after the formation of the streptavidin layer, assuming it as perfectly elastic. Since the Voigt model provides only a simplistic representation of a real system, all output data should be considered as effective parameters. A measurement at two harmonics, yielding four parameters, is sufficient to perform a fit, provided one of the parameters is kept fixed during the modeling. Here, the effective density was fixed at $\rho = 1.06$ g cm^{-3} (value taken from literature). However, to check whether the frequency dependence implemented in the Voigt model holds true, the modeling was carried out on two sets of harmonics, i.e. n=3/5 and n=5/7. The results of the modeling for the three sets of experiments, the raw data of which are shown in fig. 5.3a-c, are summarized in table 3. The best fits for n= 5 and 7 are plotted with the raw data in figures 5.3a-c. The

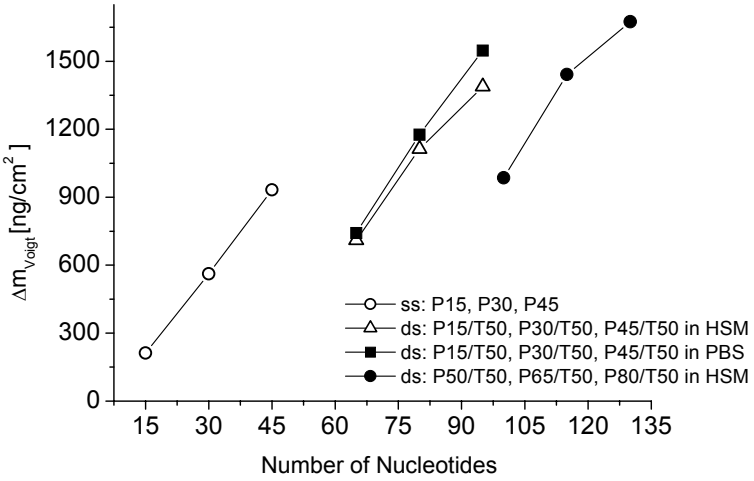

Figure 5.4: Final mass of DNA films as calculated from the Voigt viscoelastic model. The films were built-up from primers (open circles) differing in length that were subsequently hybridized to T50 (black squares). Note the small shrinkage and deviation from linearity observed for the DNA hybrids after switching from PBS to HSM buffer (open triangles). According to the Voigt model, the enzymatic elongation (black circles) of the primed templates caused an identical increase in mass.

agreement between fit and measured data was typically within 5 % for both harmonics. Yet, the agreement was typically a little better for harmonics n= 5/7, which indicates material properties the Voigt model does not account perfectly for.

The trend obtained for the film mass ($\Delta m_{Voigt}=\Delta\rho_{effective}\cdot\Delta d_{Voigt}$) compares very well with that calculated from the Sauerbrey equation. The absolute values differed by 20-30 %. Fig. 5.4 nicely illustrates the almost linear increase in Δm_{Voigt} for single-stranded and double-stranded DNA. Hybridization and extension reactions lead to identical mass increases for the three different primers, demonstrating that they are equally well suited as catcher molecules for target hybridization and as substrates for polymerase reactions. The increase of the spacer length by 15 nucleotides added about 350 ng/cm^2 in mass, while the mass increase upon target hybridization amounted to ~500 ng/cm^2 for all probes. Upon DNA extension the weight of the layers increased by another ~250 ng/cm^2. Note that switching from PBS to HSM buffer decreased the thickness for double-stranded DNA substrates slightly. The effect was more pronounced for longer probes. One reason might be an improved shielding of the negatively charged phosphate backbone of DNA by bivalent Mg^{2+} ions present in the HSM buffer. Fig. 5.5 gives typical output parameters obtained from data analysis using the Voigt model: the time courses for shear viscosity, shear modulus and effective thickness for reaction steps 1 and 2 (probe immobilization + target hybridization) are shown in 5.5a-c, the corresponding plots for reaction step 5 (elongation) are displayed in 5.5d-f.

Low values in viscosity and shear modulus are typical of molecular structures which are loose and flexible, whereas large values indicate stiff architectures. Significantly, both, viscosity and shear modulus increase with decreasing length of the probe

molecule. While the hybridization reaction does not affect the viscoelastic properties of P30 and P45, P15 reacted with a drop in η and μ. Taking into account the persistence length of ~1.3 nm for single-stranded DNA [Tinland, 1997], probe P15 is the only construct likely to adopt a rod-like structure, which is expressed in larger values for η and μ.

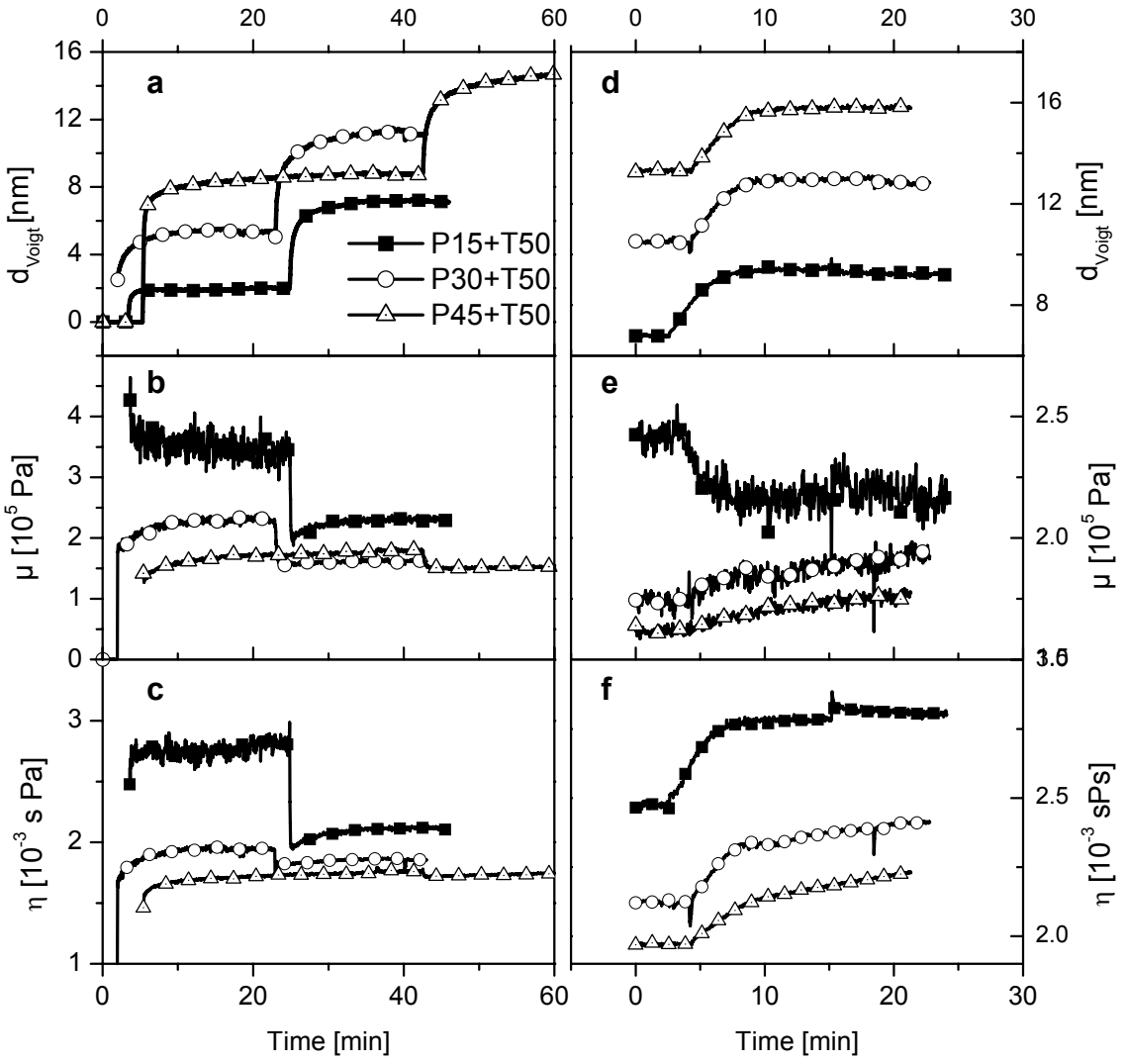

Figure 5.5: Time evolution of thickness d_{Voigt} (top), shear modulus μ (middle) and shear viscosity η (bottom) as obtained from the Voigt model. The streptavidin layer was excluded from the modeling and a fixed film density of 1.06 g/ml was used. a-c: Immobilization of different primers and hybridization to an identical target. The corresponding best fits are shown together with the raw data in fig. 5.3. Note that the model is not able to represent the initial phase of binding of the primer strands to the streptavidin layer. d-f: Enzymatic extension of different primers. Initial thickness values for the DNA substrates are smaller than presented in the left panel because PBS was exchanged against HSM buffer before primer elongation.

Table 3: Analysis of the hybridization and elongation of DNA primers exhibiting different spacer lengths using a Voigt-based viscoelastic model.

DNA in PBS buffer	d_{Voigt} [nm] n=3/5 (5/7)	μ_{film} [10^5 Pa] n=3/5 (5/7)	η_{film} [10^{-3} s Pa] n=3/5 (5/7)
P15	2.0 (2.0)	3.4 (3.9)	2.8 (2.8)
P30	5.3 (6.2)	2.3 (1.4)	1.9 (2.1)
P45	8.8 (8.2)	1.8 (2.4)	1.8 (1.7)
P15/T50	7.0 (6.9)	2.3 (2.9)	2.1 (2.1)
P30/T50	11.1 (13.8)	1.6 (1.0)	1.9 (1.8)
P45/T50	14.6 (13.3)	1.5 (2.3)	1.7 (1.7)
DNA in HSM buffer			
P15/T50	6.7 (6.5)	2.4 (3.2)	2.4 (2.4)
P30/T50	10.5 (12.4)	1.7 (1.0)	2.1 (2.2)
P45/T50	13.1 (11.8)	1.9 (1.3)	2.0 (1.9)
P50/T50	9.3 (9.0)	2.2 (3.4)	2.8 (2.9)
P65/T50	13.0 (14.6)	1.9 (1.3)	2.4 (2.5)
P80/T50	15.8 (14.0)	1.9 (3.6)	2.4 (2.3)

5.4 Monitoring polymerase-DNA interactions

The previous chapter reported enzymatic primer extension reactions monitored by QCM-D. Three different primers with varying spacer lengths were tested in the extension assay. They were replicated with identical rates, demonstrating that the enzyme was not impaired by the proximity to the surface. However, due to unsatisfactory experimental conditions, binding of the Klenow fragment to immobilized DNA was not observed. In order to improve the experiment, efforts were directed towards an increase of the effective enzyme concentration. Firstly, all measurements were carried out at a constant flow rate of 0.2 ml/min at T=21°C. This is the highest flow rate that still guarantees optimal temperature control of the flow chamber. Furthermore, the tygon tubing of the circulation system were pre-coated with BSA (0.05 mg/ ml) for 20 min. Secondly, the enzyme concentration was increased to 30 nM in the binding and extension assays. And last, all reaction steps were performed in HSM buffer, which enables a direct comparison between Δf and ΔD values for DNA hybridization and DNA extension. Besides that, the reaction conditions were identical with those described in paragraph 5.1.

5.4.1 DNA polymerase binding

Single binding experiment

Fig. 5.6a shows binding of the KF to DNA duplex P15/T50 in the absence of dNTPs. First P15 (1 μM) was immobilized on streptavidin (point 1) and hybridized to target T50 (1 μM) (point 2). Than, KF was added at a concentration of 30 nM (point 3). In a previous experiment, single-stranded DNA was exposed to a KF solution (30 nM) to check for unspecific binding. Only a negligible frequency shift was observed. Thereafter at point 4, KF was removed by rinsing with 1 M NaCl. The binding step was repeated in HSM buffer containing 10 mM $CaCl_2$ instead of 10 mM $MgSO_4$ (point 5). In contrast to the cofactor Mg^{2+}, Ca^{2+} does not enable polymerase activity, but it is known to occupy the binding site for bivalent metal ions so that binding should occur with identical affinities. At point 6, a 100 μM dNTP-mix was added to check, whether KF is catalytically active in the presence of Ca^{2+} ions.

The experiment demonstrated successful binding of KF to a surface-attached DNA substrate. The drop in Δf was rapid and binding was complete after 15 min, buffer rinsing for 15 min did not reduce the adsorbed mass. Due to the low flow rates used in QCM experiments, it was impossible to rinse off the KF in a reasonable period of time in order to measure the dissociation rate. Surprisingly, ΔD was – 0.5, indicating that the DNA layer gained rigidity upon KF binding. At the same time, the separation between the responses of the different overtones was reduced. Negative shifts in ΔD have not been reported for protein adsorption to solid supports yet. The systems that were mostly studied are antibody-antigen interactions and unspecific adsorption of proteins like BSA to various surfaces. There, the formation of the protein layer induced additional viscous losses since the protein films were less rigid than the surface was prior to adsorption [Höök, 1998]. The situation is different in the present experiments. Here, the starting-point was a low density DNA film containing up to 90 % water with flexible elongated DNA strands acting as tails of an oligo-electrolyte brush. Since it is known from the co-crystal structure of KF in complex with double-stranded DNA that the enzyme encloses DNA thereby restricting its flexibility, a significant increase in the rigidity of the DNA film is expected upon binding of the KF [Patel, 2001].

The viscoelastic parameters obtained from the Voigt model are plotted in fig. 5.6b, the results will be discussed in more details in chapter 5.4.2.2. Since the shear viscosity was found to be more robust than the shear modulus (and both parameters have the same qualitative meaning), the discussion in the following sections will focus on the shear viscosity only.

KF binding was shown to be reversible by regeneration of the surface using sodium chloride. The DNA architecture was not affected by the salt treatment and a comparable

amount of KF could be bound in a second injection. ΔF_3 were –8 Hz and –11 Hz, respectively. The deviations might be caused by differences in the effective enzyme concentrations. Judging from the kinetics, the natural cofactor Mg^{2+} can be substituted by Ca^{2+} without changing the affinity of the enzyme, although it is not catalytically active under these condition. This was proven by the addition of dNTPs not having any effect.

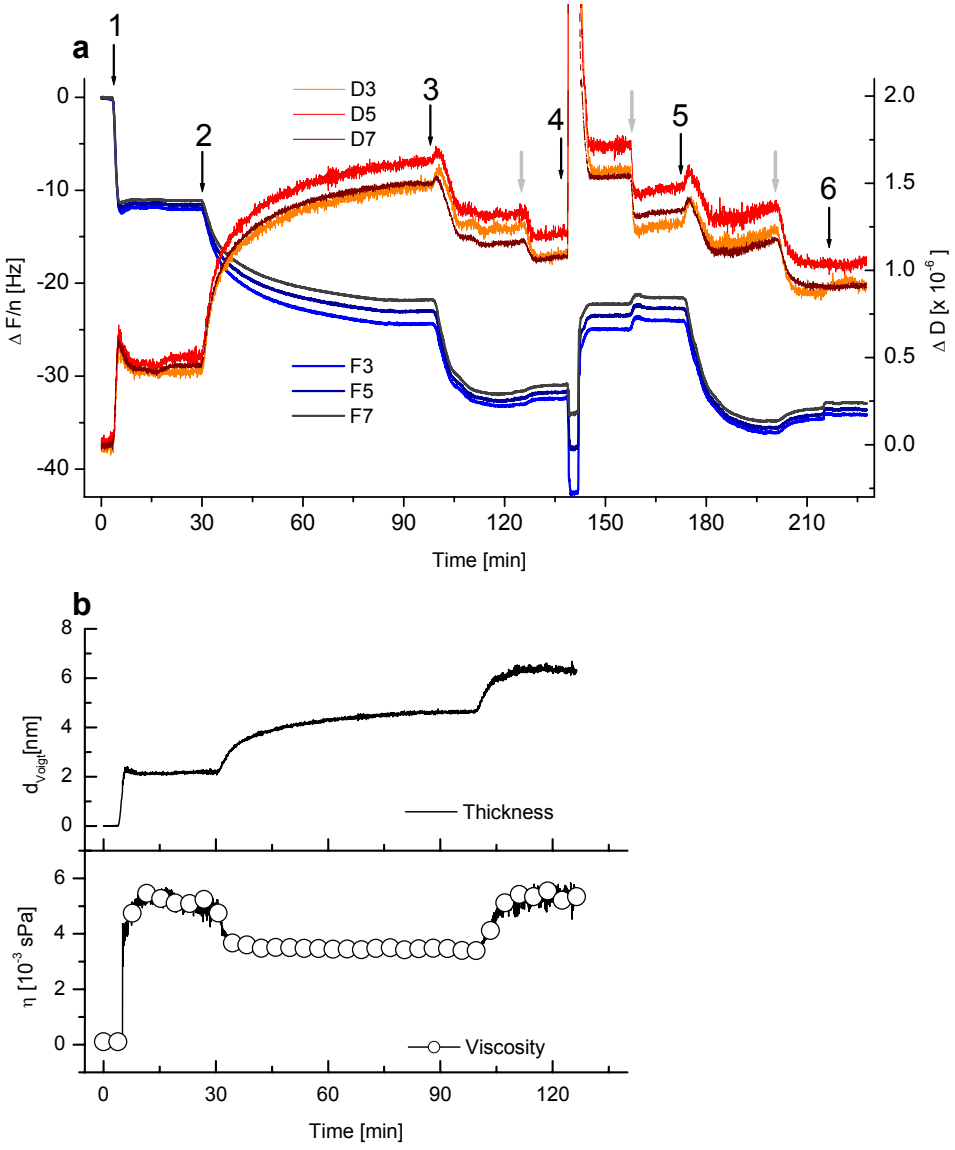

Figure 5.6: KF binding to P15/T50. a: The reaction sequence starts with immobilization of P15 (1) followed by hybridization with T50 (2). Than, 30 nM KF were added (3) in the absence of dNTPs causing a decrease in ΔD and ΔF. After removal of the enzyme by rinsing with 1 M NaCl (4), KF binding (30 nM) was repeated (5) in a buffer containing $CaCl_2$ instead of $MgSO_4$. dNTPs were added to prove that KF is not active in the absence of Mg^{2+}. Gray arrows indicate rinsing with buffer. b: Time course for shear viscosity (bottom) and thickness (top) obtained from analyzing the raw data (n=5, 7) with the Voigt model.

Titration

In order to determine affinity constants from a single binding experiment, one has to measure the desorption rate, k_{off}, of a molecule upon rinsing with buffer in order to be able to interpret the adsorption process correctly. Since enzymes are known to alter their structural properties with time, at least in an artificial environment, it is difficult or impossible to observe a monophasic desorption behavior if the desorption process is slow. Alternatively, aiming at the affinity constant for KF and DNA, a titration experiment was performed. Fig. 5.7 depicts the binding of KF to P15/T50 while the enzyme concentration was gradually increased from 2.5 nM to a final value of 45 nM (injected twice). Strikingly, for concentrations larger than 12.5 nM, Δf droped down instantaneously after injection and started increasing again after a minimum frequency was reached. As it seems, the rate of this increase rises with enzyme concentration; at 45 nM a single exponential increase of 0.03 s^{-1} was found. Surprisingly, this was a factor of ten higher than the rate with which Δf increased upon rinsing with pure buffer. The question whether the increase in Δf was attributed to an actual mass change or structural changes within the film, was answered by monitoring the same reaction sequence by SPR (chapter 4.3). Although a small accumulation of mass during the initial binding phase was detected at high KF concentrations using SPR, the signal quickly leveled off to reach a stable equilibrium. Therefore, one is tempted to interpret the increase in frequency as indication for a structural change. However, the Voigt model did not confirm a structural change, since it attributed the changes in ΔD and Δf

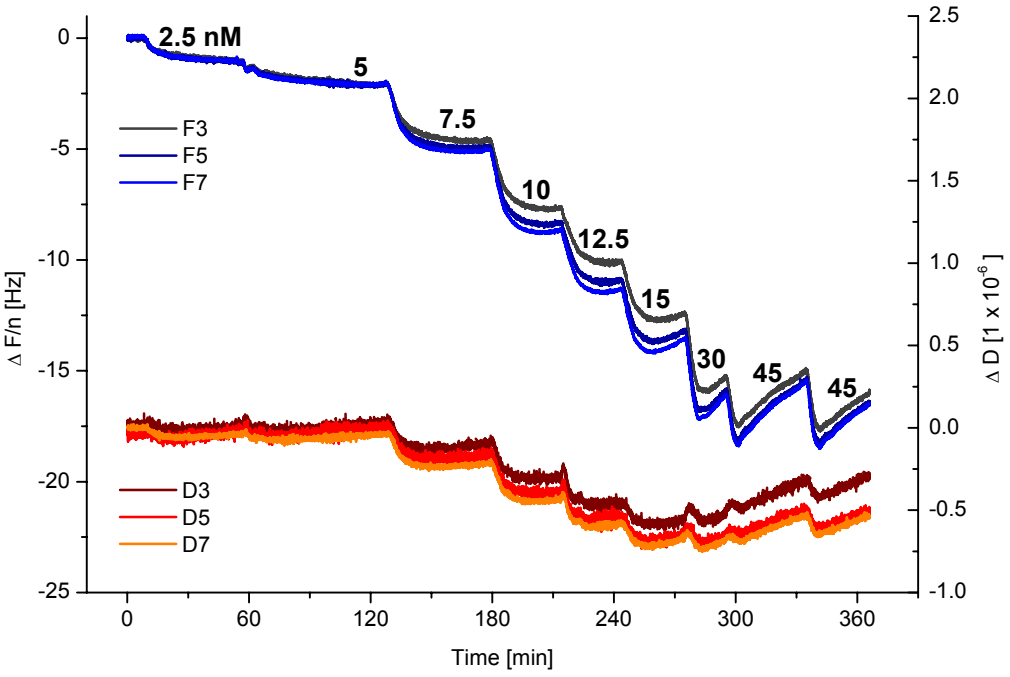

Figure 5.7: Titration experiment. Gradually increasing amounts of KF were bound to surface-attached P15/T50.

to changes of the effective film thickness which had time evolutions identical to ΔD and Δf. Fig. 5.8 compares the amount of bound KF as obtained from SPR with the mass-uptake measured by QCM-D.

The QCM experiment was analyzed using the classical Sauerbrey theory as well as the Voigt viscoelastic model; for high enzyme concentrations the analysis referred to the maximal frequency shift that was reached directly after injection of the enzyme before Δf started increasing again. The predictions for the final enzyme mass obtained from the Voigt model exceed the Sauerbrey based calculation by 25 %. The SPR curve has a hyperbolic shape, very well obeying the Langmuir model. Using this model, the affinity constant was calculated to be $1.3\times10^{8}\,M^{-1}$, which is in good agreement with the literature [Matsuno, 2001, Kuchta, 1987]. In contrast, the curves obtained from the QCM experiment are slightly sigmoid in shape. Since it does not make sense to assume a cooperative binding mechanisms in the particular case of DNA polymerases, the difference must be attributed to the way the methods create a signal. At low concentrations, SPR exhibits higher sensitivity than QCM. Surface roughness could be responsible for the lower sensitivity of QCM-D at low KF concentrations. The QCM is supposed to be sensitive to the geometric thickness of a film. If this is true, adsorption of molecules in troughs or crevices at the surface would not substantially increase Δf because it would not affect the geometric thickness of the film (provided the density of the substituted solvent is similar to the density of the adsorbed molecule) [Laschitsch, 2000].

The amount of enzyme bound to DNA at full coverage was 106 ng/cm^2 (1.7 pmol/cm2) in the SPR case and ~ 410 ng/cm^2 (4.4 pmol/cm^2) according to the Voigt analysis of the QCM data. In order to calculate the molar concentration of KF bound per area one can make use of the SPR data. Assuming a surface coverage with streptavidin of 3.8 pmol/cm^2, we can conclude that 54 % of the streptavidin molecules are occupied by a DNA polymerase. This result is in good agreement with values previously published for KF binding to biotin-coupled DNA of similar length [Matsuno, 2001]. The excess mass measured by QCM must be attributed to coupled water, yielding an effective film density of ρ_{eff}=1.1 g/cm^3 using eq. 2.26:

$$\rho_{eff} = \frac{\rho_{Protein} \cdot \Delta m_{SPR}}{\Delta m_{QCM}} + \rho_{Water}\left(1 - \frac{\Delta m_{SPR}}{\Delta m_{QCM}}\right)$$

taking ρ_{Water} and $\rho_{Protein}$ to be 1 and ~1.4 g/cm^3 [Höök, 2001]. This density deviates only slightly from that assumed for the DNA films (=1.06 g/cm^3). Thus, the error introduced by treating subsequently occurring DNA hybridization and replication reactions with a one layer model is small. Note that the product of the effective density and the thickness

is always constant in the Voigt model, which makes the mass determined using this model independent from the density that was employed during the fitting procedure.

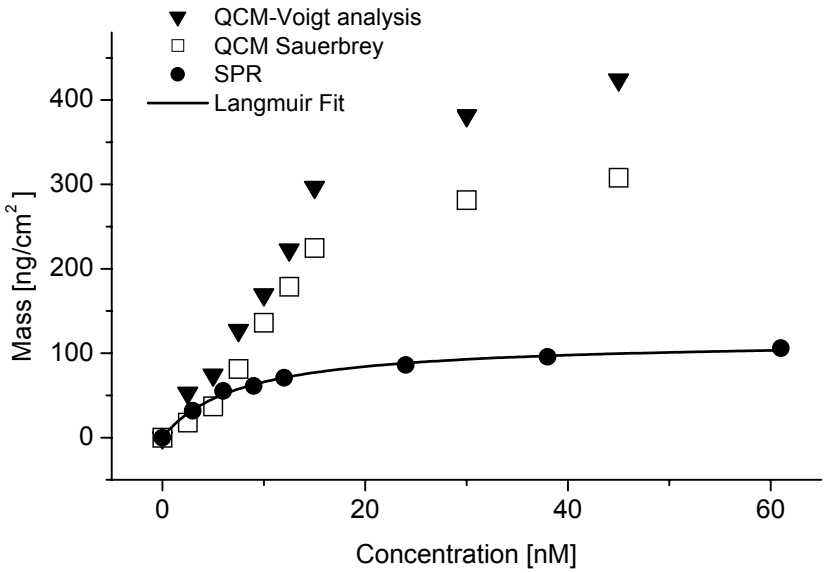

Figure 5.8: Surface concentration of KF bound to P15/T50 obtained from SPR (black circles) and QCM-D titration experiments. Mass values obtained from the Voigt model are plotted as black triangles, the corresponding Sauerbrey mass is given in open squares (see raw data in fig. 5.7). The QCM-D data refer to the mass corresponding to the maximum frequency shift.

However, the significance of the titration experiment monitored by QCM-D is a little doubtful due to the missing explanation for the unexpected changes in ΔD and Δf observed at high KF concentrations. The results obtained from SPR in the equivalent experiment clearly excluded the possibility that these changes originate from the desorption of the enzyme. Therefore, the mass changes predicted by the Voigt model must be attributed to changes in the amount of coupled water; variations in the amount of coupled water could originate from structural changes in the DNA film. Repeating the titration experiment on a surface that is only poorly covered with DNA strands should elucidate whether the contact of enzyme molecules bound to neighbored DNA strands caused these structural changes.

5.4.2 DNA elongation

In the previous paragraph, we reported successful binding of KF to surface attached DNA in the absence of dNTPs. The logical continuation of the work is to trigger enzymatic DNA extension by addition of a nucleotide mixture. Here, special emphasis will be put on the identification of distinct steps of the kinetic pathway. Such a

separation is not self-evident, considering the complexity of a reaction, in which DNA polymerization causes a mass increase, while the enzyme is simultaneously released from the complete DNA strands. Using a QCM with a fundamental frequency of 27 MHz, Okahata and coworkers studied the enzymatic DNA extension catalyzed by the KF [Matsuno, 2001, Niikura, 1998]. In this study, enzyme binding, DNA extension and enzyme release were reported to occur as well-separated, subsequent steps. The absolute amount of synthesized DNA was quantified by calibration of the system with known known mass loads, still assuming a linear relationship between Δf and Δm. This appraoch ignores the viscoelastic nature of the DNA films and withholds information obtainable from an exhaustive analysis using a viscoelastic model. Another critical point in this study was that the extension step happened on a time scale smaller than 20 s. This was only possible if all DNA strands on the surface would be extended in a highly synchronized process. But this could not be possible if only every third DNA strand was bound to KF at full coverage (as reported there) and transport of enzyme to other binding sites has to take place.

In contrast, here, the relevant reactions steps were found to be superimposed, thereby producing a quite complex response pattern. It was found that interpreting the QCM-D response on the basis of the changes in shear viscosity is more reliable than trusting Δf. Using viscoelastic parameters, structural changes of the DNA film were detected during the interaction with a DNA polymerase and during the transition from a single to a double strand.

5.4.2.1 Estimation of the mass added during DNA synthesis

For a start, the QCM-D response caused by the final product of DNA synthesis, a complete DNA duplex, was investigated. In order to create this duplex stepwise, a commercial oligonucleotide (T35) having a base sequence complementary to the template strand, was hybridized with P15/T50 (fig. 5.9a). Thereby, a DNA duplex was formed that exhibited a nick in the sugar-phosphate backbone between the 3'-terminus of the primer sequence and the 5'-terminus of T35. Analogously, the hybridization of T35 with P45/T50 was monitored (fig. 5.9c) in order to compare the signal caused by addition of identical masses. Since it was known from the SPR experiments that both DNA constructs were elongated with similar rates, this comparison should elucidate whether one of the constructs was more advantageous for elongation studies due to more pronounced changes in the viscoelastic properties.

Since the KF is a typical repair enzyme whose function it is to replace damaged DNA patches, it owns the ability to displace nicked DNA. Strand displacement activity was tested by exposure of the nicked DNA construct to 30 nM solution of KF yielding similar changes in ΔD and Δf as observed for KF binding to DNA substrates with

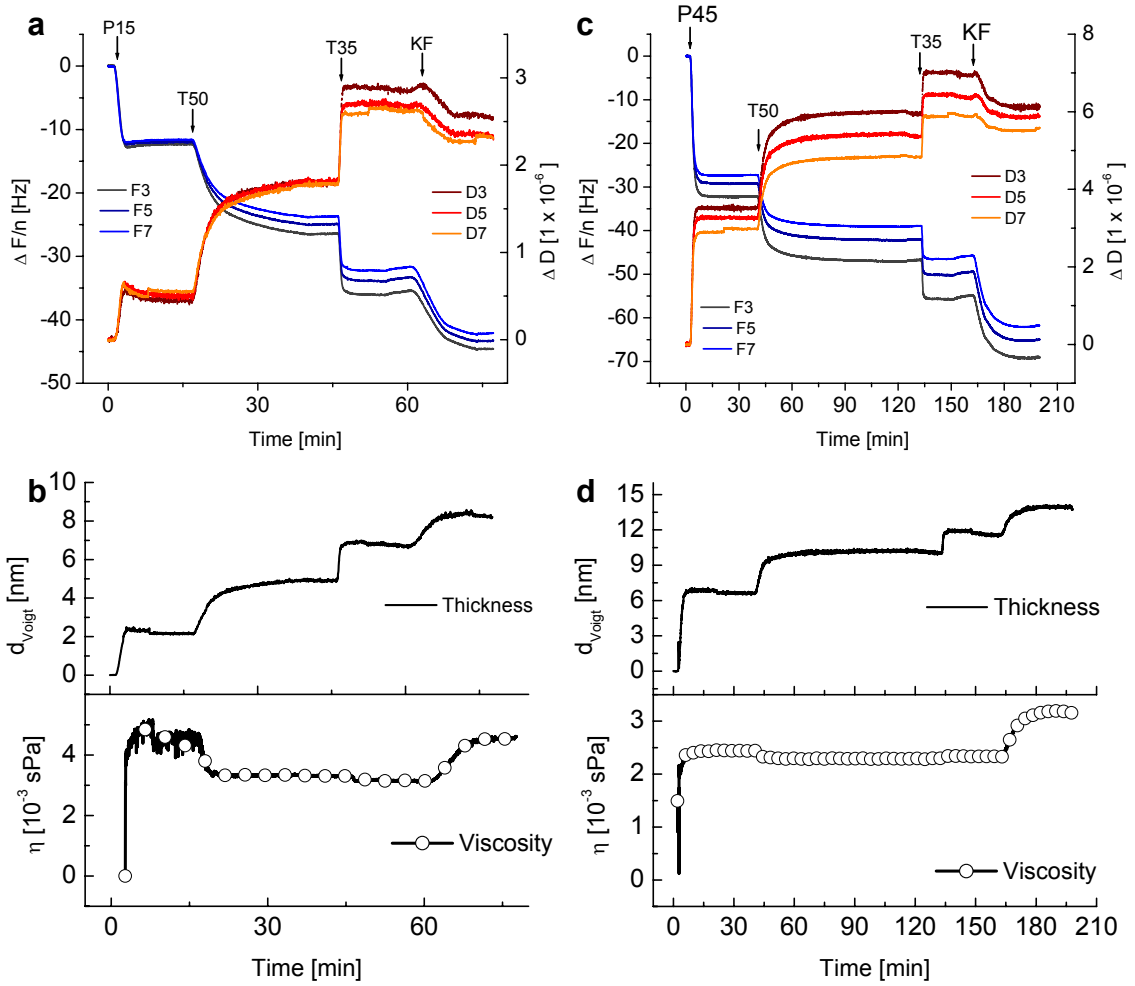

Figure 5.9: Mass response expected for complete replication of template T50. Data were recorded at n=3, 5 and 7. Hybridization of target T35 to P15/T35 (a) and P45/T50 (c), respectively, simulates the mass increase expected for complete replication of the template. The formed duplexes (P15/T50/T35 and P15/T50/T35, respectively) exhibited a nick between the 3'-terminus of P45 and the 5' end of T35. Due to the nick, they offered a potential binding site for DNA polymerases. KF was added (30 nM) in order to test for strand displacement activity.

recessed 3'-termini. The results of the Voigt analysis of the raw data in figures 5.9a and c are shown in figures 5.9b and d, respectively.

Hybridization of a 35-mer oligonucleotide was significantly faster than hybridization of a 15-mer complementary sequence due to the higher thermodynamic stability. Δf and ΔD were –9.1 Hz and 0.9×10^{-6} for both DNA constructs, yielding a thickness increase d_{Voigt} of 2 nm according to the modeling. For the spacer-free DNA construct the separation of the overtone responses became more pronounced, which was used as fingerprint for successful DNA extension in the following. Therefore, this DNA construct was chosen for further studies of the elongation process.

Displacement of T35 from P15/T50 caused shifts of Δf= -9.1 Hz and ΔD= -0.4, and Δf= -14.1 Hz and ΔD= -0.8 for P45/T50, respectively. In both cases, the QCM response was in agreement with the response observed for KF binding to P15/T50 and P45/T50

at identical concentrations. This indicates that binding to the nicked substrates occurred in the same fashion as binding to substrates with recessed 3'-termini, probably with the template bound as a single strand in the polymerization cleft. Since no mass release was detected, one has to assume that T35 was only partly displaced and remained partly hybridized to the template strand.

Taking into account the QCM-D results obtained for binding of KF to P15/T50 and for hybridization of T35 to the same duplex, enzymatic DNA extension should be attributed to: a) a final thickness increase of 2 nm b) a distinct separation of the overtones and c) a temporary stiffening of the DNA film due to interaction with the polymerase that shows up as an increase in shear viscosity and modulus.

5.4.2.2 Interpretation of the elongation process

In this section the enzymatic elongation of DNA will be discussed in the context of the results obtained for KF binding (chapter 5.4.1) and hybridization of target T35 (chapter 5.4.2.1).

Fig. 5.10 shows the QCM-D response for the elongation of duplex P15/T50 in the presence of 30 nM KF and 100 μM dNTPs (**1**). In order to facilitate the interpretation of the QCM-D response obtained for reaction (**1**), the response for following reactions are displayed in addition: binding of KF in the absence of dNTPs (**2**) and hybridization of T35 (**3**), where the latter simulates the response expected for complete primer extension (c.f. **1**). Clearly, curve **1** is a superposition of curves **2** and **3**: Bare KF binding (**2)** induces a monotonic decrease in both, D and f, while hybridization (**3**) induces an increase and decrease in D and f, respectively. Under conditions enabling DNA polymerization (**1**) there is an initial decrease in both f and D, after which both D and f start to increase. Note, however, that the final ΔD and Δf values after saturated reaction are in good agreement for the two cases were complete DNA duplex formation is expected (**1** and **3**).

The QCM-D response was further analyzed using the Voigt-based viscoelastic model. The best fits for n=5 and 7 are depicted in fig. 5.10, demonstrating a deviation less than 2 % for all harmonics. Fig. 5.11 compares the time evolution of d_{Voigt} and η_{Voigt} obtained for KF binding, DNA hybridization and DNA elongation as shown in fig. 5.10. Inspecting the changes in d_{Voigt} (fig. 5.11) firstly, it is clear that all three reactions induce a very similar Δd_{Voigt} of ~2nm, even though the kinetics of the elongation reaction (**1**) differs somewhat. The temporal variation is in this case attributed to an initial stretching of coiled DNA strands as KF binds (c.f. bare KF binding).

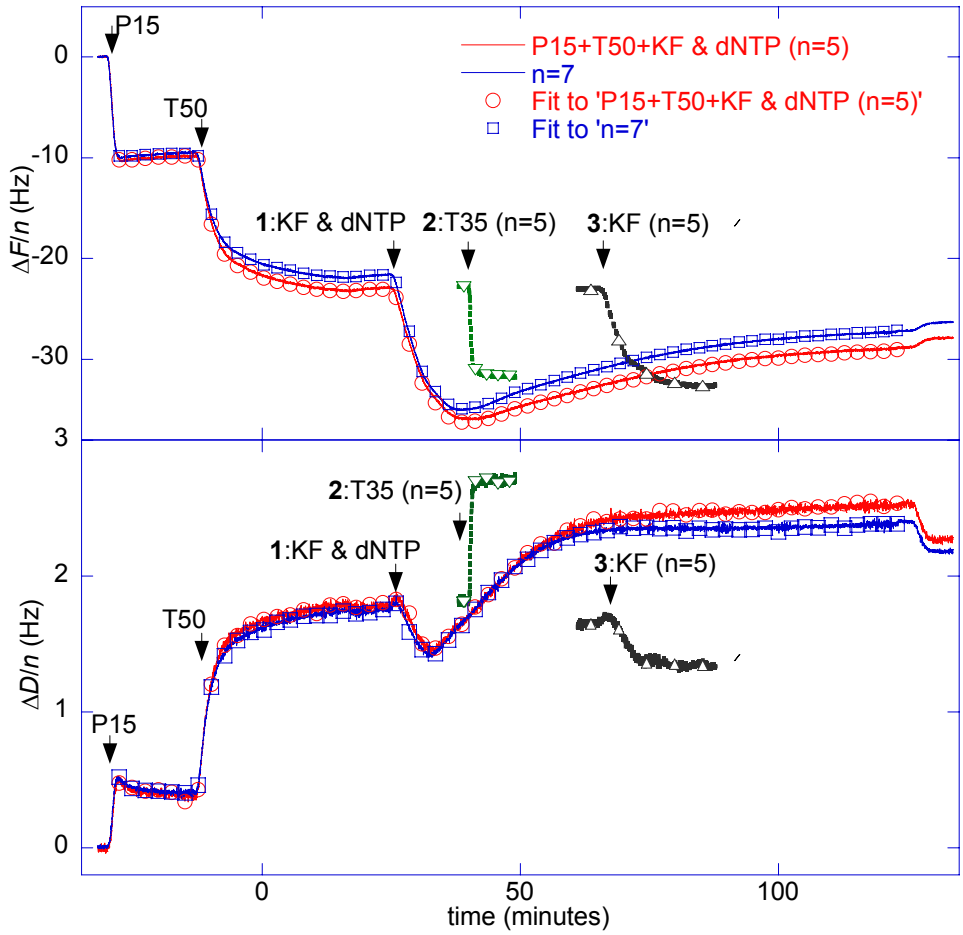

Figure 5.10: ΔF (top) and ΔD (bottom) versus time at n=5 (red) and 7 (blue) for the formation of duplex (P15 and T50) followed by its enzymatic extension (reaction 1). (Data were offset after immobilization of the streptavidin layer.) Also shown are superimposed data obtained upon T35 hybridization (reaction 2) at n=5 and KF binding in the absence of dNTPs (reaction 3) after formation of the P15/T50 template. The best fit between the data and the Voigt viscoelastic model is shown as open circles (n=5) and open squares (n=7) for (1).

As the elongation proceeds, the formed duplexes also contribute to an increase in d_{Voigt} (c.f. DNA hybridization), and as KF is eventually released, there is only a minor decrease in d_{Voigt}. However, since both KF binding and duplex formation contribute to an increase in d_{Voigt}, the efficiency of the elongation process cannot be judged from these data alone. Also note the qualitative difference between the time evolution of d_{Voigt} and Δf, where the former indicates a significantly higher mass uptake (thickness) at early stages in the process. One possible explanation for this difference might be the constant density used in order to estimate $d_{Voigt}(=\Delta m_{Voigt}/\rho_{effective})$. During KF binding, the density is expected to be slightly higher (by ~5%) than the one used. Nevertheless, correcting for this would decrease, rather than increase, the magnitude of the initial variation in thickness. A more likely explanation to this observation is therefore that the viscoelastic properties of the film are of such a kind that the observed changes in f and D are coupled, meaning that a change in f (or D) might equally well originate from a change in the viscoelastic properties as from a change in coupled mass – being of

uppermost importance when analyzing systems of this kind. However, while there are no dramatic differences in d_{Voigt} (or coupled mass) in the three cases, the obtained contrast is much higher in effective shear viscosity of the film (fig. 5.11b). Upon T35 hybridization, there is a rapid and very small decrease in η_{Voigt}, whereas there is a significant increase upon KF binding, signaling a substantial stiffening of the film in the latter case. This effect might originate from several factors: KF, having a hydrodynamic radius of ~3.4 nm [Joubert, 2003] encloses the DNA, thereby directly contacting 7-8 bp of the double-stranded primer/template region. Furthermore, the active sites responsible for double- and single strand binding are spatially separated. This, in turn, forces DNA to bend by 80° in order to enter the template binding cleft [Li, 1998]. It is still unknown how many bases are exactly buried in the template-binding cleft. However, its length of about 2.5 nm gives space for ~ 9 bases. The degree of flexible freedom for DNA should be significantly reduced considering these structural constraints. Furthermore, a release of 4-5 ions upon KF binding was reported [Datta, 2003], which causes changes in the electrostatic environment of DNA being likely to influences both its flexibility and hydration. This type of stiffening of the template upon KF binding is thus the likely origin also to the initial increase in viscosity observed upon elongation. However, in this case, three kinetic regimes are clearly visualized. The rates of the initial and the slowest phases are in good agreement with the time evolution of d_{Voigt}, where the initial phase is attributed to KF binding, whereas KF is released from completely double stranded DNA during the slowest phase (c.f. fig. 5.11a). During the intermediate phase, a process leading to a relatively rapid *decrease* in viscosity counteracts the initial increase in viscosity. Taking the speed of the polymerization process into account (k_{cat}= 5-10 bases/s), we are not expecting to see the enzyme moving on the nascent DNA strand. Furthermore, considering the reaction time required for complete polymerization, this process cannot occur processively, which means that the observed DNA synthesis is interrupted by frequent dissociation and rebinding events. Since KF binding to the primer/template *duplex* is solely determined by amino acid contacts to the phosphate backbone of DNA, it is sequence independent and is therefore expected to contribute equally to the viscosity during the elongation process. On the contrary, the affinity to the *single-stranded* template was reported to vary with sequence and length [Kuchta, 1987]. The obtained variation in viscosity, displaying an intermediate phase with a rate being different from both KF binding and release (c.f. fig. 5.11) is therefore tentatively attributed to structural differences of the KF/DNA complex depending on the length/sequence of the 5' nucleotide "overhang". Further experiments utilizing different template's lengths and sequences will be used to explore this observation in further detail.

The data presented here intriguingly demonstrate the potential of QCM-D in monitoring structural changes. At the same time, the study emphasizes that even though

a quite simplistic representation of the real system has been utilized, this is beneficial and important for the interpretation of the QCM-D response for dynamic protein-DNA interactions.

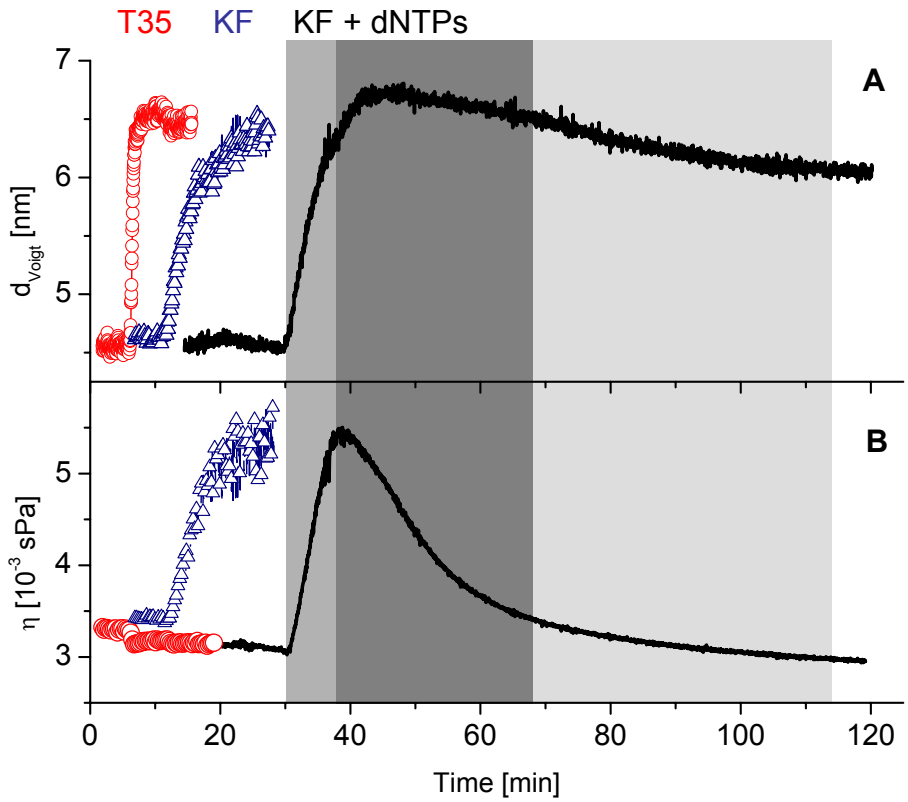

Figure 5.11: Time evolution of the effective thickness d_{Voigt} (A) and shear viscosity η_{Voigt} (B) for reaction 1 (open circles), 2 (open diamonds) and 3 (open squares) obtained by representing data in fig. 5.10 with a Voigt-based viscoelastic model. Three kinetic regimes in $\eta_{Voigt}(t)$ are indicated by shadow areas in gray, dark and light gray, respectively.

5.4.2.3 Verification of structural changes during duplex formation

As already mentioned, neither the thickness parameters determined by SPR nor those obtained from QCM measurements reflect the actual geometrical dimensions of a film. In order to examine the influence of KF binding and template-directed DNA synthesis on the conformation of the surface-attached DNA strands at least in a qualitative manner, SPFS experiments were carried out. In these experiments, the primer P15 was hybridized to 5'-Cy5-labeled template T50. The intensity of the fluorescence signal caused by the presence of this template, depends on the separation distance between the Cy5-labeled 5'-terminus and the metal surface. This originates from the fact that the radiation-less transfer of energy to the metal surface occurs in a distance-dependent

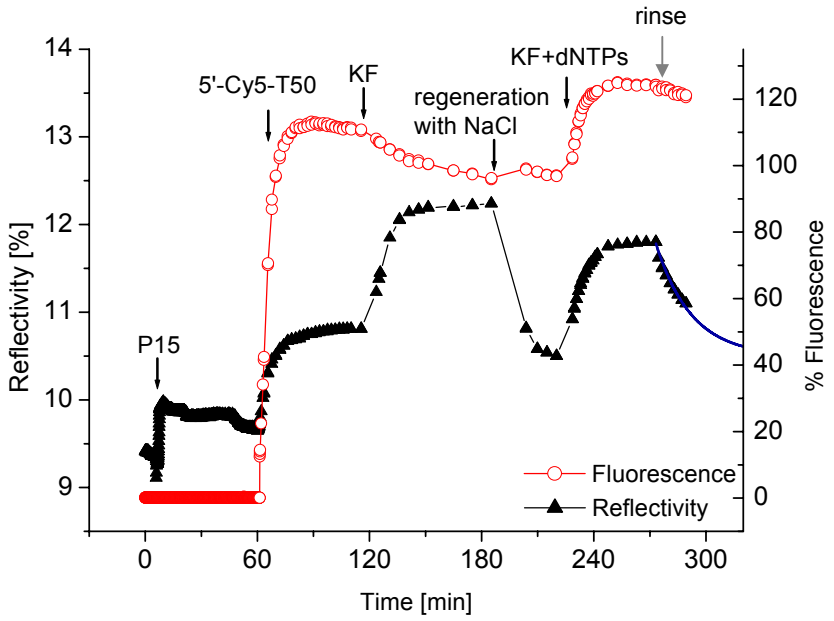

Figure 5.12: SPFS experiment aiming at conformational changes of DNA in complex with the KF and during primer extension. The experiment was performed using identical conditions like in fig. 5.10. P15 (1µM) was immobilized on a streptavidin layer and hybridized to a 5'-Cy5-labeled template, T50 (1µM). The observed fluorescence intensity depends on the position of the dye relative to the surface. The fluorescence decrease monitored upon KF binding (30 nM) must be attributed to photo-bleaching of the dye since removal of the enzyme did not recover the fluorescence light. The fluorescence increase due to synthesis of a DNA duplex (in the presence of 100 µM dNTPs) amounted to 20 %. Thus, the surface-attached DNA strand stretched out, thereby increasing the separation distance between dye and surface.

fashion according to eq. 2.21 (chapter 2.2.4). In order to calculate a theoretical quenching profile for the present system, one has to consider the probability for fluorescence emission in a) all directions b) towards the light detector on the backside of the prism and c) towards the gold surface, where coupling of the fluorescence light to surface plasmons is possible. Such a quenching profile is displayed in fig. 2.9 [Neumann, 2001]. Accordingly, a significant increase in fluorescence is predicted for distances ranging from 7 to 30 nm.

The maximal length of a 50-mer duplex that is oriented perfectly perpendicular to the surface should be 15 nm (50 × 0.3 nm), the binding matrix sets a minimal spacing distance of 5.5 nm. Since single strands are likely to adopt a less expanded coiled structure, one should be able to observe the transition of the partly single-stranded P15/T50 complex to a complete double strand. A further question was, if the KF will induce a measurable structural change upon binding. On the one hand, KF bends the template strand by 80° at the position where it enters, coming from the duplex binding domain, the polymerase domain. If the DNA substrates were fully stretched out prior to KF binding, one would expect a decrease of the overall film thickness at full coverage with enzyme. Assuming a coiled, entangled structure for the oligonucleotide would

imply that the thickness is even increased upon KF binding since the strands adopt a more ordered structure being bound in the responsible structural domains of the KF.

The experiment depicted in fig. 5.12 was carried out using identical conditions as described in chapter 5.4.2.2 including a reduction of the flow rate to 200 µl/min. The laser intensity was reduced since the system was found to be very sensitive to photo-bleaching. Firstly, the KF was exposed to the immobilized P15/5'-Cy5-T50 complex at 30 nM concentration. In order to test, if the initial decrease in fluorescence was a direct consequence of KF binding or caused by photo-bleaching of the dye, KF was quantitatively removed by treatment of the surface with 1 M NaCl. The fluorescence intensity was not affected by the regeneration step. Thus, one has to conclude that the binding process did not change the overall shape of the DNA strands significantly. In contrast, the fluorescence intensity increased by 20 % during formation of the duplex (in the presence of 30 nM KF and 100 µM unlabeled dNTPs). This is in agreement with previous results that exploited the hybridization reaction of unlabeled targets with labeled, anchored probes for the detection of DNA [Neumann, 2001]. There, a 30-mer single-stranded probe was found to stretch by ~3 nm upon hybridization to a 15-mer complementary target. Looking at the theoretical quenching profile (fig. 2.9), it is clear that there are arbitrary combinations of steps in fluorescence and thickness yielding 20 % intensity. According to the surface architecture, the change must occur somewhere in the range between 10 and 20 nm separation distance. Without a deeper analysis of the behavior of the labeled DNA strand under conditions that provoke conformational changes, for instance buffer solutions differing in ionic strength, one can only speculate about the exact distance change observed in experiment 5.12.

In contradiction to the experiment discussed in the previous chapter, the KF was not released from the DNA duplexes prior to rinsing. This does not necessarily disprove the interpretation of fig. 5.10, where the slow increase in frequency was attributed to release of the enzyme. Although equal flow rates were used, the transport conditions might vary if flow cells differing in size and geometry were used.

5.4.2.4 Catalytic activity of the Klenow fragment

In order to be able to judge the versatility of QCM-D in biochemical studies, it is necessary to determine the catalytic activity of the particular enzyme acting close to a surface. The simplest model that accounts for the enzymatic extension of DNA is a Michaelis-Menten reaction between a binary DNA/KF complex and the dNTP substrate. Here, the immobilized DNA/KF complex is assumed to be in equilibrium with a ternary DNA/KF/dNTP complex. The ternary complex has two options to decompose: either via the irreversible incorporation of a complementary nucleotide into the DNA strand

occurring with a rate k_{cat}, or via dissociation into the educts of the reaction (k_{-1}) (see chapter 4.6). According to eq. 4.1, plotting the initial velocity of primer extension versus the dNTP concentration yields a hyperbolic curve.

As described in chapter 5.4.2.2, the interpretation of the elongation reaction was complicated by the fact that we were not able to detect DNA extension and enzyme release as separated processes and changes in ΔD and Δf were coupled due to the viscoelastic behavior of the DNA films. In order to determine the catalytic constants, though, KF was bound to immobilized P15/T50 at a low fixed concentration of 2.5 nM prior to the addition of dNTP substrates. At this low concentration, the presence of enzyme was not expected to influence the QCM-D response very much. Six separate experiments were performed adding dNTP substrate at concentrations between 1 and 200µM, which caused a uniform increase in ΔD of $\sim 1 \cdot 10^{-6}$. The frequency change was –7 Hz for 1µM dNTP and about –10 Hz for other dNTP concentrations. By comparing these shifts in ΔD and Δf with that observed for T35 hybridization, one can conclude that the elongation process produced complete duplexes. The experimental procedure is exemplified in fig. 5.13.

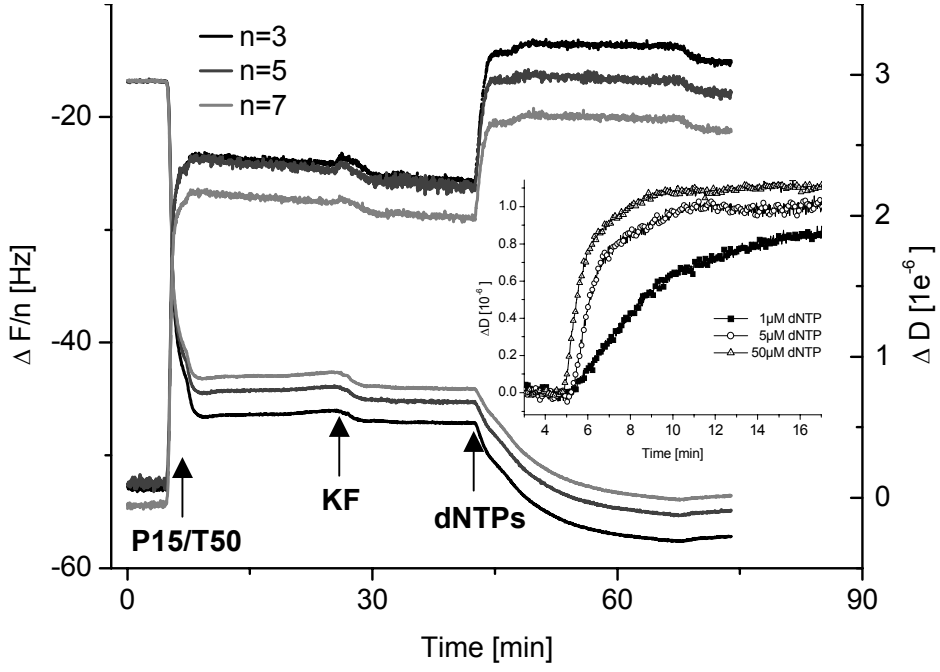

Figure 5.13: Enzymatic elongation of duplex P15/T50 using varying dNTP concentrations. Initial replication rates were obtained from the initial slopes of ΔD.

In order to evaluate the concentration-dependent experiments, the initial slopes of ΔD_3 were determined by linear regression, normalized to a uniform KF surface coverage and plotted versus the dNTP concentration. The resulting hyperbolic curve is depicted in fig. 5.14. Plotting the initial slopes of ΔF_3 instead, did not produce a similar trend.

From a linearized presentation of the Michaelis Menten equation, K_M was calculated to be ~3 µM. In order to calculate k_{cat}, giving the number of added bases per time unit, ΔD had to be translated into the molar concentration of incorporated nucleotides. This was done by considering the increase in Voigt mass as consequence of T35 hybridization. During this reaction 190 ng/cm^2 were immobilized, which was attributed to a change of the dissipation factor of $\Delta D \sim 1 \times 10^{-6}$. Applying $V_{max} = k_{cat} \cdot [KF]$, yielded k_{cat} =23 bases·s^{-1}. The catalytic constants are in good agreement with literature values, being K_M=5 µM and k_{cat}=10 s^{-1} [Kuchta, 1988].

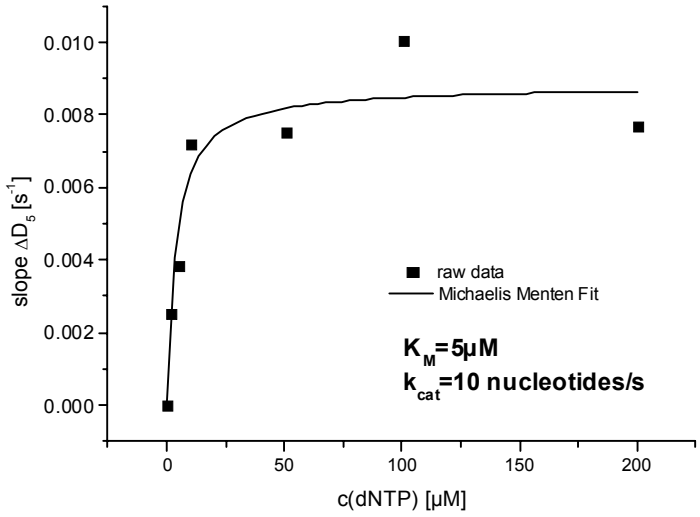

Figure 5.14: Slopes of ΔD_3 plotted versus dNTP concentration. The resulting hyperbolic curve is well described by the Michaelis Menten model.

5.5 Conclusions

Alternatively to SPFS, QCM-D was used as an independent mass-sensitive method for the characterization of the multi-layer sensor architecture. Being based on the reflection of an optical or acoustic wave at the substrate-film interface these two methods share some common principles. Although similar, it is possible to obtain complementary information from these techniques. Using them as means to measure film thickness, the results can differ tremendously. Whereas the optical thickness is proportional to the adsorbed mass (leading to an averaged thickness for dilute films), the acoustic thickness is governed by the mass moving on top of the quartz crystal. That means, solvent is sensed as additional mass if the adsorbate drags it along in its shear movement or if it is entrapped in cavities or troughs of the film. Consequently, comparing the film mass obtained from SPR and QCM permits to determine the film density, which gives access to the geometrical thickness of a film. Moreover, being capable of measuring viscoelastic film properties, the QCM-D technique has been shown to be useful in studying structural changes.

Referring to the biosensor surface invariably used in the scope of this work, QCM-D was used to verify the thickness of various DNA films and to investigate their viscoelastic properties. Special focus was also put on the structural dynamic of the polymerase-DNA interaction.

The QCM-D response observed upon probe immobilization and target hybridization clearly indicated viscoelastic film properties. Indeed, the data were well represented by a Voigt-based viscoelastic model and a comparative analysis using the classical Sauerbrey equation revealed that film mass was underestimated by 20-30 % using the latter one. However, the model gave a qualitatively correct interpretation of the binding kinetics. A systematic study of single-stranded DNA probes of different length resulted in a linear mass increase with length. At the same time the film viscosity decreased, which corresponds to decreased stiffness of the DNA films. Referring to SPR data for the same system, the DNA films were found to contain 90 % of water. The water content did not vary with DNA length, indicating that each nucleotide added coupled to the same amount of water. Therefore, the mass detected for binding of single-stranded DNA was a factor of 9 larger than expected, making QCM more sensitive than SPR in this respect. Yet, this did not hold for hybridization of the target. Here, binding is attributed to an exchange of coupled water with the complementary strand. Accordingly, the mass added due to hybridization corresponds to the density difference between bound DNA and replaced water only.

In summary, the large dissipative loss induced by DNA films combined with the high water content points towards elongated and flexible structures being primarily oriented outward from the surface.

QCM-D was also successful in monitoring binding of a DNA polymerase to immobilized DNA substrates. KF binding significantly stiffened the DNA film and caused a small thickness increase, which reflects the structural properties of the binary polymerase/DNA complex. Upon the initial binding phase, the slightly coiled DNA strands stretch out and become enclosed by the functional domains of KF. As consequence, the flexibility of the DNA chains is reduced. Water coupling during this step is less pronounced than in the DNA case, here the ratio between QCM : SPR signal amounted to 3 : 1.

DNA elongation was monitored with good resolution by following the increase in ΔD and Δf. However, at high enzyme concentrations the separation of the signals being attributed to the mass addition due to elongation of DNA and to the mass changes due to KF binding and release was not as clear as in the SPFS case. Since Voigt modeling revealed that changes in Δf and ΔD are coupled during DNA polymerization and rather originate from changes in viscoelastic properties than from changes in coupled mass, the viscosity was found to be more appropriate to extract kinetic information. Yet, it was more straightforward to perform the primer extension reactions at very low enzyme concentrations so that the experimental measures were solely attributed to DNA elongation. This way, the elongation velocity was found to be identical irrespective of the spacer length of the probe molecule. The influence of various dNTP concentrations up to 200 µM on the elongation rate was tested in order to investigate the concentration range that was not accessible by SPFS. Being in good agreement with solution experiments, the kinetics was confirmed to obey the Michaelis Menten model. Different from SPFS, the elongation process was found to be as efficient as hybridization. One might speculate that the use of labeled dNTPs promotes the premature termination of the replication process.

QCM-D was shown to be a valuable tool for studying structural changes and viscoelastic properties of a film, issues that cannot be addressed using SPR. However, without having the possibility to compare optical and acoustic data it would be difficult to extract quantitative information due to errors caused by water coupling. Regarding the sensitivity for the manipulation of single nucleotides, SPFS definitely beats QCM-D. In order to maximize the benefit it would be desirable to acquire QCM and SPR data simultaneously using the same gold surface.

6 Summary

Biosensors have been successfully applied to study DNA hybridization reactions for several years. However, this detection principle has only rarely been used to investigate DNA processing enzymes. In the present work, the versatility of surface analytical tools has been demonstrated not only for monitoring biomolecular recognition events but also for measuring the catalytic activity of an enzyme. The study was centered around the replication of surface-tethered oligonucleotides using a bacterial DNA polymerase, the Klenow fragment. The replication process could be successfully monitored in real-time utilizing Surface Plasmon enhanced Fluorescence Spectroscopy (SPFS) and the Quartz Crystal Microbalance with Dissipation monitoring (QCM-D).

Since both techniques require functionalization of a gold surface, identical surface architectures were used as matrix for DNA immobilization. Biotinylated primer oligonucleotides were bound to a streptavidin arrangement that was tethered to the gold surface by a self-assembled monolayer of biotinylated thiols. A DNA substrate with recessed 3'-terminus was formed by hybridization of the primer to an unmodified template oligonucleotide. The stepwise immobilization of the matrix components was followed using both, SPFS (label-free) and QCM-D, providing control over the multi-layer system. By comparison of the results obtained from both techniques, it was possible to determine the water content of each layer. In agreement with previous studies, streptavidin was found to form a monomolecular film exhibiting 50 % water as reported for 2-dimensional streptavidin crystals. A water content of 90 % was measured for the DNA films irrespective of the length of the primer oligonucleotides. Thus, identical amounts of water are coupled per nucleotide leading to a film with a high lateral dilution. As predicted for QCM measurements in liquids, the water coupled due to viscous drag was sensed as additional mass, which made the technique by a factor of ~10 more sensitive for the detection of DNA than SPR. Analysis of the QCM-D data using a viscoelastic model revealed that streptavidin forms a very rigid film, whereas the DNA films are relatively soft provoking large dissipative losses. Accordingly, one can assume elongated DNA chains, which are only moderately coiled. Only sequences being shorter than 15 nucleotides were significantly stiffer than longer oligonucleotides.

The sensor surface could be shown to be well-suited for DNA polymerase action. Binding and catalytic constants derived for enzymatic DNA synthesis were in good agreement with results obtained from solution. Thus, the catalytic activity of the Klenow fragment was not perturbed by the proximity to the surface. This was also proven by introducing a spacer region that increased the distance between enzyme and surface, which did not influence the experimental results. By introducing a poly-thymine tail as spacer, a second putative binding site for DNA polymerases was created. However, identical amounts of enzyme bound to the 15 nucleotide long primer/template

duplex of the different DNA substrates, demonstrating that exclusively 1:1 polymerase/DNA complexes were formed.

QCM-D and SPFS differed in their capability to resolve different steps involved in DNA replication. SPR was incapable of sensing the mass increase due to DNA synthesis. Therefore, DNA synthesis was visualized by incorporation of Cy5-labeled dCTP into the DNA strand. This way, enzyme binding and release (accounted for by reflectivity), and DNA polymerization (fluorescence intensity) were obtained as well separated signals which facilitated the interpretation of the experimental curves. Deviating from recent findings, the polymerase was clearly found to prefer the natural unlabeled dCTP substrate over the labeled one.

In contrast, the mass increase during DNA polymerization could be easily detected by QCM-D. Since the replication of immobilized DNA cannot occur synchronously at the surface, the signals being attributed to a mass loss due to enzyme release and an increase due to DNA synthesis were found to be superimposed. Despite of this complication, the process could be interpreted based on changes in shear viscosity. This became possible because formation of the double stranded replication product and the polymerase/DNA complex had opposite effects on the stiffness of the DNA films: while an identical viscosity was calculated before and after elongation, it was significantly increased as long as the polymerase directly interacted with the oligonucleotides. The latter finding is attributed to a loss of motional freedom and changes in the chemical environment of the oligonucleotides in complex with the DNA polymerase.

In conclusion, both techniques, QCM-D and SPFS, were successfully applied as biosensors for the real-time analysis of DNA replication. However, it makes sense to use them as complementary methods addressing different objectives. SPFS is unbeaten in sensitivity for the manipulation of single nucleotides; even dye concentrations of ~5 fmol/cm^2 could be easily detected. The strength of QCM-D lies clearly in its ability to give insights into the conformational dynamics of the DNA films.

7 Outlook

Major objective of this thesis was to demonstrate the versatility of biosensors in studies of the interaction between DNA polymerases and DNA. Towards this goal, an acoustic biosensor, the quartz crystal microbalance (QCM), and an optical biosensor, surface plasmon fluorescence spectroscopy (SPFS), were utilized. Both techniques were capable of measuring the catalytic constants for DNA polymerization performed by the *E. coli* Klenow fragment. Despite of the artificial environment of the sensor surface, neither the affinity of the polymerase to surface-attached DNA nor the catalytic activity were found to be impaired. Thus, biosensors being traditionally used for the determination of affinity constants also have potential in studies of enzyme kinetics on the molecular level.

However, the interpretation of the QCM response obtained for DNA elongation was rather complicated compared to the SPFS results. Using QCM, one encountered the problem that the mass change was the only experimental measure by which to sense a complex mechanism including enzyme binding and processing of the DNA. In disagreement to previous studies, the linear relationship between frequency and mass was found to be affected in the presence of large amounts of enzyme, making an analysis on the basis of a viscoelastic model beneficial. Since the polymerase binding induced a significant change in the shear viscosity of the DNA films, this parameter was found to be most helpful for the interpretation of the QCM signal. The strength of QCM lies clearly in the possibility to observe conformational changes by means of the viscoelastic properties of a material and variations in the amount of coupled water. Yet, the determination of the water content of a film requires the use of reference methods, which are sensitive to the mass of the "dry" film like SPR, ellipsometry or waveguide spectroscopy. Since the transport of mass is crucial to all biosensor reactions, one would profit significantly from combined QCM and SPR measurements utilizing the same gold surface. In such a combined set-up, a direct comparison of the reaction kinetics became possible, yielding the water content of a film as a function of time. Those measurements are necessary to elucidate the origins of shear viscosity; it has been anticipated recently that viscosity was a result of viscous friction between hydrodynamically entrapped water and immobilized molecules. Towards this goal, the combination of electrochemical methods with QCM is also promising, giving insights into the ion/solvent transport between film and bulk liquid, electron density and redox potential. By controlling the potential of a surface it is possible to examine the importance of electrostatic interactions for a certain biological system. From the thermodynamic point of view, the binding of proteins to DNA is driven by numerous effects like ion release, hydrophobic and electrostatic interactions, at the same time proteins may enclose or bend the DNA strands in the binary protein/DNA complex. If

the origins of shear viscosity were clearer, one would be able to attribute changes in viscosity to particular processes of the binding mechanism, which would in turn improve the interpretation of QCM data. For instance, one could compare the QCM response obtained from DNA polymerases that bend DNA and from those which do not. Similarly, the impact of electrostatic interactions could be estimated by using DNA binding proteins, which mediate binding primarily via hydrophobic contacts to the DNA bases and those that contact exclusively the phosphate sugar backbone. Furthermore, it would be interesting to learn more about the actual dimensions of a film by using methods like atomic force microscopy; thinking of proteins sitting like a point mass on a string of DNA it certainly makes a difference at which distance from the surface one places the mass. This question could be addressed by placing the recognition sequence for a restriction enzyme at different positions of an oligonucleotide strand. In this context, SPFS experiments that exploit the distance-dependence of the fluorescence emission near a metal surface, allow at least for the qualitative analysis of the film dimensions.
Although, biology provides a wealth of enzymes which are superior to manmade molecules regarding a specific function, it is questionable if one ever gains adequate control of those systems to decipher structure-function relationships in ensemble experiments. However, regarding the type of information obtainable from biosensor, they are at a intermediate stage between solution and single-molecule methods. Considering their ease of application they are definitely a good compromise to the experimentally challenging single molecule methods.

Whereas QCM was used to address fundamental objectives like the conformational changes of DNA in the present work, SPFS is a more application-oriented technique. Although the orientation of this thesis was rather methodological, the obtained SPFS results can be considered as a vantage point for the further development of methods for DNA detection. Using SPFS, a two step procedure was established including targeting of a certain DNA sequence from solution and the subsequent use of the overhanging single-strands as templates for nucleotide incorporation. The presence of fluorescently-labeled nucleotides incorporated into DNA at femto-molar surface concentration could be easily detected. The inhibition of the primer extension reaction in the presence of a terminal base mismatch was demonstrated and the specificity of the replication reaction further addressed by examining the effect of internal base mismatches. A base mismatch 3 bases upstream of the 3'-terminus of the primer slowed the elongation process substantially, allowing for distinguishing a perfectly matched from a mismatched DNA substrate. In order to test the applicability of this method, future experiments should address: the efficiency of the method in the presence of unspecific background DNA, influence of base mismatches besides G-G at various positions of the primer, adjustment

of the optimal label concentration that ensures minimal intramolecular quenching effects and the role of the length of the 5' base overhang.

The presented DNA sensor could further be used for the fast screening of the activity of protein mutants. Doing so, a variety of DNA processing enzymes could be investigated: those that incorporate labeled nucleotides like DNA and RNA polymerases, or those which remove nucleotides like restriction enzymes by DNA cleavage and exonucleases by hydrolysis. Using such an biosensor, only one assay is necessary in order to decide if a low yield of reaction product is caused by changes in the binding affinity or the catalytic activity, a question that is crucial for biochemical studies aiming at the elucidation of the catalytic center of enzymes.

Biosensor are useful for the investigations of biomolecules in a controllable environment of reduced complexity. Furthermore, studying the compatibility of enzyme reactions with various surface materials provides the basis for the use of enzymes as tools for the fabrication of nano-architectures. In a sense, DNA-synthesizing, -cleaving and –linking enzymes meet perfectly the requirements of the current trend for miniaturization and they are unbeaten regarding their specificity and efficiency. It is anticipated that future research will further focus on methods to exploit available biological functions for human needs as it has been done already in recombinant DNA technology.

Bibliography

V.M. Agranovich, *Surface Polaritrons*, North Holland, Amsterdam, 1982.

J.J. Aklonis and W.J. MacKnight, *Introduction to Polymer Viscoelasticity*, Wiley, New York, 1983.

W. L. Barnes and R. Amos, Phys. Rev. B, 55 (1997), pp. 7249.

A.S. Andersson, K. Glasmastar, D. Sutherland, U. Lidberg and B. Kasemo, *Cell adhesion on supported lipid bilayers*, J Biomed Mater Res., 64A (2003), pp. 622-629.

M.F. Bailey, E.H.Z. Thompson and D.P. Millar, *Probing DNA polymerase fidelity mechanisms using time-resolved fluorescence anisotropy*, Methods, 25 (2001), pp. 62-77.

E. Bakker and M. Telting-Diaz, *Electrochemical sensors*, Anal Chem., 74 (2002), pp. 2781-800.

F. Barany, *Genetic disease detection and DNA amplification using cloned thermostable ligase*, Proc Natl Acad Sci USA, 88 (1991), pp. 189-193.

W.L. Barnes, *Fluorescence near interfaces: the role of photonic mode density*, Journal of modern optics, 45 (1998), pp. 661-699.

K. Bebenek, C.M. Joyce, M.P. Fitzgerald and T.A. Kunkel, *The fidelity of DNA synthesis catalyzed by derivatives of Escherichia coli DNA polymerase I*, J Biol Chem., 265 (1990), pp. 13878-87.

L.S. Beese, D. V. and T.A. Steitz, *Structure of DNA Polymerase I Klenow Fragment Bound to Duplex DNA*, Science, 260 (1993), pp. 352-355.

I. Braslavsky, B. Hebert, E. Kartalov and S.R. Quake, *Sequence information can be obtained from single DNA molecules*, Proc Natl Acad Sci U S A, 100 (2003), pp. 3960-4.

M. Brown and C. Royer, *Fluorescence spectroscopy as a tool to investigate protein interactions*, Curr Opin Biotech, 8 (1997), pp. 45-49.

A. Brecht and G. Gauglitz, *Recent developments in optical transducers for chemical or biochemical applications*, Sensors and Actuators B, 38-39 (1997), pp. 1-7.

W. Brise and B. Neubig, *Das große Quarzkochbuch*, Franzis Verlag, Feldkirchen, 1997.

M. Buckle, R.M. Williams, M. Negroni and H. Buc, *Real time measurements of elongation by a reverse transcriptase using surface plasmon resonance*, Proc. Natl. Acad. Sci. USA, 93 (1996), pp. 889-894.

E. Burstein, W.P. Chen, Y.J. Chen and A. Hartstein, *Surface polaritrons-propagating electromagnetic model at interfaces*, J. Vac. Sci. Technol., 2 (1974), pp. 1004-1009.

H.R. Carver TE Jr, Millar DP, *Proofreading DNA: recognition of aberrant DNA termini by the Klenow fragment of DNA polymerase I*, Proc Natl Acad Sci U S A, 91 (1994), pp. 10670-4.

A.S. Chilkoti, P. S., *Molecular origins of the slow streptavidin-biotin dissociation kinetics*, J. Am. Chem. Soc., 117 (1995), pp. 10622-10628.

M.A. Cooper, *Label-free screening of bio-molecular interactions*, Anal Bioanal Chem., 377 (2003), pp. 834-42.

M.E. Dahlberg and S.J. Benkovic, *Kinetic Mechanism of DNA Polymerase I (Klenow Fragment): Identification of a second conformational change and Evaluation of the Internal Equilibrium Constant*, Biochemistry, 30 (1991), pp. 4835-4843.

S.A. Darst, M. Ahlers, P.H. Meller, E.W. Kubalek, R. Blankenburg, H.O. Ribi, H. Ringsdorf and R.D. Kornberg, *2Dimensional Crystals of Streptavidin On Biotinylated Lipid Layers and Their Interactions With Biotinylated Macromolecules*, Biophysical Journal, 59 (1991), pp. 387-396.

K. Datta and V.J. LiCata, *Salt dependence of DNA binding by Thermus aquaticus and Escherichia coli DNA polymerases*, Journal of Biological Chemistry, 278 (2003), pp. 5694-5701.

M. Daune, *Molekulare Biophysik*, Viehweg Verlag, Braunschweig, 1997.

M. Delarue, O. Poch, N. Tordo, D. Moras and P. Argos, *An attempt to unify the structure of polymerases*, Protein Eng., 3 (1990), pp. 461-467.

K.H. Drexhage, Prog. Optics, 12 (1974), pp. 165.

B. Dubertret, M. Calame and A.J. Libchaber, *Singel-mismatch detection using gold-quenched fluorescent oligonucleotides*, Nature Biotechnology, 19 (2001), pp. 365-370.

H. Echols and M.F. Goodman, *Fidelity mechanisms in DNA replication*, Annu Rev Biochem., 60 (1991), pp. 477-511.

J.R. Epstein, I. Biran and D.R. Walt, *Fluorescence-based nucleic acid detection and microarrays*, Analytica Chimica Acta, 469 (2002), pp. 3-36.

R. Favis, J.P. Day, N.P. Gerry, C. Phelan, S. Narod and F. Barany, *Universal DNA array detection of small insertions and deletions in BRCA1 and BRCA2*, Nature Biotechnology, 18 (2000), pp. 561-564.

Z. Foldes-Papp, B. Angerer, P. Thyberg, M. Hinz, S. Wennmalm, W. Ankenbauer, H. Seliger, A. Holmgren and R. Rigler, *Fluorescently labeled model DNA sequences for exonucleolytic sequencing*, J Biotechnol., 86 (2001), pp. 203-24.

K. Faulds, W.E. Smith and D. Graham, *Evaluation of surface-enhanced resonance Raman scattering for quantitative DNA analysis*, Anal Chem., 76 (2004), pp. 412-7.

C.C. Fong, W.P. Lai, Y.C. Leung, S.C.L. Lo, M.S. Wong and M.S. Yang, *Study of substrate-enzyme interaction between immobilized pyridoxamine and recombinant porcine pyridoxal kinase using surface plasmon resonance biosensor*, Biochimica Et Biophysica Acta-Protein Structure and Molecular Enzymology, 1596 (2002), pp. 95-107.

P.S. Freemont, J.M. Friedman, L.S. Beese, M.R. Sanderson and T.A. Steitz, *Cocrystal structure of an editing complex of Klenow fragment with DNA*, Proc Natl Acad Sci U S A, 85 (1988), pp. 8924-8.

M. Goodman, *Hydrogen bonding revisited: geometric selection as a principal determinant of DNA replication fidelity*, Proc Natl Acad Sci U S A, 94 (1997), pp. 10493-5.

A.W. Peterson, L.K. Wolf and R.M. Georgiadis, *Hybridization of mismatched or partially matched DNA at surfaces*, J Am Chem Soc, 124 (2002), pp. 14601-7.

I. Gorshkova, J.W. Rausch, S.F. Le Grice and R.J. Crouch, *HIV-I reverse transcriptase interaction with model RNA-DNA duplexes*, Anal Biochem, 291 (2001), pp. 198-206.

L. Häussling, Ringsdorf, H., Schmitt, F.-J., Knoll, W., *Biotin-Functionalized Self-Assembled Monolayers on Gold: Surface Plasmon Optical Studies of Specific Recognition Reactions*, Langmuir, 7 (1991), pp. 1837-1840.

R.J. Heaton, A.W. Peterson and R.M. Georgiadis, *Electrostatic surface plasmon resonance: direct electric field-induced hybridization and denaturation in monolayer nucleic acid films and label-free discrimination of base mismatches*, Proc Natl Acad Sci U S A, 98 (2001), pp. 3701-4.

T. Heyduk, *Measuring protein conformational changes by FRET/LRET*, Current Opinion in Biotechnology, 13 (2002), pp. 292-6.

P. Holland, R. Abramson, R. Watson and D. Gelfand, *Detection of specific polymerase chain reaction product by utilizing the 5'-3' exonuclease activity of Thermus Aquaticus DNA polymerase*, Proc Natl Acad Sci USA (1991), pp. 7276-7280.

J. Homola, *Present and future of surface plasmon resonance biosensors*, Anal Bioanal Chem., 377 (2003), pp. 528-39.

F. Höök, B. Kasemo, T. Nylander, C. Fant, K. Sott and H. Elwing, *Variations in coupled water, viscoelastic properties, and film thickness of a Mefp-1 protein film during adsorption and cross-linking: A quartz crystal microbalance with dissipation monitoring, ellipsometry, and surface plasmon resonance study*, Analytical Chemistry, 73 (2001), pp. 5796-5804.

F. Höök, A. Ray, B. Norden and B. Kasemo, *Characterization of PNA and DNA immobilization and subsequent hybridization with DNA using acoustic-shear-wave attenuation measurements*, Langmuir, 17 (2001), pp. 8305-8312.

F. Höök, M. Rodahl, P. Brzezinski and B. Kasemo, *Energy dissipation kinetics for protein and antibody-antigen adsorption under shear oscillation on a quartz crystal microbalance*, Langmuir, 14 (1998), pp. 729-734.

J.D. Jackson, *Klassische Elektrodynamik*, de Gruyter, Berlin, 1988.

J. Jager and J. Pata, *Getting a grip: Polymerases and their substrate complexes*, Curr. Opin. Struc. Biol., 9 (1999), pp. 21-28.

D. Johannsmann, *Viscoelastic analysis of organic thin films on quartz resonators*, Macromolecular Chemistry and Physics, 200 (1999), pp. 501-516.

T. Johnson, J. Zhu, R. M. Wartell, *Differences between DNA base stacking energies are conserved over a wide range of ionic strength*, Biochemistry, 37 (1998), pp. 12343-12350.

A. Janshoff, H.J. Galla and C. Steinem, *Piezoelectric mass-sensing devices as biosensors-An alternative to optical biosensors?*, Angew Chem Int Ed Engl., 39 (2000), pp. 4004-4032.

A.M. Joubert, A.S. Byrd and V.J. LiCata, *Global conformations, hydrodynamics, and X-ray scattering properties of Taq and Escherichia coli DNA polymerases in solution*, Journal of Biological Chemistry, 278 (2003), pp. 25341-25347.

C.M. Joyce, *How DNA travels between the separate polymerase and 3'-5'-exonuclease sites of DNA polymerase I (Klenow fragment)*, Journal of Biological Chemistry, 264 (1989), pp. 10858-10866.

B.K. Kanazawa and J.G. Gordon, *The oscillation frequency of a quartz resonator in contact with liquid*, Analytica Chimica Acta, 175 (1985), pp. 99-105.

K. Kanazawa, Faraday Discussions, 107 (1997), pp. 77.

W. Karthe and R. Müller, *Integrierte Optik*, Akademische Verlagsgesellschaft Geest und Portig, Leipzig, 1991.

K.A. Marx, *Quartz crystal microbalance: a useful tool for studying thin polymer films and complex biomolecular systems at the solution-surface interface*, Biomacromolecules, 4 (2003), pp. 1099-120.

B. Kasemo, *Biological surface science*, Surface Science 500 (2002), pp. 656-677.

M. Kinjo, *Quantitative analysis by the polymerase chain reaction using fluorescence correlation spectroscopy*, Analytica Chimica Acta, 365 (1997), pp. 43-48.

W. Knoll, *Guided Wave Optics for the Characterization of Polymeric Thin Films and Interfaces*, , *Handbook of Optical Properties*, CRC Press, 1997, pp. 373-399.

W. Knoll, *Interfaces and thin films as seen by bound electromagnetic waves*, Annual Review of Physical Chemistry, 49 (1998), pp. 569-638.

W. Knoll, M. Zizlsperger, T. Liebermann, S. Arnold, A. Badia, M. Liley, D. Piscevic, F.J. Schmitt and J. Spinke, *Streptavidin arrays as supramolecular architectures in surface- plasmon optical sensor formats*, Colloids and Surfaces a-Physicochemical and Engineering Aspects, 161 (2000), pp. 115-137.

A. Kornberg and T. Baker, *DNA Replication*, Freeman, New York, 1992.

A. Krieg, S. Laib, T. Ruckstuhl and S. Seeger, *Real-time detection of nucleotide incorporation during complementary DNA strand synthesis*, ChemBioChem, 4 (2003), pp. 589-592.

R.D. Kuchta, P. Benkovic and S.J. Benkovic, *Kinetic Mechanism Whereby Dna-Polymerase-I (Klenow) Replicates Dna With High Fidelity*, Biochemistry, 27 (1988), pp. 6716-6725.

R.D. Kuchta, V. Mizrahi, P.A. Benkovic, K.A. Johnson and S.J. Benkovic, *Kinetic Mechanism of Dna-Polymerase-I (Klenow)*, Biochemistry, 26 (1987), pp. 8410-8417.

T.A. Kunkel and K. Bebenek, *DNA Replication Fidelity*, Annu. Rev. Biochem., 69 (2000), pp. 497-529.

J.R. Lakowicz, *Principles of Fluorescence Spectroscopy*, Kluwer Academic Pub, 1999.

C. Larsson, M. Rodahl and F. Höök, *Characterization of DNA immobilization and subsequent hybridization on a 2D arrangement of streptavidin on a biotin-modified lipid bilayer supported on SiO2*, Analytical Chemistry, 75 (2003), pp. 5080-5087.

A. Laschitsch, B. Menges and D. Johannsmann, *Simultaneous determination of optical and acoustic thicknesses of protein layers using surface plasmon resonance spectroscopy and quartz crystal microweighing*, Applied Physics Letters, 77 (2000), pp. 2252-2254.

Y. Li, S. Korolev and G. Waksman, *Crystal structures of open and closed forms of binary and ternary complexes of the large fragment of Thermus Aquaticus DNA polymerase I: structural basis for nucleotide incorporation*, EMBO, 17 (1998), pp. 7514-7525.

T. Liebermann, *Oberflächenplasmonen-Fluoreszenzspektroskopie zur Detektion molekularer Erkennungsreaktionen*, Universität Mainz, 1999.

T. Liebermann, W. Knoll, P. Sluka and R. Herrmann, *Complement hybridization from solution to surface-attached probe-oligonucleotides observed by surface-plasmon-field- enhanced fluorescence spectroscopy*, Colloids and Surfaces a-Physicochemical and Engineering Aspects, 169 (2000), pp. 337-350.

T. Liebermann and W. Knoll, *Surface-plasmon field-enhanced fluorescence spectroscopy*, Colloids and Surfaces a-Physicochemical and Engineering Aspects, 171 (2000), pp. 115-130.

M. Little, J. Andrews, R. Moore, S. Bustos, L. Jones, C. Embres, G. Durmowicz, J. Harris, D. Berger and K. Yanson, *Strand displacement amplification and homogenous real-time detection incorporated in a second-generation DNA probe system*, Clin Chem, 45 (1999), pp. 777-784.

P.M. Lizardi, X. Huang, Z. Zhu, P. Bray-Ward, D.C. Thomas and D.C. Ward, *Mutation detection and single-molecule counting using isothermal rolling-circle amplification.*, Nat Genet, 19 (1998), pp. 225-232.

L.A. Loeb and T.A. Kunkel, *Fidelity of DNA synthesis*, Annu Rev Biochem., 51 (1982), pp. 429-457.

C.R. Lowe, *An introduction to the concept and technology of biosensors*, Biosensors, 1 (1985), pp. 3-16.

R. Lucklum, C. Behling and P. Hauptmann, *Role of mass accumulation and viscoelastic film properties for the response of acoustic-wave based chemical sensors*, Analytical Chemistry, 71 (1999), pp. 2488-2496.

H. Matsuno, K. Niikura and Y. Okahata, *Direct monitoring kinetic studies of DNA polymerase reactions on a DNA-immobilized quartz-crystal microbalance*, Chemistry-a European Journal, 7 (2001), pp. 3305-3312.

K. B, Mullis, *Target amplification for DNA analysis by the polymerase chain reaction*, Ann Biol Clin (Paris). 48(1990), pp. 579-82.

M. Myszka, *Kinetic analysis of macromolecular interactions using surface plasmon resonance biosensors*, Methods Enz., 295 (1998).

I. Nazerenko, S. Bhatnagar and R. Hohman, *A closed tube format for amplification and detection of DNA based on energy transfer*, Nucleic Acids Res, 25 (1997), pp. 2516-2521.

T. Neumann, *Strategies for detecting DNA hybridization using surface plasmon fluorescence spectroscopy*, Johannes-Gutenberg Universität, Mainz, 2001.

C.M. Niemeyer and D. Blohm, *DNA microarrays*, Angewandte Chemie-International edition, 38 (1999), pp. 2865-2869.

K. Niikura, H. Matsuno and Y. Okahata, *Direct monitoring of DNA polymerase reactions on a quartz- crystal microbalance*, Journal of the American Chemical Society, 120 (1998), pp. 8537-8538.

R.W.F. Noll, *Fluoreszenzspektroskopie*, *Methoden der biophysikalischen Chemie*, Teubner, Stuttgart, 1998.

Y. Okumoto, Y. Tanabe and N. Sugimoto, *Factors that contribute to efficient catalytic activity of a small Ca2+-dependent deoxyribozyme in relation to its RNA cleavage function*, Biochemistry, 42 (2003), pp. 2158-2165.

G.Y. Onoda and E.G. Liniger, *Experimental-Determination of the Random-Parking Limit in 2 Dimensions*, Physical Review a, 33 (1986), pp. 715-716.

P.H. Patel and L.A. Loeb, *Getting a grip on how DNA polymerases function*, nature structural biology, 8 (2001), pp. 656-659.

H.P. Patel, M. Suzuki, E. Adman, A. Shinkai and L.A. Loeb, *Prokaryotic DNA Polymerase I: Evolution, Structure, and "Base Flipping" Mechanism for Nucleotide Selection*, J. Mol. Biol., 308 (2001), pp. 823-837.

I.A. Pemberton and M. Buckle, *Real-time in vitro analysis of transcription by RNA polymerase on immobilized DNA fibers*, Journal of Molecular Recognition, 12 (1999), pp. 322-327.

J. Petruska, L.C. Sowers and M.F. Goodman, *Comparison of nucleotide interactions in water, proteins, and vacuum: model for DNA polymerase fidelity*, Proc Natl Acad Sci U S A, 83 (1986), pp. 1559-62.

H. Raether, *Surface Plasmons on Smooth and Rough Surfaces and on Gratings*, Springer, Berlin, 1988.

E. Reimhult, F. Höök and B. Kasemo, *Vesicle adsorption on SiO2 and TiO2: Dependence on vesicle size*, Journal of Chemical Physics, 117 (2002), pp. 7401-7404.

R. Reiter, H. Motschmann and W. Knoll, *Ellipsometric Characterization of Streptavidin Binding to Biotin-Functionalized Lipid Monolayers At the Water Air Interface*, Langmuir, 9 (1993), pp. 2430-2435.

M. Rodahl, F. Höök and B. Kasemo, *QCM operation in liquids: An explanation of measured variations in frequency and Q factor with liquid conductivity*, Analytical Chemistry, 68 (1996), pp. 2219-2227.

M. Rodahl, F. Höök, A. Krozer, P. Brzezinski and B. Kasemo, *Quartz-Crystal Microbalance Setup For Frequency and Q-Factor Measurements in Gaseous and Liquid Environments*, Review of Scientific Instruments, 66 (1995), pp. 3924-3930.

M. Rodahl and B. Kasemo, *A simple setup to simultaneously measure the resonant frequency and the absolute dissipation factor of a quartz crystal microbalance*, Review of Scientific Instruments, 67 (1996), pp. 3238-3241.

T. Ruckstuhl, M. Rankl and S. Seeger, *Highly sensitive biosensing using a supercritical angle fluorescence (SAF) instrument*, Biosens Bioelectron. 2003 Aug 15; 18(9): 1193-9., 18 (2003), pp. 1193.

W. Saenger, *Principles of nucleic acid structure*, Springer, New York, 1983.

S.K. Sahoo and V. Labhasetwar, *Nanotech appraoches to drug delivery and imaging*, Drug Discovery Today, 8 (2003), pp. 1112-20.

M.G. Samant, C.A. Brown and J.G. Gordon, *Structure of an Ordered Self-Assembled Monolayer of Docosyl Mercaptan On Gold(111) By Surface X-Ray-Diffraction*, Langmuir, 7 (1991), pp. 437-439.

T. Sano, C.L. Smith and C.R. Cantor, *Immuno-PCR: very sensitive antigen detection by means of specific antibody–DNA conjugates*, Science, 258 (1992), pp. 120-122.

G. Sauerbrey, *Verwendung von Schwingquarzen zur Wägung dünner Schichten und zur Mikrowägung*, Z. Phys., 155 (1959), pp. 206-222.

S. Scheuring, Müller D. J., Ringler, P., Heyman, J. B., Engel, A., *Imaging streptavidin 2D crystals on biotinylated lipid monolayers at high resolution with the atomic force mocroscope*, Journal of Microscopy, 193 (1999), pp. 28-35.

B. Schweitzer and S. Kingsmore, *Combining nucleic acid amplification and detection*, Current Opinion in Biotechnology, 12 (2001), pp. 21-27.

M. Senior, R. A. Jones, K. J. Breslauer, *Influence of loop residues on the relative stability of hairpin structures*, Proc. Natl. Acad. Sci. USA, 85 (1988), pp.6242-6246.

J.I. Siepmann and I.R. McDonald, *Monte-Carlo Study of the Properties of Self-Assembled Monolayers Formed By Adsorption of Ch(3)(Ch(2))(15)Sh On the (111) Surface of Gold*, Molecular Physics, 79 (1993), pp. 457-473.

K.L. Smith, Electronics & Wireless World, july (1986), pp. 51.

W.J. Spencer and K.L. Smith, J. Appl. Phys., 37 (1966), pp. 2557.

T.A. Steitz, *DNA Polymerases: Structural Diversity and Common Mechanisms*, The Journal of Biological Chemistry, 274 (1999), pp. 17395-17398.

J.D. Swalen, D.L. Allara, J.D. Andrade, E.A. Chandross, S. Garoff, J. Israelachvili, T.J. McCarthy, R. Murray, R.F. Pease, J.F. Rabolt, K.J. Wynne and H. Yu, *Molecular Monolayers and Films*, Langmuir, 3 (1987), pp. 932-950.

E.H. Thompson, M.F. Bailey, E.J. van der Schans, C.M. Joyce and D.P. Millar, *Determinants of DNA mismatch recognition within the polymerase domain of the Klenow fragment*, Biochemistry. 2002 Jan 22;41(3):713-22, 41 (2002), pp. 713-22.

B. Tinland, A. Pluen, J. Sturm and G. Weill, *Persistence length of single-stranded DNA*, Macromolecules, 30 (1997), pp. 5763-5765.

P.Y. Tsoi and M. Yang, *Kinetic study of various binding modes between human DNA polymerase beta and different DNA substrates by surface-plasmon-resonance biosensor*, Biochem J., 361 (2002), pp. 317-25.

S. Tyagi and F. Kramer, *Molecular beacons: probes that fluoresce upon hybridization*, Nat Biotech, 14 (1996), pp. 303-308.

A. Ulman, *An Introduction to Ultrathin Organic FIlms*, Academic press, London, 1991.

A. Vainrub, Montgomery Pettitt, B., *Thermodynamics of association to a molecule immobilzed in an electric double layer*, Chemical Physics Letters, 323 (2000), pp. 160-166.

M.V. Voinova, M. Rodahl, M. Jonson and B. Kasemo, *Viscoelastic acoustic response of layered polymer films at fluid-solid interfaces: Continuum mechanics approach*, Physica Scripta, 59 (1999), pp. 391-396.

J. Wang, T. Li, Y. Bai, Y. Zhu and Z. Lu, *Fabrication of unimolecular double-stranded DNA microarrays on solid surfaces for probing DNA-protein/drug interactions*, Molecules, 8 (2003), pp. 153-168.

W.W. Warner and C.D. Stockbridge, *Vacuum Microbalance Techniques*, Plenum Press, 3 (1963).

J.D. Watson and F.H.C. Crick, *A structure for deoxyribose nucleic acid*, Nature, 171 (1953), pp. 737-738.

P.C. Weber, D.H. Ohlendorf, J.J. Wendoloski and F.R. Salemme, *Structural Origins of High-Affinity Biotin Binding to Streptavidin*, Science, 243 (1989), pp. 85-88.

L. Westin, X. Xu, C. Miller, L. Wang, C. Edman and M. Nerenberg, *Anchored multiplex amplification on a microelectronic chip array*, Nat Biotech, 18 (2000), pp. 199-204.

D. Whitcombe, J. Theaker, S. Guy, T. Brown and S. Little, *Detection of PCR products using self-probing amplicons and fluorescence*, Nat Biotech, 65 (1999), pp. 804-807.

G.M. Whitesides, *The "right"size in nanobiotechnology*, Nat Biotech, 21 (2003), pp. 1161-1165

M.B. Wilchek, *The avidin-biotin complex in bioanalytical application*, Anal. Biochem., 184 (1988).

I. Willner, B. Willner and E. Katz, *Functional biosensor systems via surface-nanoengineering of electronic elements*, J Biotechnol., 82 (2002), pp. 325-55.

T. Wink, S.J. van Zuilen, A. Bult and W.P. van Bennekom, *Self-assembled monolayers for biosensors*, Analyst, 122 (1997), pp. R43-R50.

M.S. Yang, F.L. Chung and M. Thompson, *Acoustic Network Analysis As a Novel Technique For Studying Protein Adsorption and Denaturation At Surfaces*, Analytical Chemistry, 65 (1993), pp. 3713-3716.

P. Yeh, *Optical Waves in Layered Media*, John Wiley & Sons, New York, 1988.

F. Yu, D.F. Yao and W. Knoll, *Surface plasmon field-enhanced fluorescence spectroscopy studies of the interaction between an antibody and its surface- coupled antigen*, Analytical Chemistry, 75 (2003), pp. 2610-2617.

J. Zhai, H. Cui and R. Yang, *DNA based biosensors*, Biotechnol Adv., 15 (1997), pp. 43-58.

M. Zitzlsperger, *In situ Detektion von DNA Hybridisierungsreaktionen auf multifunktionalen Oligonukleotid-Chips auf der Basis der Oberflächenplasmonen-Mikroskopie*, Universität Mainz, 1998.

Appendix

a) Cleaning of the quartz crystals
Prior to surface modification, the gold electrodes were treated in a mixture of 100% NH3, 30% H2O2 and H20 (1:1:5) at 60 °C for 20 min. Alternatively the gold was cleaned in an UV/oxygen chamber for 15 min followed by treatment with Piranha solution for 1min. Cleaning was always finished by thoroughly rinsing the crystals with MilliQ water.

b) Cleaning of glass wafers before metal evaporation
For SPFS experiments, high refractive LaSFN9 glass wavers (20 × 20 × 2.5 mm, n= 1.8458, Helma, Germany) were used. Since the wavers have been reused several times, old metal films had to be removed. Wavers were usually evaporated with a very thin adhesion layer from Chromium underneath the gold film. Gold films were immersed in a mixture of KI (8 % w/v) and Iodine (2 % w/v) for 10 min. After brief rinsing with water, the chromium was removed by a 10 min treatment with an aqueous solution of ammonium cerium (IV) nitrate (Aldrich, 99 %). The samples were sequentially sonicated for 15 min each in a) 2 % alkaline detergent solution (Helmanex, Helma, Germany; sonification apparatus Super RK510, Sonorex, Germany), b) MilliQ water and c) 15 min sonification in ethanol (Chromasolv, Riedel-de Haen, Germany). In between the sonification steps the samples were rinsed with MilliQ water. Finally the samples were blown dry in a stream of nitrogen and placed directly into the evaporation apparatus for further processing.

c) Metal evaporation
For standard SPFS measurements, 47nm gold films (99.99%, Balzers) were deposited onto clean LaSFN9 wavers by thermal evaporation [Holland, 1966] at a deposition rate of 0.1 nm/s under UHV conditions (5·10-6 mbar) in an evaporation apparatus (Edwards, FL400 or Balzers, model BAE 250). To improve the adhesion of the gold film to the glass substrate a 2 nm thin chromium film was routinely evaporated first.

d) Streptavidin binding
Binding of streptavidin (Roche, Germany) to the biotinylated thiol SAM was carried out in physiological PBS buffer (10 mM phosphate buffer, 2.7 mM KCl, 150 mM NaCl, pH 7.4).

e) Conditions for DNA hybridization and elongation
Hybridization reactions were either performed in PBS buffer (10mM phosphate buffer, 2.7 mM KCl, 150 mM NaCl, pH 7.4) or in HSM buffer (10 mM HEPES, 150 mM NaCl and 10 mM MgSO4).

DNA extension assays were carried out using various concentrations of the exonuclease-free Klenow fragment of *E. coli* DNA polymerase I (Amersham Pharmacia) in HSM buffer. DNA extension was always initiated by a mixture of all four deoxynucleotidetriphosphates (dNTP, Amersham Pharmacia) and Cy5-labeled dCTP (Amersham Pharmacia) at various concentration.

f) Sequences of the oligonucleotides

All oligonucleotides used were purchased from MWG Biotech, Germany. The base sequences are given below; the experimental design making use of a particular oligonucleotide and its purpose are outlined in the respective result chapter.

Probes (primers)

5′-Biotin-ACG TCA GTC TCA CCC-3′	**P15**
5′-Biotin-$(TTT)_3$ACG TCA GTC TCA CCC-3′	**P30**
5′-Biotin-$(TTT)_5$ACG TCA GTC TCA CCC-3′	**P45**
5′-Biotin-$(TTT)_5$ACG TCA GTC TCA CCG-3′	**P45tG**
5′-Biotin-$(TTT)_5$ACG TCA GTC TCA GCC-3′	**P45iG**

Targets (templates)

T50
5′-AGT TAC AGA GGT AGT AGT GGC TGA GTG AAT ATT GT **G GGT GAG ACT GAC GT**-3′

T50G1close
5′-ACT TAC ACA CCT ACT ACT CCC TCA CTC AAT ATT GT **G GGT GAG ACT GAC GT**-3′

T50G1far
5′-AGT TAC ACA CCT ACT ACT CCC TCA CTC AAT ATT CT **G GGT GAG ACT GAC GT**-3′

T35
5′-ACA ATA TTC ACT CAG CCA CTA CTA CCT CTG TAA CT-3′

The parts of the template sequences, which are complementary to the primer strands, are shown in bold letters.

List of Figures